Dissertation

Tracking of Magnetite Labeled Nanoparticles in the Rat Brain using MRI

submitted by

Naira Pilar MARTÍNEZ VERA, MU

for the Academic Degree of

Doctor of Philosophy

(PhD)

at the

Medical University of Graz

Department of Neurology

under the Supervision of

Univ.-Prof. Dr.med.univ. Reinhold SCHMIDT
Assoz. Prof. Univ.-Doz. Dipl.-Ing. Dr. Stefan ROPELE

2017

A mi padre y a mi madre[*]

[*] To my father and mother

Declaration

I, Naira P. Martínez Vera, hereby declare that this dissertation is my own original work and that I have fully acknowledged by name all of those individuals and organizations that have contributed to the research for this dissertation. Due acknowledgement has been made in the text to all other material used. Throughout this dissertation and in all related publications I followed the guidelines of “Good Scientific Practice ".

Parts of this thesis have been published in: Martínez Vera N.P., Schmidt R., Langer K., Zlatev I., Wronski R., Auer E., Havas D., Windisch M., von Briesen H., Wagner S., Stab J., Deutsch M., Pietrzik C., Fazekas F., and Ropele R. 2014, "Tracking of magnetite labeled nanoparticles in the rat brain using MRI", PLOS ONE.

Prof. Dr. Claus Pietrzik (University Medical Center of the Johannes Gutenberg-University Mainz, Mainz), Prof. Klaus Langer (Institute of Pharmaceutical Technology and Biopharmaceutics, Münster), Ewald Auer, Balázs Dobrovich and also Daniel Havas from the JSW Life Sciences GmbH, Austria actively contributed to the results of the thesis.

Graz, 18.05.2017

...su inexorable evolución hacia una manifestación más crítica: el olvido. Quería decir que cuando el enfermo se acostumbraba a su estado de vigilia, empezaban a borrarse de su memoria los recuerdos de la infancia, luego el nombre y la noción de las cosas, y por último la identidad de las personas y aun la conciencia del propio ser, hasta hundirse en una especie de idiotez sin pasado.**

Cien años de soledad (1967) ***

Gabriel García Márquez (1927 - 2014)

** ... its inexorable evolution toward a more critical manifestation: a loss of memory. She meant that when the sick person became used to his state of vigil, the recollection of his childhood began to be erased from his memory, then the name and notion of things, and finally the identity of people and even the awareness of his/her own being, until he/she sank into a kind of idiocy that had no past.

*** One Hundred Years of Solitude (1967).

Acknowledgments

I would like first to express my gratitude to my supervisor Prof. Stefan Ropele (Department of Neurology, Medical University of Graz, MUG) for giving me the opportunity to join his MRI group in Graz and for his time spent supervising me during this thesis, his intense help in the MRI field and his patience and constant availability.

I would also like to express my gratitude to Prof. Dr. Reinhold Schmidt (Department of Neurology, MUG) and Prof. Rudolf Stollberger (Institute of Medical Imaging, Technical University), supervisor and member of my dissertation committee, for their support throughout this thesis. My sincere thanks also goes to Thomas Pekar and Michaela Haindl, in the laboratory at the Department of Neurology, MUG, who prepared the samples to analyze the different nanoparticle configurations using MRI. A very special thanks goes out to Ewald Auer und Balázs Dobrovich from the JSW Life Sciences GmbH who handled the rodents during the MRI experiments and also Daniel Havas (JSW Life Sciences GmbH) for conducting the fluorescence imaging work. Also I would like to thank Prof. Dr. Claus Pietrzik (University Medical Center of the Johannes Gutenberg-University Mainz, Mainz) and Prof. Klaus Langer (Institute of Pharmaceutical Technology and Biopharmaceutics, Münster) for the nanoparticle preparation and characterization, Prof. U. Karst, University of Muenster, for the TXRF experiments and Elektronen-Optik-Service GmbH for the preparation of the SEM images.

I would also like to thank the Medical University of Graz, the neurology department, and everyone who was involved in the "Brain Ageing" PhD program for giving me the opportunity to carry out my thesis, their advice and support. Thanks also the neuroimaging team, especially Michaela Söllinger for guiding me at the beginning of this work with the DESPOT1-sequence optimization, and Christian Langkammer for his advice and help in the susceptibility analysis and the correction of this dissertation. I would also like to acknowledge Patricia Linortner from the "Brain Ageing" PhD program, for all the time we spent together during the PhD courses and the exciting Journal Clubs. I gratefully acknowledge the Ludwig Boltzmann Institute for Clinical Forensic Imaging, in particular Martin Urschler, for giving me the opportunity to combine both a new research area and at the same

time allowing me to finalize analyses and write this thesis. Also from the same institute, I would like to thank Bridgette Webb for the dissertation English corrections.

My friends in Spain and the new friends made in Austria who welcomed me and made me feel at home, especially Peter Brugger for his time, interest and helpful comments for the summary of this dissertation. My growing family, especially my sister Beatriz and my parents, for their love and encouragement from the distance. And most of all, my husband Bernhard who was a pillar during all the stages of this thesis.

And of course, I would finally like to thank those rats used in this thesis who helped with their life to further advance research of Alzheimer's disease.

PhD student Naira P. Martínez Vera received funding from the Medical University of Graz through the PhD Program "Brain Ageing".

Contents

Abbreviations and Definitions

AD	Alzheimer's disease
ApoE	apolipoprotein E
B	magnetic flux density
B_0	static main magnetic field of a magnetic resonance system.
B_1	alternating magnetic field of RF radiation generated by a transmitter coil.
BBB	blood-brain barrier
BS	Bloch-Siegert
BW	bandwidth
CA	contrast agent
CC	corpus callosum
CNS	central nervous system
CSF	cerebrospinal fluid
DAM	double angle method
DESPOT1	driven equilibrium single pulse observation of $T1$
DLB	dementia with Lewy bodies
ETL	echo train length
FA	flip angle
Fe_3O_4	magnetite
FLASH	fast low angle shot
FOV	field of view
FSE	fast spin echo
FTD	frontotemporal dementia
FWHM	full-width at half-maximum
GM	gray matter
GMR	gradient motion re-phasing
GRE	gradient-recalled echo
HC	hippocampus
HSA	human serum albumin
IBMT	Fraunhofer-Institute for Biomedical Engineering
IR	inversion-recovery
M	magnetization
MLNP	magnetically labeled nanoparticle
MRI	magnetic resonance imaging
MUG	Medical University of Graz
Mz	magnetization vector
NEX	number of excitations
NP	nanoparticle
NSA	number of signal averages
PCS	photon correlation spectroscopy
PDI	polydispersity index
PEG	polyethylene glycol
PFA	paraformaldehyde
PRF	proton resonance frequency
PSIR	phase sensitive inversion recovery
Px	pixel
$R1$	$1/T1$; $T1$ relaxation rate
$r1$	$T1$ relaxivity

$R2$	$1/T2$; $T2$ relaxation rate
$R2^*$	$1/T2^*$; $T2^*$ relaxation rate
$r2$	$T2$ relaxivity
RF	radio frequency
ROI	region of interest
SE	spin echo
SEM	standard error of the mean
SEM	scanning electron microscopy
SI	signal intensity
SNR	signal-to-noise ratio
SPGR	spoiled gradient echo
SWI	susceptibility weighted imaging
$T1$	longitudinal relaxation time; spin-lattice relaxation time
$T2$	transverse relaxation time, spin-spin relaxation time
$T2'$	relaxation time caused by static field inhomogeneities
$T2^*$	effective transversal relaxation time
TA	acquisition time
TE	time to echo
THK	thickness
TI	inversion time
TJ	tight junctions
TR	repetition time
TXRF	total reflection X-ray fluorescence
VaD	vascular dementia
WM	white matter

List of Figures

List of Tables

Zusammenfassung

Viele Behandlungsansätze von Alzheimer scheitern an der fehlenden Fähigkeit, die Blut-Hirn-Schranke uneingeschränkt passieren zu können. Nanopartikel sind ein vielversprechendes Instrument um die Blut-Hirn-Schranke zu durchqueren und damit die gezielte Abgabe von Wirkstoffen zu ermöglichen.

Diese Dissertation befasst sich mit dem Tracking und der Quantifizierung von Nanopartikeln mittels Magnetresonanztomographie (MRT). Die MRT-Relaxationszeiten $T1$ und $T2$ von magnetisch markierten Nanopartikeln (magnetically labeled nanoparticle, MLNP) wurden auf einem 3 Tesla System zuerst im Phantom und anschließend in vivo bei Mäusen und Ratten gemessen, um die Auswirkung und Dynamik der MLNP Aufnahme zu untersuchen. Die MLNP-induzierten $T1$-Änderungen in vivo wurden mit Fluoreszenz-Aufnahmen quantitativ korreliert. Zusätzlich zum schnellen *T1*-Mapping, basierend auf der DESPOT1-Sequenz, wurde ein suszeptibilitätsgewichteter Kontrast durch eine Kombination aus Magnituden- und Phasenbildern erzeugt (SWI).

Nach intravenöser MLNP-Injektion konnte eine fokale MLNP-Aufnahme in der Rattenleber und Milz, jedoch nicht im Gehirn beobachtet werden. Weitergehende Histogramm-Analysen von $T1$ und Suszeptibilitätsänderungen bestätigten jedoch eine globale und diffuse Präsenz von MLNPs im Gehirn, welche mit den Ergebnissen der post-mortem Fluoreszenz-Aufnahmen korrelierten. Außerdem wurde die exakte Konzentration von Magnetit im Gehirn nach MLNP-Injektion durch die Suszeptibilitätsverschiebung von Magnetit bestimmt und durch Fluoreszenz-Aufnahmen bestätigt.

Die neuen methodischen Ansätze dieser Dissertation demonstrieren die Machbarkeit der Messung von bereits geringen Mengen an Magnetit-markierten Nanopartikeln in vivo. Diese Methoden könnten zukünftig den Einsatz und die Erforschung von wirkstoffbeladenen Nanopartikeln gegen Alzheimer aber auch andere Erkrankungen des Gehirns unterstützen.

Schlagwörter: MRT, Kontrastmittel, Nanopartikel, Kleine Tiere, Blut-Hirn-Schranke, R1 Relaxationsrate, Suszeptibilitätsgewichtete Bildgebung

Summary

To date, there are no effective treatments to relieve the burden of Alzheimer's disease, which causes cognitive impairment and memory loss for patients. The blood-brain barrier restricts transport of many pharmaceuticals to the brain and therefore they are not useful for immediate treatment approaches. Among different strategies to overcome this barrier, nanoparticles are a promising tool to enhance targeted brain drug delivery. In this thesis, nanoparticles for drug transport in the healthy rat brain were traced with a clinical magnetic resonance imaging (MRI) scanner. In this work, relaxation time mapping and susceptibility weighted MRI were performed on a 3 Tesla system. To trace nanoparticles phantom studies were performed to assess the $T1$ and $T2$ relaxation time constants of magnetically labeled nanoparticle (MLNP) formulations based on biodegradable human serum albumin. In vivo MRI in mice and rats studied the effect and dynamics of MLNP uptake. In the brain, $T1$ changes induced by MLNPs were quantitatively assessed by $T1$ relaxation time mapping in vivo and compared to post-mortem results from fluorescence imaging. Rapid $T1$ mapping in vivo was performed using an optimized DESPOT1-sequence, which also provided susceptibility weighted imaging contrast by a combination of magnitude and phase images.

Following its intravenous injection, MLNP uptake was seen in the rat liver and spleen, while no focal effect was detectable in the brain. However, histogram analysis of $T1$ and susceptibility changes in the brain demonstrated a diffuse presence of MLNPs, which also scaled with post-mortem fluorescence intensity. In addition, the absolute concentration of magnetite in the brain after MLNP injection by utilizing the susceptibility shifting effect of magnetite was determined, which was also confirmed by post-mortem fluorescence intensity.

The novel approaches used in this thesis demonstrate the feasibility of tracking small concentrations of magnetite labeled nanoparticles in the brain of living rodents. These methods could support further research and development of drug loaded nanoparticles in Alzheimer's disease and other disorders of the brain.

Keywords: MRI, Contrast agent, Nanoparticle, Small animal, Blood-brain barrier, R1 relaxation rate, Susceptibility weighted imaging

1 | Introduction

1.1. Framework of this thesis

This section is partly reused from (Martinez Vera et al. 2014)

This thesis was inside of a huge collaborative interdisciplinary approach involving multiple teams ranging from cell biology and medical chemistry to biomedical engineering, where the main goal was the development of drug delivery systems based on nanoparticles (NPs) for the specific transport of Alzheimer's disease (AD) drugs over the blood-brain barrier (BBB). This research resulted from the NanoBrain project which was funded by the ERA-NET Neuron Call "Development and advancement in methods and technologies towards understanding of brain diseases". Grant sponsors: Austrian Science Fund (FWF): I456-B09 and I454-B09, Deutsches Bundesministerium für Bildung und Forschung: 01EW1009 and 01EW1010, and Israel Ministry of Health: 6694.

Specifically, this thesis was carried out within the preclinical magnetic resonance imaging (MRI) group at the Medical University of Graz (MUG) and the main task was to develop an in vivo approach to follow nanoparticle transport in small living animals using a clinical MRI scanner. The synthesis of the nanoparticles for in vivo tracking using MRI was performed using very small superparamagnetic magnetite particles that were incorporated into human serum albumin (HSA) nanoparticles. These protein-based NPs are non-antigenic and biodegradable, making them suitable for in vivo tracking and medical substance delivery (Weber, Kreuter, et al. 2000; Weber, Coester, et al. 2000; Langer et al. 2003). Based on the in vitro testing results obtained by the Fraunhofer-Institute for Biomedical Engineering (IBMT) group and the University of Frankfurt, the suitable nanoparticle formulations were identified for the in vivo testing. In vivo tracking of the nanoparticles was required to ensure that they were indeed capable of passing the BBB in small animals. The Fraunhofer IBMT team and the MUG group collaborated tightly in the development of an optimized formulation. Continuous feedback regarding MR relaxivity and biodistribution was provided to this institute to improve nanoparticle characteristics. The group from JSW Life Sciences GmbH provided and handled the small animals in the in vivo experiments. They also performed the validation of MRI results using fluorescence imaging.

1.2. Alzheimer's disease

Approximately 47.5 million people worldwide[1] have dementia and The World Health Organization predicts that the number of people with dementia will almost double over the next 20 years (Prince et al. 2015) . The term dementia is used to describe a set of symptoms that can vary a great deal but include memory loss, confusion and mood changes. It can be caused by a number of different diseases, usually neurodegenerative diseases, such as AD, frontotemporal dementia (FTD), vascular dementia (VaD) and dementia with Lewy bodies (DLB). With these diseases, the brain cells degenerate and die more quickly than is normal. Damage to brain cells is caused by a buildup of abnormal proteins in the brain, which are different in each type of neurodegenerative dementia (Ritchie & Lovestone 2002). It is important to identify the neurodegenerative disease before the point of disease where pathological damage would stop effective intervention (Figure 1).

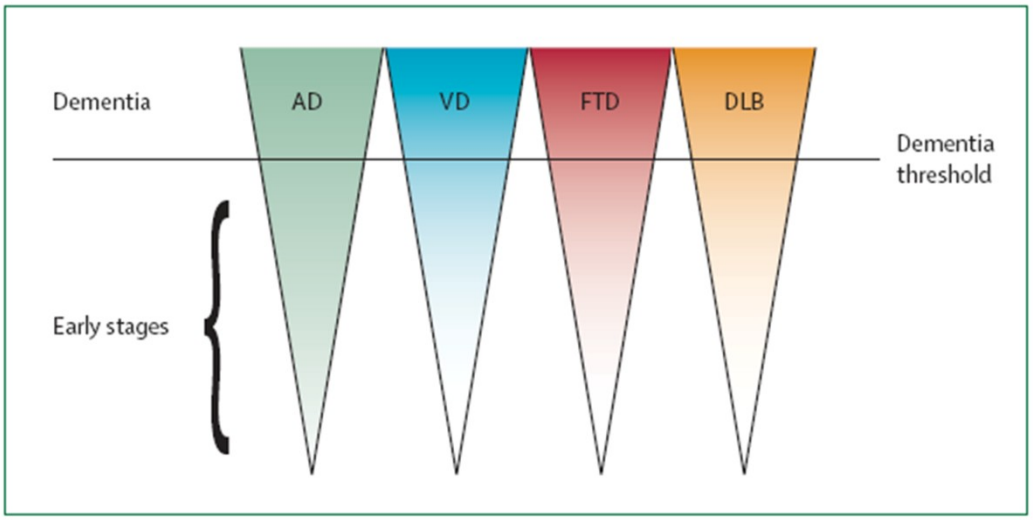

Figure 1. Before dementia occurs, disease early stages are important to be defined as detection of differences for other dementing conditions. AD = Alzheimer's disease; VD = vascular dementia; FTD = frontotemporal dementia; DLB = dementia with Lewy bodies. Reproduced from (Dubois et al. 2007), with permission from Elsevier.

AD is the most age-related neurodegenerative disease in people over the age of 65. Its symptoms include cognitive impairment, disturbance of the sleep-wake cycle and circadian rhythms (Musiek et al. 2015), and dysfunction of metabolism, such as insulin-resistance and mitochondrial dysfunction (Kim & Mook-Jung 2015).

[1] http://www.who.int, last accessed 10.04.2017

Pathologically AD is characterized by intraneuronal neurofibrillary tangles (NFTs), formation consisting of hyperphosphorylated tau and extracellular senile plaques composed of amyloid-β (Aβ) (Alzheimer 1907; Alzheimer et al. 1995) in susceptible brain regions (Hardy 2006), neuroinflammation (Wyss-Coray & Rogers 2012; Wyss-Coray & Mucke 2002) and neuronal and synapses loss. These clumps of proteins, known as tangles and plaques, progressively form in the brain and they are thought to result in the loss of brain cells leading to brain shrinkage. As connections between brain cells are lost there are fewer neurotransmitter chemicals, such as dopamine and acetylcholine, available to carry messages from one brain cell to another (Xu et al. 2012). Dopamine and acetylcholine are thought to play an important role in regulating brain functions, such as memory, learning, mood and attention (El-Ghundi et al. 2007; Wang et al. 2008; Sariñana & Tonegawa 2016). Although risk of AD is thought to be gene and age related (Lardenoije et al. 2015), diagnosis in neurodegenerative dementia is difficult in early stages, when symptoms are subtle and the characteristic syndromic features may not yet completely manifested. The initial cognitive effects of neurodegeneration may also be masked by cognitive reserve, a compensatory mechanism which varies among individuals depending on factors such as education (Xu et al. 2015) and by patient comorbidities (Viatonou et al. 2009). In addition, there is confuse diagnosis in the heterogeneity clinical phenotype of the neurodegenerative cognition (Nasrallah & Wolk 2014).

Clinical observations and cognitive testing have been traditionally used to diagnose AD and to follow its course. Final confirmation of AD relied on the neuropathological characteristics seen in post-mortem brains of AD patients. These include abnormal protein deposits (amyloidosis and NFTs), atrophy (neuron and synapse loss) and gliosis. However, the use of biomarkers in longitudinal observational studies has enabled investigators to establish that AD pathological changes take place decades before the earliest clinical symptom occurs. These changes and clinical decline occur gradually, with dementia representing the end stage of many years of accumulation (Jack et al. 2010; Sperling et al. 2014).

1.3. Nanocarrier approaches to overcome the restriction of the BBB

This section is partly reused from (Martinez Vera et al. 2014)

The blood-brain barrier represents the main obstacle in the treatment of many central nervous system (CNS) diseases because it restricts the transport of many therapeutically important drugs from the blood into the brain, including Alzheimer drugs (Banks 2012) like non-steroidal anti-inflammatory drugs (NSAIDs) (Geerts 2007). The BBB is an important and impermeable physiological barrier in the organism which was showed for the first time by Paul Ehrlich in 1885 in animal experiments after intravenous injection of trypan blue. All tissues were stained except the spinal cord and the brain (Ehrlich 1885). The BBB is mainly constituted by brain capillary endothelial cells which are connected by tight junctions (TJ). The TJ close the aperture that exists between the cells and block the free diffusion of water-soluble polar substances creating a high transedothelial electrical resistance up to 2000 Ωcm^2 (Crone & Olesen 1982; Butt et al. 1990). The brain capillary endothelial cells possess an increased number of mitochondria (great metabolic activity) and they are surrounded by astrocytes, pericytes and nerve endings which maintain an essential part of the characteristic of the BBB (Dyrna et al. 2013). Only some lipophilic, small hydrophobic molecules can cross the BBB by diffusion and some large molecules, peptides and proteins can cross through receptor-mediated specific transport systems (Begley 2003). Therefore, the BBB protects the brain from toxic substances within the bloodstream and keeps the brain's homeostasis stable (Abbott et al. 2006).

Over the past few years a number of different strategies have been devised to overcome this barrier such osmotic opening of the TJs or direct surgical administration of drugs into the brain (Alam et al. 2010). Among different techniques, nanotechnology has emerged as promising tool to enhance brain drug delivery of therapeutic molecules. Numerous recent research works have studied the bio-distribution of many classes of nanoparticles, however additional investigation is needed to clarify how intravenously administered NPs can cross the blood-brain barrier and which capacities are held by the mononuclear phagocyte system to control their uptake (Beduneau et al. 2009; Tu & Louie 2012; Pelaz et al. 2013; Wahajuddin & Arora 2012; Xu et al. 2013; Yokel et al. 2013).

Nanoparticle size, shape, surface charge and surface coating were found to be the main influences in nanoparticle processing and in nanoparticle uptake, including the BBB transition. (De Jong & Borm 2008; Silva 2010; Wahajuddin & Arora 2012; Yokel et al. 2013; Meister et al. 2013). Multifunctional nanoparticles are expected to have a favorable impact and are prepared with a wide range of targeting and imaging agents. Nevertheless each new functionality will come at the cost of production, financial and regulatory hurdles. Consequently, the nanoparticles that reduce these issues are likely to see the most immediate clinical translation (Cheng et al. 2013).

For successful drug delivery, nanoparticles may either modulate BBB integrity or exploit transport systems present on the endothelium (Rempe et al. 2014). In this context, it could be shown that apolipoprotein-modified particles can interact with apolipoprotein receptors at the BBB resulting in their endocytic uptake into endothelium and possibly transcytosis into the brain (Kreuter et al. 2002; Kreuter et al. 1995). This suggestion is supported by the observation that nanoparticles made of HSA with adsorbed or covalently bound apolipoprotein E (Zensi et al. 2009) or apolipoprotein AI (Zensi et al. 2010) transported attached drugs equally well across an artificial BBB (Kreuter et al. 2007). Mechanism studies showed a specific binding and uptake of apolipoprotein-modified HSA nanoparticles on endothelial cells. Moreover, they were able to enter the CNS by transcytosis and were delivered to neurons (Wagner et al. 2012). The kinetic and biological behavior of these kind of nanostructures in living animals have not been yet investigated. The non-invasive nature and high spatial resolution of MRI make this technique highly suitable for detecting in vivo nanoparticles within the body. With the aim of studying nanoparticle organ delivery by MRI, nanomaterial that exhibits a chemical shift (Ward et al. 2000; McMahon et al. 2006; Schröder et al. 2006; Soesbe et al. 2013; Castelli et al. 2013) or paramagnetic or superparamagnetic nanomaterials (magnetically labeled nanoparticles, MLNPs) (Stephen et al. 2011; Wahajuddin & Arora 2012) are needed to be loaded in protein-based nanoparticles because alone this class of NPs does not induce intrinsic MRI contrast.

1.4. Contrast based MRI in small animals using MLNPs

To understand how MLNPs can be detected using MRI, contrast in MRI will be introduced. After that, the advantages and disadvantages of small animal imaging using clinical scanners will be provided.

1.4.1. Image contrast in MRI

The difference between signal amplitudes of different tissues in a MR measurement defines the contrast in MRI. This difference depends firstly on experimental parameters such as selected excitation mode for repetitive excitation of the same spins and on time intervals between several pulses. While on the other hand, signal amplitudes and image contrast are also determined by physical or physiological characteristics of the tissue, such as spin proton density, $T1$ and $T2$ relaxation times which in turn depend on magnetic field strength and the magnetic properties of a tissue.

Bloch Equations

The time dependent behavior of a system of spins under the influence of an external magnetic field $\overrightarrow{B_0}$ is described by the magnetization $\vec{M}$ measured in Ampere/meter (A/m) which is the sum of the magnetic moment vectors of the analyzed nuclei per unit volume of the macroscopic sample.

$$\frac{\overrightarrow{dM}}{dt} = \gamma\left(\vec{M} \times \vec{B}\right) \tag{1.1}$$

The magnetic field $\vec{B}$ measured in Tesla (T) in a magnetic resonance experiment consists of a static magnetic component $\overrightarrow{B_0} = (0,0,Bo)$ in the z-direction and of time dependent component $\overrightarrow{B(t)} = (Bx(t), By(t), 0)$ in the xy-plane orthogonal to $\overrightarrow{B_0}$. γ is the gyromagnetic ratio of the proton (42.576 MHz/T).

It results in the Bloch equations when effects of relaxation due to interaction between spins and between the spins and the environment are treated by the linear time constants $T1$ and $T2$:

$$\frac{dMx}{dt} = \gamma\,(MyBz - MzBy) - \frac{1}{T2}Mx$$

$$\frac{dMy}{dt} = \gamma\,(MzBx - MxBz) - \frac{1}{T2}My \qquad (1.2)$$

$$\frac{dMz}{dt} = \gamma\,(MxBy - MyBx) - \frac{1}{T1}(Mz - Mo)$$

M_0 is determined by the population difference of spins when any magnetic field is applied. The time constants $T1$ and $T2$ describing these relaxation processes are denoted as the longitudinal and transversal relaxation time respectively. In a coordinate system (x', y', z' = z) that rotates about the field direction with the Larmor frequency $\omega_0 = \gamma\, B_0$, the time dependence of the magnetization with respect (x', y', z') is defined by:

$$\frac{dMx'}{dt} = -\frac{1}{T2}Mx'$$

$$\frac{dMy'}{dt} = -\frac{1}{T2}My' \qquad (1.3)$$

$$\frac{dMz}{dt} = -\frac{1}{T1}(Mz - Mo)$$

Longitudinal relaxation ($T1$)

The behavior of the relaxation is influenced by the surroundings (the "lattice") which allows more or less transfer the excess of energy. This environment has very different compositions, thus the nuclear relaxation does not occur at the same way. The process of returning to the equilibrium state is called the spin-lattice relaxation, or longitudinal relaxation, process. The $T1$ relaxation time is the time required for the system to recover to 63 % of its equilibrium value after it has been excited with a 90 ° radio frequency (RF) pulse. The recovery of the longitudinal component of the magnetization Mz is described by the Equation (1.3) where $Mz - Mo$ tends to zero with $e^{-t/T1}$.

Intrinsic and external transverse relaxation ($T2$ and $T2'$)

The surrounding nuclei have influence through the micromagnetic fields on the protons which are precessing in phase when the excitatory RF pulse is applied. After the excitatory RF pulse is switched off, these influences produce a random and irreversible loss of precessing coherence on the xy-plane, meaning some protons' nuclei will precess slower than another one's, depending on the lattice and the local variation of the external magnetic field. This incoherent relaxation is named spin-spin or transversal relaxation process. It is referred to as $T2$ relaxation time when the transversal relaxation depends only on the dipole-dipole interaction between nuclei in the neighborhood. The net transversal component $M_{x'y'}$ exponentially decays with the decay time $T2$, according to next equation:

$$\frac{dM_{x'y'}}{dt} = -\frac{dM_{x'y'}}{T2} \tag{1.4}$$

However, it is referred to as $T2'$ relaxation time when the additional dephasing of the transversal magnetization caused by external field inhomogeneities (ordered and constant) across the volume, is taken into account.

The effective transversal rate is defined by:

$$\frac{1}{T2^*} = \frac{1}{T2} + \frac{1}{T2'} \tag{1.5}$$

To remove the effect of field inhomogeneities, a spin echo (SE) (Hahn 1950) sequence can be used where this de-phasing caused by constant external fields can be re-phased.

$T1$-weighted and $T2$-weighted images

Purely $T1$-weighted or $T2$-weighted images do not exist because the transversal relaxation and the longitudinal magnetization recuperation occur concurrently. This means that all the MR images have a $T1$ and $T2$ component. The scan parameter selection of the pulse sequences determines if an image has $T1$ predominance ($T1$-weighted image) or $T2$ predominance ($T2$-weighted image) or the right combination of both.

Magnetic susceptibility

Magnetic susceptibility is the ability of a substance to become magnetized when placed in an external magnetic field. Susceptibility can be also defined as the measure of the extent to which a substance modifies the strength of the magnetic field passing through it.

When an uniform external magnetic field $\overrightarrow{B_0} = \mu_0 \overrightarrow{H_0}$ is applied to a substance, the actual field $\vec{B}$ inside the material is given by

$$\vec{B} = \mu_0(\vec{H} + \vec{M}) \tag{1.6}$$

And outside the material, the field is given by

$$\vec{B} = \mu_0 \vec{H} \tag{1.7}$$

Where $\vec{B}$ is measured in T, $\vec{H}$-field is measured in A/m, $\vec{M}$ in A/m, and μ_0 is the absolute permeability of free space ($4\pi 10^{-7}$) with units in Tm/A.

When $\vec{M}$ is not constant, so the material is not permanently magnetized, the induced magnetization $\vec{M}$ inside the material may be related to the $\vec{H}$-field by a constant susceptibility χ (dimensionless) through

$$\vec{M} = \chi \vec{H} \tag{1.8}$$

Therefore inside the material,

$$\vec{B} = \mu_0(1 + \chi)\vec{H} \tag{1.9}$$

Based on their macroscopic behavior under the influence of an external magnetic field, materials are classified into diamagnetic, paramagnetic, and ferromagnetic substances. From Equation (1.9), if $\chi > 0$, the material is considered as paramagnetic and if $\chi < 0$, the material is considered diamagnetic. Ferromagnetic substances are permanently magnetized and then Equation (1.6) is used and $\vec{M}$ is a positive constant. Most organic molecules and water are examples of diamagnetic substances. Paramagnetic substances are for example manganese (Mn^{2+}), cobalt (Co^{2+}), iron (Fe^{2+} and Fe^{3+}) and Gadolinium (Gd^{3+}). Molecular oxygen is also slightly paramagnetic in nature. Ferromagnetic particles within

human tissue are unusual and are often found as external, rather than biological, sources (Schenck 1996).

The effect of magnetic susceptibility in MRI can be observed under the presence of different materials with different magnetic susceptibilities, so they can alter the external applied field within and outside these materials. A magnetic gradient field is used to spatially encode so that the precession frequency is known at each location along the gradient. When a gradient field Gx is switched on, the field at the position x is given by:

$$B(x) = Bo + Gx\,.\,x \tag{1.10}$$

With the corresponding Larmor frequency,

$$\omega\,(x) = -\gamma\,(Bo + Gx\,.\,x) \tag{1.11}$$

However, the magnetic field can be perturbed by the presence of magnetic material, such that the net precession frequency of the spins within and outside a substance is influenced by the applied gradient and by the induced field perturbation:

$$B(x) = Bo + Gx\,.\,x + \Delta B(x) \tag{1.12}$$

$$\omega\,(x) = -\gamma\,(Bo + Gx\,.\,x + \Delta B(x)) \tag{1.13}$$

When using gradient echo sequences, during image reconstruction, those spins which are experiencing the additional field perturbation $\Delta B(x)$ are mapped to an incorrect location. In addition to this geometric image distortion, local differences in magnetic susceptibility also cause spins in the same neighborhood to precess at different frequencies. As these spins start to get out of phase with each other, the MR signal within that voxel decreases. These differences in the magnetic susceptibility between substances can provide a very unique imaging contrast if appropriate MR image acquisition and processing methods are used (Haacke & Reichenbach 2011).

MR contrast agents

The goal for magnetic resonance contrast agents (CAs) is to change signal intensity and consequently the contrast of the image. The main contrast agent mechanism in MR imaging are changes in proton density, relaxation times, magnetic susceptibility and resonant shift frequency (Graves 2007). As it is difficult to manipulate the water content of a tissue, contrast agent research focus on relaxation time or magnetic susceptibility (Geraldes & Laurent 2009). This work focuses on contrast agents that are injected into the blood torrent and they have influence on H^1 nucleus relaxation times. These contrasts are characterized in terms of the presence of a metallic ion as an active agent which accelerates the nuclei energy relaxation ($T1$ decreases), increases the asynchrony proton nuclei relaxation ($T2$, $T2^*$ decrease) and causes a greater effect on local magnetic field inhomogeneities, resulting in higher susceptibility differences in susceptibility weighted imaging. The term relaxivity explains the variations of $T1$ and $T2$ and instead of working with $T1$ or $T2$ values, it uses the inverse values $1/T1$ and $1/T2$, which are called longitudinal relaxivity index ($R1$) and transversal relaxivity index ($R2$). Both increase when a contrast agent substance is injected. In a simple form, for a given external magnetic field and with fixed temperature conditions, the increase of $R1$ and $R2$ lineally depend on the CA concentration:

$$\begin{aligned} R1 &= R1^0 + r1\, C_{CA} \\ R2 &= R2^0 + r2\, C_{CA} \end{aligned} \tag{1.14}$$

C_{CA} is the contrast agent concentration expressed in mM. $r1$ and $r2$ are the relaxivity values, i.e., the effective relaxation rate of $R1$ and $R2$ as a function of C_{CA}. For given $R1$ and $R2$ values before administration of contrast agent ($R1^0$, $R2^0$), there is more contrast repercussion when higher $R1$ and $R2$ values are obtained after administration of the CA.

The principal goals for the development and use of MR contrast agents are the improvement of tissue contrast, tissue characterization, overall sensitivity and specificity. It is also important to reduce image artifacts, imaging time and overall costs. Another significant issue in using contrast agents is the requirement of

adequate relaxivity, susceptibility, osmolality, biodistribution, tolerance, stability, elimination, metabolism and toxicity. These research aspects are mainly investigated in rodent animal studies.

1.4.2. MRI pulse sequences

Here an overview of the sequences used in this thesis for MLNP characterization and localization will be provided.

Inversion-recovery sequence:

To measure the $T1$ relaxation times, an inversion-recovery (IR) sequence was used. In IR, the magnetization M_0 is inverted by a 180 ° RF pulse. Following the inversion, the magnetization starts to recover towards its equilibrium state. The rate of recovery is determined by $T1$. The subsequent 90 ° RF pulse which is applied after a certain delay time, called the inversion time TI, flips the magnetization to the xy-plane. The sequence is repeated after a repetition time TR sending a new 180 ° pulse:

$$Mz(TI) = Mz(0) \times (1 - \rho \times e^{-\frac{TI}{T1}}) \tag{1.15}$$

$Mz(TI)$ is the signal measured at time TI, $Mz(0)$ is the signal that would be obtained from the equilibrium longitudinal magnetization and $\rho\,(= 1 - \cos\theta)$ is another constant with a value around 2 (the inversion pulse is imperfect and is not always exactly 180 °).

Multi-echo gradient-recalled echo (GRE):

In GRE-sequences a gradient echo, Mxy, is built up at the echo time TE, by de- and re-phasing the frequency encoding readout gradient. Multi-echo GRE-sequences are rapid sequences which are produced when, after a single RF-pulse, more additional reversal gradients are created in the same TR interval. Multiple GREs are feasible as long as the transverse magnetization by $T2$* relaxation is not completely lost. Particularly, Fast Low-Angle Shot (FLASH) sequence is a GRE using small flip angles (FAs). For this kind of sequences, a residual Mxy at the end of TR is spoiled and the resultant signal of the steady state is given by:

$$Mxy = \frac{Mz(0)\ \times (1 - E_1)\, sin\ (\alpha_T)}{1 - E_1\, cos\ (\alpha_T)} exp\left(-\frac{TE}{T2^*}\right);\ E_1 = \ exp\left(-\frac{TR}{T1}\right) \quad (1.16)$$

Where $Mz(0)$ is a factor proportional to the equilibrium longitudinal magnetization and α_T is the real transmitted flip angle. This kind of sequence accelerates acquisition times and is frequently used for fast $T1$- and $T2^*$-weighted imaging. Therefore, it is very sensitive to field inhomogeneities due to the presence of a superparamagnetic material such as magnetite nanoparticles.

DESPOT1 (driven equilibrium single pulse observation of $T1$):

DESPOT1 relaxometry method is used for rapid $T1$ mapping and was originally introduced in 1974 by Christensen using the variable nutation angle method (Christensen K.A. et al. 1974). The method obtains $T1$ by establishing a spoiled steady state followed by the collection of spoiled gradient echo (SPGR) images acquired with constant TR, short TE and over a series of two or more incremented FAs (Deoni et al. 2003; Deoni et al. 2004).

Therefore the general SPGR signal equation is given by:

$$S_{SPGR} = \frac{Mz(0)\ \times (1 - E_1) \sin\ (\alpha_T)}{1 - E_1 \cos\ (\alpha_T)};\ E_1 = \exp\left(-\frac{TR}{T1}\right) \quad (1.17)$$

This equation can be written in a linear form (Y = slope X + intercept):

$$\frac{S_{SPGR}}{\sin\ (\alpha_T)} = \frac{S_{SPGR}}{\tan\ (\alpha_T)}\ E_1 + \ Mo(1 - E_1) \quad (1.18)$$

Plotting $S_{SPGR}/\sin\ (\alpha_T)$ versus $S_{SPGR}/\tan\ (\alpha_T)$ allows $T1$ to be calculated from the slope of this line as:

$$T1\ = \text{-TR} / \ln\ (\text{slope}) \quad (1.19)$$

B_1 mapping

The dominant source of error in the accuracy of the DESPOT1 is the imprecise knowledge of the flip angles used, due mainly to the inhomogeneities in the RF field that excite the spins (B_1-field). Therefore, the choice of FAs can significantly affect the precision and accuracy of the derived $T1$ values. At high field strengths like 3 T or above, uniformity of the RF-field cannot be ensured (Deoni et al. 2004;

Deoni 2007). As a consequence, the real angle transmitted (α_T) will be the prescribed angle (α_P) affected by a factor k:

$$\alpha_T = k \times \alpha_P \tag{1.20}$$

Where k indicates the spatial variation of the B_1-field. Therefore, to obtain the desired flip angle, calibration of the B_1-field is necessary. B_1 calibration methods include theoretical modeling of the FA profile through finite element simulations of the coil and tissue compartment, the use of adiabatic or composite RF pulses to provide a more uniform B_1 profile, or direct mapping of the B_1-field from acquired image data. B_1 mapping methods are divided in two categories, magnitude-based and phased-based maps. Double Angle Method (DAM) is the standard magnitude based method (Insko & Bolinger 1993; Hornak et al. 1988; Stollberger & Wach 1996).

If we consider DAM, the signal intensity $I(x)$ of a spin echo sequence without transversal coherence and non-interacting spins is written by:

$$I(x) = k \times \rho(x) \times S(x) \times \sin\alpha(x) \times \sin^2\frac{\beta(x)}{2} \times R1\big(\alpha(x), \beta(x), TR, TE, T1(x)\big) \times e^{\frac{-TE}{T2(x)}} \tag{1.21}$$

where $\alpha(x)$ is the excitation angle, $\beta(x)$ the flip angle of the refocusing angle, $\rho(x)$ the spin density, k a system constant, $S(x)$ the coil sensitivity and $R1\big(\alpha(x), \beta(x), TR, TE, T1(x)\big)$ a term describing the longitudinal relaxation. To avoid this term, it is acquired with very long TR in order to remove the $T1$ effect.

Then,

$$I(x) \propto k \times \rho(x) \times S(x) \times \sin\alpha(x) \times \sin^2\frac{\beta(x)}{2} \times e^{\frac{-TE}{T2(x)}} \tag{1.22}$$

$$\frac{I1(x)}{I2(x)} = \frac{\sin\alpha1(x)}{\sin\alpha2(x)} \tag{1.23}$$

$$, if\ \alpha1(x) = 2 \times \alpha2(x)\ then,$$

$$\sin 2\alpha(x) = 2 \times \cos\alpha(x) \times \sin\alpha(x) \tag{1.24}$$

$$\frac{I2(x)}{I1(x)} = 2 \times \cos \alpha(x) \qquad \alpha(x) = arccos\left(\frac{I2(x)}{2 \times I1(x)}\right) \tag{1.25}$$

However, DAM takes a long time to acquire because TR needs to be longer than $5 \times T1_{max}$, where $T1_{max}$ is the longest $T1$ time occurring within investigated object. Therefore, other approaches have been proposed to speed up B_1 map calculation including the phase-based method Bloch-Siegert (BS) shift which is widely used (Sacolick et al. 2010). There is a phase shift (φ_{BS}) in spin precession frequency when an off-resonance pulse ω_{RF} is applied (Bloch & Siegert 1940):

$$\begin{aligned} \varphi_{BS} = \int_0^T \omega_{BS}(t) &= \int_0^T \frac{\left(\gamma \times B_1(t)\right)^2}{2 \times \omega_{RF}(t)} \\ &= {B_{1,peak}}^2 \times \int_0^T \frac{\left(\gamma \times B_{1,normalized}(t)\right)^2}{2 \times \omega_{RF}(t)} dt \end{aligned} \tag{1.26}$$

$$\varphi_{BS} = {B_{1,peak}}^2 \times k_{BS} \tag{1.27}$$

Where $B_{1,peak}$ is the magnitude of the maximum point in the RF waveform $B_1(t)$:

$$B_1(t) = B_{1,peak} \times B_{1,normalized}(t) \tag{1.28}$$

And k_{BS} is a constant that describes the phase shift (radians/gauss^2) for a given RF pulse. The Bloch-Siegert frequency shift ω_{BS} results in a ${B_1}^2$-dependent phase φ_{BS}.

Susceptibility weighted imaging (SWI)

SWI is a $T2^*$ technique that exploits the magnetic properties of tissues and enhances local contrast by using phase information (Haacke & Reichenbach 2011). SWI uses magnitude and phase images obtained with gradient echo sequences. Signals from substances with different magnetic susceptibilities compared to their neighboring tissue will become out of phase with these tissues at sufficiently long echo times. Specifically, phase images are used to enhance contrast between tissues with different susceptibilities. In SWI, such phase images are used to alter the contrast in the magnitude images. For that, several steps are taken. First, a high pass filter is applied to the phase image to remove the low-

spatial frequency inhomogeneities of the background field and air/tissue interfaces (Wang et al. 2000). Second, this filtered phase image is used to create a mask $f(x)$ that is used to multiply n times the original magnitude image $\rho(x)$ to create novel contrast in the magnitude image ($SWI(x)$):

$$SWI(x) = f^n(x) \times \rho(x) \tag{1.29}$$

1.4.3. Contrast enhancing magnetic nanoparticles

This section is partly reused from (Martinez Vera et al. 2014)

Strong microscopic field gradients are produced by contrast enhancing magnetic NPs providing a high magnetic susceptibility. As a result, $T1$ relaxation is accelerated due to dipole-dipole interactions (positive contrast) and the effective loss of the transversal magnetization of the free induction decay ($T2$* relaxation) is also accelerated due to dephasing effects in the field gradients (negative contrast).

Iron oxide magnetic NPs are widely used to create negative contrast agent due to their high relaxivity $r2$, biocompatibility and long circulation time in the body (Lee et al. 2012; Zhao et al. 2013; Xing et al. 2013). Nevertheless, their negative contrast effect is often confused with low-level signals from bleeding, calcification or metal depositions and their magnetic susceptibility artifacts (signal drop is much larger than the area of MLNPs accumulation) distort the background image. Additionally, due to the faster signal decay on clinical scanners using small animals, the quantitative assessment of negative contrast effects is also more difficult. For these reasons, the development of new $T1$ contrast nanoparticles with a $T1$ contrast effect and nanostructural characteristics is of great interest (Hu & Zhao 2012; Zhu et al. 2013). Paramagnetic nanoparticles which are usually Gd- and Mn-based nanoparticles, are normally used as positive contrast (Boros et al. 2012; Zhou et al. 2013; Na et al. 2007; Zipfel et al. 2003; T. Kim et al. 2011; J. Yu et al. 2012). However, toxicity still persists due to their accumulation and synthesis difficulty is also a challenge to overcome their short signal duration, which is too short for long-term in vivo MR contrast enhancement. Therefore, new research is focused on the development of iron oxide nanoparticles as positive contrast agents for biomedical applications due to their excellent biocompatibility and ease of synthesis (B. H. Kim et al. 2011; Hao et al. 2013; Tromsdorf et al. 2009).

Magnetite and maghemite are the most used superparamagnetic contrast agent, with magnetite being preferred due to its higher magnetic properties and biocompatibility. Magnetite (Fe_3O_4) is a ferrimagnetic compound that exhibits superparamagnetic behavior when spherical magnetite nanoparticles are under some conditions such as a small diameter (< 20 nm) (Rümenapp et al. 2012). Superparamagnetic particles have no net magnetization if no external field is applied but their magnetic saturation is comparable with ferromagnetic particles (Rümenapp et al. 2012; Stephen et al. 2011; Gossuin et al. 2009; Wahajuddin & Arora 2012).

The MRI system is a complex function of a number of factors including coil sensitivity, pulse sequence and field strength that together with the relaxivity of the MLNPs limits the sensitivity for probing very small amounts of magnetically labeled nanoparticles. Consequently, improvement of MRI acquisition and post-processing methods are currently in development with the purpose of achieving shorter acquisition times and a better image contrast (Stephen et al. 2011; Herrmann et al. 2012; Brisset et al. 2011; Pillai et al. 2011; Zhang et al. 2011; Huang et al. 2012; Eibofner et al. 2010).

1.4.4. Animal MRI on clinical scanners

MR imaging using dedicated ultra-high field (4.7 T and above) animal scanners allows high spatial resolution (30 μm or higher) with excellent soft tissue contrast (Marzola et al. 2003). However, there are some advantages in MRI of small animals using clinical scanners. Clinical whole-body scanners are often more easily available than the relatively expensive dedicated high field strength, small bore animal MR scanners. Another advantage is that an animal imaging at clinical field strengths (1.5 T or 3 T) is closer to human imaging, enabling a more direct translation of these studies to human research. Additionally, the contrast generating effects of many $T1$-shortening agents, are reduced at ultra-high field strengths (Brockmann et al. 2007; Herrmann et al. 2012; Pillai et al. 2011). However, scanning small animals using clinical scanners also has a number of restrictions, making such procedures more elaborate than in humans. Physiology monitoring (respiration, temperature, cardiac, and blood pressure), gas anesthesia, heating and nanoparticle injection systems are similar to those used in

dedicated small animal MR systems. Since the respiration rate and cardiac cycle are much faster than in humans, the built-in physiology monitors in clinical systems do not usually work without additional hardware and software. Such additional hardware is usually stored in the control room with hoses and connections led into the magnet room through waveguides and connections. A clinical scanner is designed for a human, which is on average in volume approximately 4000 times larger than a mouse and around 270 times larger than a rat. Larger magnets limit the field strength, larger gradient coils result in weaker and slower magnetic field gradients for spatial encoding, and larger radio frequency coils results in very low filling factors. All these aspects translate to a large reduction in image quality in terms of signal-to-noise ratio (SNR), spatial and temporal resolution when compared to a small animal system. SNR represents the total detected MR signal normalized by the overall noise. This limitation is found in small objects performed using clinical MRI. The smaller the voxels are, the lower the amount of signal that can be obtained from each voxel although the noise remains the same. Consequently, SNR depends on the voxel size of the acquisition and low SNR leads to reduced image quality. This SNR restriction can be compensated at the expense of spatial resolution. Increasing all three voxel dimensions by 25 % compensates for a difference of factor 2 in field strength. Signal averaging is another solution. The SNR, which is proportional to the square root of the number of signal averages (NSA), improves as the NSA increases, but scan times also increases linearly with NSA. The gradient system is critical to the spatial resolution and scanning speed, so the lower gradient strength and lower gradient slew rate available on clinical systems is another limitation. Clinical scanners have a typical gradient strength of 40 mT/m and slew rates up to 200 T/m/s compared to gradients of 700-1000 mT/m and slews rates up to 5000 T/m/s in animal scanners. This also limits the minimum slice thickness and field of view (FOV). Sensitivity performance can be gained with some sequences by increasing the minimum refocusing time and repetition time, meaning TE and TR are longer when scanning a mouse compared to a human scan.

1.5. Aim of work

The main goal of this thesis was to develop a novel in vivo approach to follow nanoparticle transport in small living animals using a clinical MRI scanner. To achieve this purpose, the potential of magnetite labeling for making HSA NP traceable with MRI was explored in phantom studies and in vivo studies using mice and rats.

The following aims were addressed:

A) Firstly, to assess the relaxivities of different MLNP configurations and with that, to identify the most appropriate nanoparticle for in vivo experiments. Here the specific objectives were to:

- establish a phantom MRI scan protocol; and

- optimize MRI sequences for magnetic loaded nanoparticles characterization.

B) In addition, to look for body distribution patterns of the NPs in vivo experiments in mice and rats, to test if the relaxivity and susceptibility effect in the brain is high enough to allow in vivo tracking and afterwards to quantify the magnetite concentration present in the brain.

This involved the following detailed objectives:

- Establishment of an in vivo MRI scan protocol;

- Optimization of MRI sequences for the animal experiment; and

- Development of novel, sensitive and selective post analysis techniques to investigate the dynamics of NP accumulation in the brain.

C) Confirm and validate the MRI findings with fluorescence imaging.

2| Material and Methods

In this section, the relaxivities of different MLNP models are assessed in small samples in order to select the best candidate for in vivo studies. In vivo tracking of the nanoparticles is required to ensure that MLNPs are indeed capable of passing the BBB. Animal setup configurations and MRI sequences are optimized for in vivo abdominal and brain imaging using rodents. Body imaging is optimized to obtain high SNR, high contrast and to avoid motion artifacts. MLNP-induced changes in the brain are analyzed by $T1$ mapping and SWI. Generation of $T1$ maps is performed using the gold standard IR-sequence and using an optimization of a rapid $T1$-weightened sequence (DESPOT1). As changes in the brain after MLNP injection cannot visually be detected, $T1$ and SWI values are analyzed with a histogram technique where the mean values of the main brain components are represented. In order to compare images obtained before and after injection, post-processing data may include brain segmentation and registration. The final aspect is to calculate the concentration of the magnetite that reaches brain. For that, the relaxivity rate in the rat brain before and after the administration of the CA and the change of $T1$ with temperature is taken into account. The temperature of the rat brains is calculated through phase mapping using proton resonance frequency shift. To validate MRI results, histological studies are performed using fluorescence image. For that, $T1$, SWI and magnetite concentration values in the brain are correlated with the mean fluorescence signal in the investigated rat brain regions.

The description of Materials and Methods is partly reused from (Martinez Vera et al. 2014)

2.1. Nanoparticle preparation

The Fraunhofer IBMT and the University of Frankfurt were in charge of the development and synthesis of NPs as future AD drug carriers (protocol is described in detail in Appendix A). These NPs were based on HSA and for in vivo tracking using MRI, the nanoparticles were developed by additional incorporation of very small magnetite nanoparticles (MLNPs). Some of the MLNPs for the in vivo studies were as well labeled with polyethylene glycol (PEG). Different studies demonstrated that coating their surface with different hydrophilic surfactants such as PEG polymer increased MLNP blood circulation time thus avoiding their fast

clearance by the mononuclear phagocyte system (Jokerst et al. 2011; Naahidi et al. 2013). The resulting MLNP size and the magnetic NP size of the entrapped magnetite were the two main characteristics to improve in the MLNP preparation process. This methodological description was also published in an original article (Martinez Vera et al. 2014).

2.2. Methods used to asses MLNP relaxivity

The different MLNP models (Table 7) were analyzed in small samples (2 mL solution) containing distilled water and the desired magnetite concentration (mM). MLNP concentration in the samples was modified depending on the relaxivity response. This methodological description was also published in a similar fashion in an original article (Martinez Vera et al. 2014).

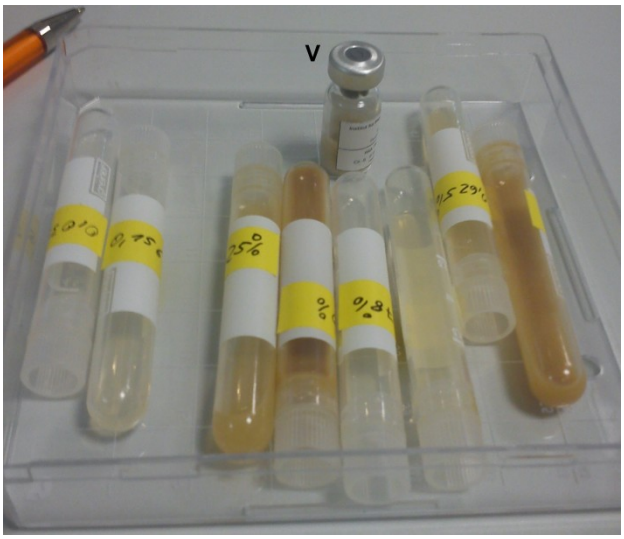

Figure 2. Example of a nanoparticle model prepared in small samples containing different magnetite concentrations. Samples with higher magnetite concentration demonstrated a darker color than those with only a low concentration. MLNPs were received in vials like the one in the image (v).

2.2.1. Data acquisition and mapping of relaxation properties

MRI scans were performed on a conventional clinical 3 T scanner (Tim Trio, Siemens Healthcare, Germany) and an 8-channel knee coil was used for signal reception (Siemens). The use of the knee coil which has a large, homogeneous transmit coil with a local surface receive coil, minimized RF pulse errors whilst maintaining high local SNR. Acquiring signal originating from the samples in the scanner was possible due to the use of a water bottle next to the samples which

led to higher SNR. However, a gel phantom was selected for use in the experiments instead of pure water because of the image artifacts induced in pure water due to patient table movements. Nanoparticle detection was also improved when samples and the bottle were placed in the center of the knee coil. Furthermore, the positioning indicator light in the scanner was aligned with the bottle so the high signal coming from the bottle was always at the isocenter of the B_0 magnet from the scanner.

Nanoparticles containing superparamagnetic materials give rise to much larger local magnetic fields and strong dipolar interaction, and hence much more rapid longitudinal relaxation. Therefore, the effect of $R1$ increases and pulse sequences that minimize $R2$ influence are needed. $T1$ mapping was first determined using a single slice, 2D IR-sequence and data was collected at different TI and fast readout. For each MLNP model, sequence parameters are summarized in Table 1. The experimental data was fitted by finding the values of $T1$ that minimized the difference between the modeled curve and the measured signal $Mz(TI)$. This was done using a three parameter nonlinear, least-squares fitting (chi-squared minimization) algorithm using the curve fitting tool toolbox from Matlab R2011 to solve the Equation (1.15) for $Mz(0)$, ρ and $T1$. This methodological description was also published in a similar fashion in an original article (Martinez Vera et al. 2014). The susceptibility inhomogeneity from the presence of the superparamagnetic nanoparticles was analyzed using a clinical 2D $T2$*-weighted sequence (multi-echo GRE) with a number of evenly spaced echoes. Relatively short echo times were required, as a faster signal decay was expected due to field inhomogeneities produced by the magnetite nanoparticles. For each MLNP model, sequence parameters are summarized in Table 1.

Table 1. Sequence parameters used for $T1$ and $T2$* mapping in phantom measurements.

Sequence	TR /ms	TI /ms	TE /ms	FOV	FA /º	Px size /mm^2	Px BW /Hz/px	Slice THK /mm
$T1$-weighted 2D IR	5000	50, 100, 200, 400, 800, 1600, 3200	9.2	256×152	180	0.5×0.5	349	2
$T1$-weighted 2D DESPOT1	20	-	3.3	256×152	5,10,15, 20,25	0.5×0.5	331	2
$T2$*-weighted 2D GRE	300	-	4.9, 9.9, 14.7, 19.6, 24.6, 29.6	256×152	30	0.5×0.5	190	3

TR = Repetition time; TI = Inversion time; TE = Echo time; FOV = Field of view; FA = Flip angle; px = Pixel; BW = Bandwidth; THK = Thickness

$T1$ and $T2$* relaxometry maps were analyzed with MRICRO software[2]. A selected subset inside each sample was defined and the mean of this region of interest (ROI) was used to calculate the mean relaxometry value of each sample concentration. As a last step, the relationship between the relaxation rates and magnetite-load nanoparticle concentration was modeled using regression analysis.

2.2.2. DESPOT1 measurements

A second target was the improvement and optimization of a rapid $T1$-weighted sequence with high sensitivity for the labeled nanoparticles and high contrast to noise ratio under preservation of spatial resolution. For this purpose, high resolution $T1$-weighted sequence 2D DESPOT1 was developed (Table 1). Phantom $T1$ values were calculated as a unique solution for $T1$ and $Mz(0)$ using least-squares minimization of Equation (1.19) (curve fitting tool toolbox from Matlab R2011). IR $T1$ values were used as reference values to analyze $T1$ values obtained with DESPOT1-sequence.

[2] http://www.mccauslandcenter.sc.edu/crnl/tools, last accessed 18.04.2016

DESPOT1 optimization

New examinations using a gel phantom were performed to investigate and correct $T1$ values obtained from 2D DESPOT1 measurements. These experiments were conducted using the body-coil for RF transmission and a 32-channel phased array head coil (Siemens) for signal reception. Sequence parameters of these experiments are summarized in Table 2. 2D IR-sequence was used to obtain the reference (phantom) $T1$ values.

- B_1 measurement and correction of $T1$ values

First, B_1 inhomogeneities were corrected. Two DAM images were acquired using SE-sequences with same scan parameters but different nominal excitation angles. TR was selected to be equal and greater than five times the longest $T1$ time of the sample. The real FA transmitted was calculated using the ratio of the two DAM images using the Equation (1.25) and the k correction factor was calculated using Equation (1.20). To avoid the long scans for B_1 mapping using DAM, the Bloch-Siegert shift fast B_1 mapping method was also performed. In this method, an RF pulse at off-resonance frequency ω_{RF} = 8 kHz was placed into a spoiled GRE imaging sequence following excitation. Two images were acquired with the pulse applied symmetrically around the water resonance at $\pm\,\omega_{RF}$. The phase difference between these two images was proportional to the square of the B_1 magnitude and the k correction factor (Equation (1.27)). Bloch-Siegert B_1 mapping was programmed by Andreas Petrovic at the Institute of Medical Engineering of the Technical University of Graz. DAM and BS shift k maps were registered to a reference magnitude image obtained from DESPOT1-sequence using FLIRT (FMRIB's Linear Image registration Tool[3]) from FSL library (M. Jenkinson & Smith 2001; M. Jenkinson et al. 2002). $T1$ maps were then calculated using the corrected flip angles (Equation (1.20)).

The next step involved the evaluation of the influence of the flip angle selected for $T1$ mapping and examination of the precision of $T1$ mapping using just two flip angles. For this purpose, different $T1$ maps were calculated using a standard set

[3] www.fsl.fmrib.ox.ac.uk/fsl/fslwiki/FLIRT, last accessed 14.04.2016

of uniformly spaced angles (5 º, 10 º, 15 º, 20 º, 25 º) and a series of FA pairs (5 º and 10 º, 5 º and 15 º, 5 º and 20 º, 5 º and 25 º). For $T1$ map calculation, all FAs were corrected with the BS shift method. The slope resulting from the different linear fits (Equation (1.18)) and the $T1$ values versus this slope were examined (Equation (1.19)). 3D DESPOT1 was also studied in order to reduce the scan time and to improve the SNR. For this last study only 2 flip angles were used (Table 2).

Table 2. Sequence parameters used for $T1$ optimization and B_1 mapping. IR-sequence was used to have reference $T1$ values. DAM and BS shift were employed to measure B_1 maps and to correct the $T1$ values obtained with DESPOT1-sequences.

Sequence	TR /ms	TI /ms	TE /ms	FA /º	Voxel size /mm
Localizer	8.6	-	4	20	0.4×0.4×6
$T1$-weighted 2D IR	5000	50,100,150, 200,300,400, 600,800	18	180	0.6×0.6×4
$T1$-weighted 2D DESPOT1	20	-	3.29	5,10,15,20,25	0.6×0.6×4
$T1$-weighted 3D DESPOT1	10	-	4.2	3,19	1.3×1.3×1.3
B_1 mapping 2D DAM (SE)	10000	-	12	60,120	1.3×1.3×4
B_1 mapping 2D BS shift	60	-	12	15	2.6×2.6×4
TR= Repetition time; TI= Inversion time; TE= Echo time; FA = Flip angle					

Finally, samples containing magnetite were acquired with the sequence parameters obtained from DESPOT1 optimization results (Table 9).

2.3. Methods used to track the nanoparticles in vivo

All measurements were performed on a clinical 3 T scanner (Trio Siemens) equipped with a system capable of generating maximum gradient amplitude of 40 mT/m with a slew rate of 180 mT/m/ms. Different approaches were implemented in order to overcome the low SNR obtained from small rodents and to trace the nanoparticles in vivo. In this thesis, first mice and then rats were used. Animal fixation, supply of the anesthesia, NP administration and temperature control were implemented in different forms depending on the animal used in the experiments (Figure 3 and Figure 5). The MRI scanner setup and scanning protocol were used

to investigate nanoparticle uptake in the small animals with a series of measurements which allows the study of dynamics of labeled nanoparticles regarding local distribution and accumulation over time.

Ewald Auer and Balázs Dobrovich (JSW Life Sciences GmbH) handled the small animals in the in vivo experiments.

Animal studies conformed to the Austrian guidelines for the care and use of laboratory animals and were approved by the Styrian Government (FA10A-78Jo-98-2012).

2.3.1. Mouse study protocol

Month-old male adult healthy mice (n = 5) were used in these experiments. RF coils, animal setup and MRI sequences were analyzed using two of the mice. The other three served to explore the accumulation of MLNPs in the brain and body following intravenous injection of 70 µL (140 µg) MLNPs via the tail vein.

RF coils

Mouse experiments were carried out with two RF coils, one for abdominal imaging and another one for brain imaging (Figure 3A). For abdominal imaging, a NORAS CPC Multipurpose coil 3 T was used. The CPC is a multifunctional 8-channel coil pair with a holder which ensures correct positioning of the coil. Each coil half is configured as a 4-channel array. This 2-element surface coil was equipped with a highly flexible mounting system that enabled rotation and tilt of the two modules as well as rotation and translation of the mounting arms to nearly any required position (Figure 3C). For brain imaging a microcoil with an inner diameter of 30 mm and brain amplifier was used (Figure 3D). The MR scanner was also provided with a physiological triggering and gating, a prerequisite for high resolution 3D imaging in small animals.

Animal setup

Mice were initially anesthetized in an anesthesia induction chamber for ten minutes using a gas mixture of oxygen (1.8 %) and isoflurane (1.8 %) before being placed into the scanner. After that, the mice were placed on the MRI scanner bed in the prone position using a plastic mouse bed holder. During the experiments, the same mixture of oxygen and isoflurane was transported from a gas vaporizer situated outside the scanner through cables to the snout of the rodent. Fixation and anesthesia supply was given to the animal through a mouse anesthesia mask. Secreted waste was transported away via air pressure controlled tube. The plastic mouse bed holder also was provided with a custom-builtair-heated bed to maintain the core temperature of the animal (Figure 3B). The mouse's abdomen was positioned directly on the lower coil module of the 2-element surface coil and the upper module on the mouse's back. During the measurements, the half coils were positioned close to the animal allowing enough space for the animal's breathing (Figure 3C). At the same time the dedicated microcoil was positioned just above the mouse's head (Figure 3D). Two bottles containing a gel mixture were placed on both sides of the lower half coil to facilitate the detection of the signal originating from the mouse (Figure 3C).

MRI sequences

First of all, localizer sequences using the body coil were applied in order to find the mouse into the scanner. Afterwards, the following sequences were applied depending if the exam focused on the brain or the abdomen of the animal.

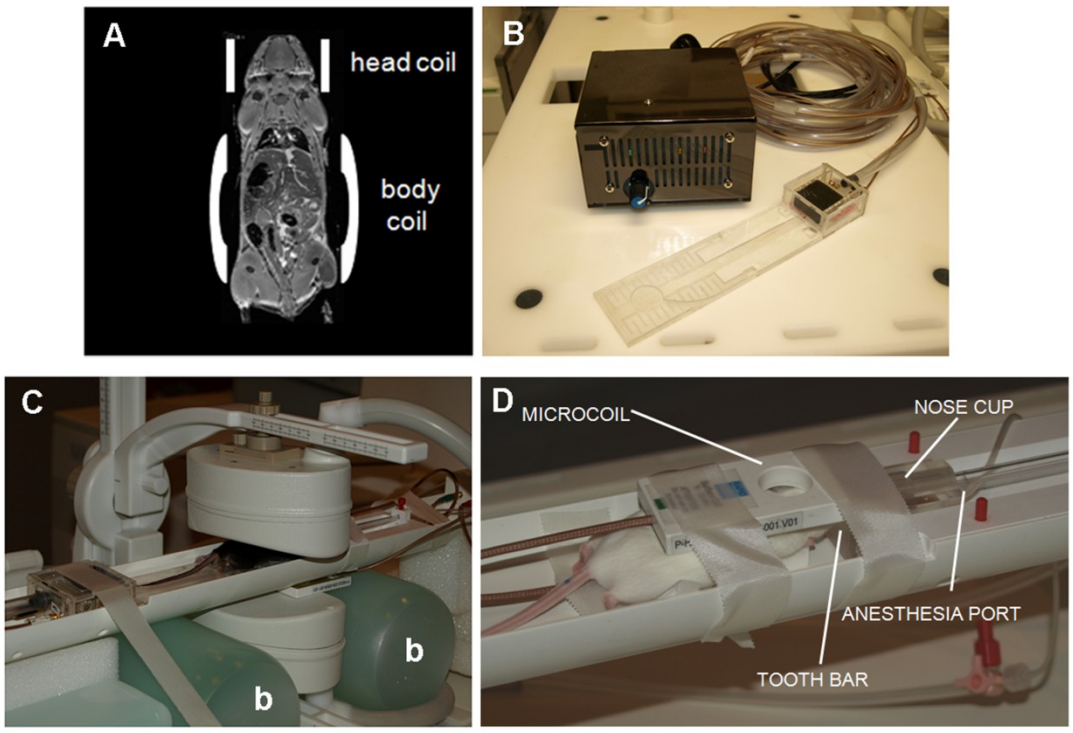

Figure 3. MRI animal setup when optimizing MRI sequences in mice. (A) Head and body coils were used in both brain and abdominal imaging. (B) A custom builtair-heated bed was used to maintain the core temperature of the animal. (C) A surface coil was used in abdominal imaging and (D) a microcoil in brain imaging. Two bottles of a mixture gel (b) were placed close to the animal to better detect the signal originating from the mouse in the clinical scanner.

- Abdominal imaging

Abdominal imaging is affected by artifacts due to motion from respiratory, cardiac, gastrointestinal and involuntary animal movements. In this section, sequences were adjusted to obtain high SNR, high contrast and to avoid these motion artifacts.

Initially body scans were performed using 3D FLASH MRI sequence. The scan parameters are summarized in Table 3. In these measurements, the re-phasing gradient (Gradient Motion Rephasing, GMR) was switched on for flow compensation and selective fat-saturation option was also used for suppress fat throughout the entire image which led to artifact reduction. Since images using FLASH sequence still contained motion artifacts, 2D phase sensitive- IR (PSIR) fast spin echo (FSE) was used to optimize body imaging. Here, each IR pulse was followed by a FSE readout sequence (Table 3) with an echo train length (ETL) of 5. As in the previously mentioned FLASH measurements, fat saturation and flow compensation were also switched on. Artifacts caused by motion due to breathing

were reduced using a spatial saturation slab on the region of the lungs. All data sets were acquired in coronal orientation relative to the rodent head.

Table 3. Sequence parameters used for mouse body imaging.

Sequence	TR /ms	TE /ms	TI /ms	Acquisition matrix	FA /º	Voxel size /mm^3	Px BW /Hz/px	NEX
3D FLASH	40	7.23	-	128×256×30	25	0.47×0.47×1	199	4
2D PSIR FSE	5000	9.20	50,100 ,200	180×256×10	180	0.39×0.39×1.44	320	3
TR = Repetition time; TE = Echo time; TI = Inversion time; FA = Flip angle; px = Pixel; BW = Bandwidth; NEX = number of excitations								

- Brain imaging

Based on phantom results, brain scans were performed with 3D DESPOT1 using 2 FAs (Table 4). B_1 mapping was also performed with BS shift where a RF pulse with off-resonance frequency ω_{RF} = 8 kHz was placed into a spoiled GRE imaging sequence following excitation (Table 4). All data sets were acquired in coronal orientation relative to the rodent head.

Table 4. Sequence parameters used for mouse brain imaging.

Sequence	TR /ms	TE /ms	Acquisition matrix	FA /º	Voxel size /mm^3	Px BW /Hz/px	NEX
3D DESPOT1	14	5.9	192×192×60	3, 19	0.21×0.21×0.50	180	4
3D BS shift	60	13	128×128×16	15	0.39×0.39×1	379	2
TR = Repetition time; TE = Echo time; FA = Flip angle; px = Pixel; BW = Bandwidth; NEX = number of excitations							

MLNP MRI protocol

The following MRI protocol was employed to study the in vivo dynamics of injected MLNPs. After a scout scan, baseline mouse imaging consisting of brain and abdominal imaging, was performed. After injection of the nanoparticles in situ into the tail vein, without moving the mouse from the scanner, body imaging and brain imaging was repeated. $T1$-weighted maps on the brain were calculated with and without B_1 correction.

2.3.2. Rat study protocol

Certain advantages exist when rats instead of mice are used. These are higher SNR, easier animal setup in a clinical scanner and better tolerance to anesthesia and NP injection dose due to the increased size of rats compared to mice. The MRI protocol applied in this study was adapted based on the results obtained in the mouse study and the characteristics of the new animal. To study the accumulation of NPs in the brain and in other organs, in vivo experiments were performed in 12-30 weeks old female Wistar wild rats (n = 44).

Animal setup

Prior to MRI, rats were pre-sedated with isoflurane inhalation anesthesia. While scanning the first rat, the presence of an implanted animal identification chip (metallic object) within the volume to be imaged drastically distorted the local magnetic field because of its high magnetic susceptibility. This susceptibility artifact generated a total loss of signal in the particular region, surrounded by a strong distortion of the signal (Figure 4). Consequently, an operation removing this identification chip was included in the animal protocol prior to MR scanning.

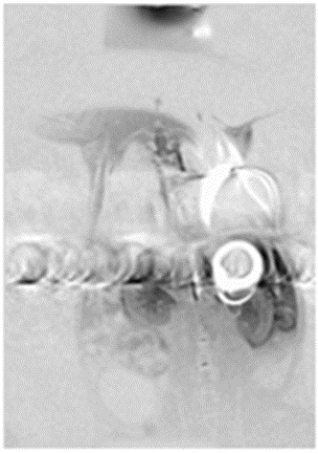

Figure 4. Susceptibility artifact generated by an implanted identification chip (white ring) in a rat.

Following sedation and extraction of the rat's chip identification, a catheter was placed into the vein in its right leg. This opening was used during the measurements to inject the nanoparticles as well as the anesthesia without having to remove the animal from the scanner (Figure 5B). Sedation during MR measurements was achieved with a mixture of ketamine and xylazine (2.3:1)

where 1.66 µL per gram body weight were injected intraperitoneally. To position the animal in the scanner, a thin piece of cardboard was used as an animal bed. The rat was fixed in supine position. A rectal probe (LUXTRON 790 Fluoroptic Thermometer, LumaSense Technologies, Santa Clara, CA, USA) continuously monitored the body temperature of the rats during scans (Figure 5D). Brain as well as abdominal imaging was carried out using the 2-element surface coil for signal reception (NORAS CPC Multipurpose coil 3 T) (Figure 5A). The presence of MLNPs in rats were separately measured in the abdomen and brain. During abdominal examinations, the rat's abdomen was positioned directly on the upper coil module of the 2-element CPC surface coil and the lower module on the rat's back. It was important to place the coil nearer to the legs as to the lungs to avoid breathing artifacts. For the examination of the brain, the upper coil was placed close to the animal’s mandible and the lower coil under the parietal bone (Figure 5B). In both configurations the coils were placed as close as possible, always allowing sufficient room for breathing. Two bottles containing a gel mixtures were also added on both sides of the lower half coil (Figure 5A) to facilitate the detection of the signal originating from the rat. Carefully placing the organ (abdomen or brain) at the isocenter of the magnet allowed easy automatic frequency and transmit adjustment for the rats. This methodological description was also published in a similar fashion in an original article (Martinez Vera et al. 2014).

- Animal setup optimization

An eight-channel phased-array wrist coil was also used in brain imaging to compare SNR with respect to the CPC surface coil. When the wrist coil was used, the rats were also placed in supine position on a thin cardboard holder and any bottle was added next to the coil (Figure 5C). To compare the SNR of these two coils, a total of 10 rats (5 rats per coil) were scanned using 3D DESPOT1-sequence.

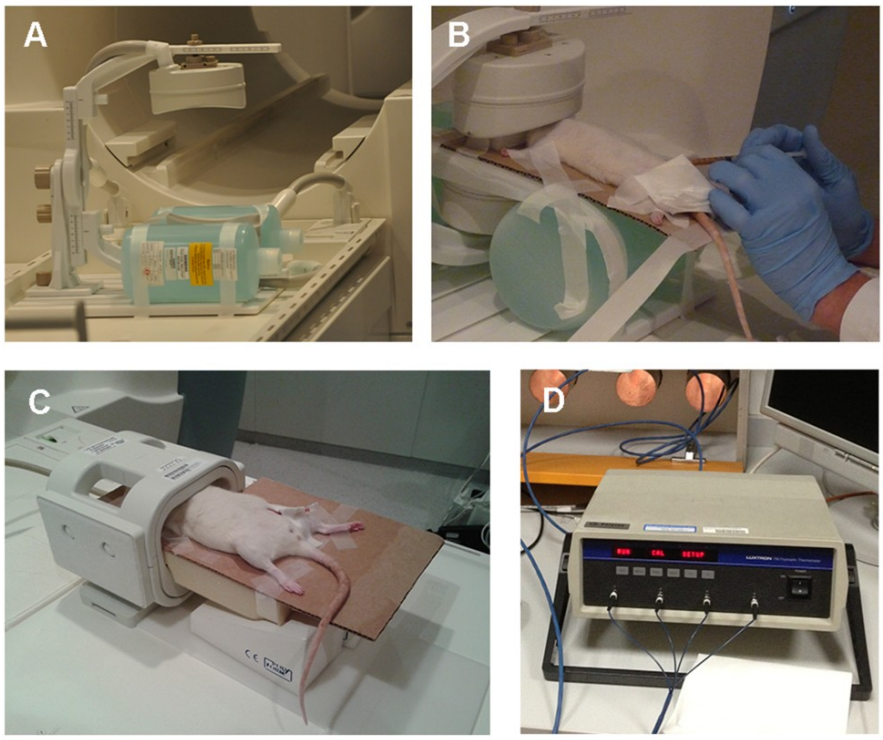

Figure 5. MR animal setup when tracking nanoparticles in the rat brain using a 2-element surface coil (A, B) or a wrist coil (C) for signal reception. (D) A fiber optic thermometer continuously monitored the body temperature of the rats during the scans.

MRI Sequences

Sequences used in the mouse study were adapted for rat imaging.

- Abdominal imaging

2D PSIR FSE-sequence (Table 5) was used in abdominal imaging with an ETL of 5 and total scan time of 3 min 20 s. As in mouse imaging, fat saturation and flow compensation were also switched on. Artifacts caused by motion due to breathing were also reduced using a spatial saturation slab on the region of the lungs. No physiological triggering was employed. All data sets were acquired in coronal orientation relative to the rodent head. This methodological description was also published in a similar fashion in an original article (Martinez Vera et al. 2014).

- Brain Imaging

Initially, brain scans were performed with 3D DESPOT1 using 2 FAs (Table 5). 3D acquisition with slice selective excitation was used in order to limit the backfolding

effect where the signal from the body folds into the brain. B_1 mapping was not performed. All data sets were acquired in coronal orientation relative to the rodent head. Total scan time was 14 min. Based on these initial rat brain imaging results and in order to obtain higher SNR, new sequence parameters were tested where the FAs were increased and two echo times were used (Table 5). Matrix acquisition and voxel size were kept the same. Total scan time was 23 min.

Table 5. Sequence parameters used for body (3D PSIR FSE) and brain (3D DESPOT1) rat imaging.

Sequence	TR /ms	TE /ms	TI /ms	Acquisition matrix	FA /º	Voxel size /mm^3	Px BW /Hz/px	NEX
2D PSIR FSE	5000	9.2	100	180×256×10	180	0.47×0.47×1.44	320	3
3D DESPOT1	14	5.9	-	192×192×30	3,19	0.21×0.21×1	180	16
3D DESPOT1	19	5.6, 11.14	-	192×192×30	4,22	0.21×0.21×1	200	14
TR = Repetition time; TE = Echo time; TI = Inversion time; FA = Flip angle; px = Pixel; BW = Bandwidth; NEX = number of excitations								

Generation and analysis of $T1$ maps of the rat brain

Before $T1$ map calculation and brain segmentation, image dataset coming from the baseline and two follow-up scans was spatially registered to the same space to remove scanner-induced image shifts. For that, they were linearly registered using FLIRT (FMRIB's Linear Image Registration Tool). The baseline magnitude image with the higher SNR was used as a reference image and each of the other images was 3D spatially registered to this one. As the brain images were from the same rat and in addition any rat displacement was made inside the scanner during the measurements, an intramodal brain image registration was performed with the transform type restricted to rigid body (degree of freedom = 6).

$T1$ maps were calculated for each echo. Maps were evaluated both individually and combined (average values). Segmentations of brain tissue from 3D T1 map images of the rat head were first manually performed using FSLview tool[4] to create a brain tissue mask. Automatic brain segmentation using FAST FSL tool was not possible. This tool is used to automatically extract human brain structures,

[4] www.fsl.fmrib.ox.ac.uk/fsl/fslview/, last accessed 14.04.2016

however due to the size of the rat brain, the SNR and the contrast between structures, this automatic tool did not recognize the brain and segmentation did not work. Manually segmentation was time-consuming so the software application was changed to ITK-SNAP[5] software which provided semi-automatic segmentation. This process consisted of an initial definition of a ROI in the image that contained the brain of the rat. All subsequent segmentation operations were applied to this ROI, rather than the whole image. The second step was the pre-segmentation stage where voxels with intensity within this specified range were mapped to positive speed values. After that, seeds were placed inside the brain. These seeds were spheres that expanded over the region of the positive portions and contracted in the negative regions. In the end, a contiguous object based on the seeds was created. The resulting 3D brain segmentation was not always perfect, so a final step was a manual correction using delineation. This new method made the segmentation process faster and robust brain segmentations were obtained (Figure 6).

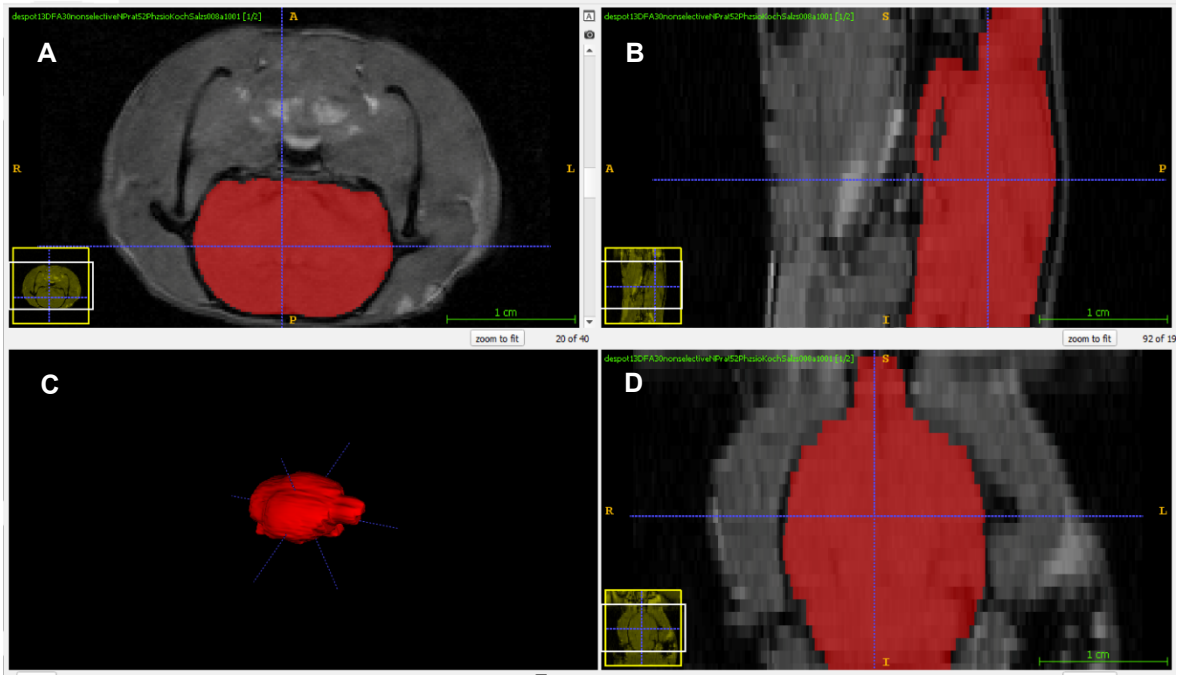

Figure 6. Segmentation of a rat brain (red) from a MR image using the semi-automatic segmentation software tool ITK-SNAP. Orthogonal slice views (axial (A), coronal (B) and sagittal section (D)) and the 3D volume of a segmented rat brain (C) are shown.

[5] www.itksnap.org, last accessed 14.04.2016

Following generation of $T1$ maps and using the brain masks, the $T1$ values in the brain were globally analyzed with a histogram technique using a home written script in Matlab (The MathWorks, Natick, MA, USA) with a bin width of 10 ms. A moving average filter of 15 ms span was used to smooth all of the data at once. Since brain volumes vary between rats, the histograms were normalized by dividing all histogram values by the total number of voxels. Histologically, the majority of brain tissue consists of gray matter, white matter, and cerebrospinal fluid space. Consequently, the $T1$ distribution in the entire brain was modeled by fitting a triple Gaussian function with a least-square technique. The three Gaussians represented gray matter (GM), white matter (WM), and cerebrospinal liquid (CSF). This methodological description was also published in a similar fashion in an original article (Martinez Vera et al. 2014).

Brain $T1$ imaging optimization

Some brain histograms had values that could not be explained by the triple Gaussian model (Figure 23 right). To understand the reason behind this finding, new phantom studies using a water bottle were performed. Data was acquired using 3D DESPOT1-sequence (Table 6; total scan time = 4 min and 67 s) and for signal reception, the 2-element surface coil (NORAS CPC Multipurpose coil 3T) was used. B_1 correction was also performed using the BS shift method (Table 6; total scan time = 2 min 22 s).

Table 6. Sequence parameters for optimization of rat brain imaging using a water bottle phantom.

Sequence	TR /ms	TE /ms	Acquisition matrix	FA /º	Voxel size /mm3	Px BW /Hz/px	NEX
3D DESPOT1	19	5.6, 11.4	192×192×16	4,22	0.47×0.47×2	200	14
3D BS shift	60	13	128×128×16	4,22	0.7×0.7×2	379	10
TR = Repetition time; TE = Echo time; FA = Flip angle; px = Pixel; BW = Bandwidth; NEX = number of excitations							

$T1$ maps were calculated and $T1$ values from each slice were evaluated using 2D ROIs. The mode of these $T1$ histograms served as a representative $T1$-weighted value per slice. Also, the $T1$ values from the whole volume were analyzed using a 3D ROI and $T1$-weighted images were evaluated using the mode of the $T1$ histogram of this ROI. Based on these results (Figure 24), new water phantom measurements were performed using the same 3D DESPOT1-sequence, however

this time a nonselective RF excitation pulse was enabled. This selection permitted higher FAs (FA = 6 º, 30 °) and consequently, the TR was raised to 30 ms and the number of averages was reduced to 6.

Based on the results obtained above (Figure 25), in vivo $T1$ mapping in the brain was estimated with a 3D mode acquisition and driven equilibrium single pulse observation of $T1$ (DESPOT1, FA = 6 ° and 30 °, TR = 30 ms; THK = 1 mm; FOV = 40 mm; matrix = 192 × 192 × 32). To increase the SNR of the $T1$ maps, the sequence was performed with two echoes ($TE1$ = 4.82 ms, $TE2$ = 9.96 ms). Total scan time was 26 min. Before averaging, $T1$ maps were calculated for both echoes separately. A nonselective excitation pulse was used in order to reduce flip angle errors by cause of slice profile effects. In addition, to prevent backfolding and to suppress residual signal from the rat body, a saturation slab was placed caudally. As this study focused on the longitudinal changes of $T1$ and therefore was based on serial $T1$ mapping, no attempts were made to correct for B_1 induced $T1$ errors. $T1$ maps were calculated and the $T1$ distribution in the entire brain was modeled by fitting a triple Gaussian function with a least-square technique. The three Gaussians represented GM, WM and CSF (Figure 26). This methodological description was also published in a similar fashion in an original article (Martinez Vera et al. 2014).

Generation and analysis of SWI maps of the rat brain

Magnitude (ρ) and phase (φ) images were used to generate susceptibility weighted maps. These images corresponded to the ones acquired with the longest TE and highest FA using the optimized DESPOT1-sequence for brain imaging. Initially, phase images were scaled between -pi and pi (unwrapping), and thereafter a complex number ($\rho e^{i\varphi}$) of the magnitude and phase image was generated. The complex input was then filtered using a 12 × 12 Hamming high pass filter. This filtered phase image was used as a mask and was multiplied 4 times (Eibofner et al. 2010) to the original magnitude image to obtain the SWI (Equation (1.29)). The code used for generation of susceptibility weighted maps was programmed by Christian Langkammer (Department of Neurology of the Medical University of Graz). Registration of baseline and post-follow images was not performed, meaning brain masks had to be created for each image. Brain SWI

maps were segmented and these values were globally assessed with a histogram technique as used in $T1$ analysis (bin width was 0.1 signal intensity (SI)). Since brain volumes vary between rats, the histograms were also normalized by dividing all histogram values by the total number of voxels. The mode of these histograms was used as the susceptibility SI value of the entire brain.

Determination of magnetite concentration in the brain

Magnetite concentration in the brain after MLNP injection was determined using Equation (2.1) where the susceptibility effect of the magnetite is considered (Equation (1.14)) together with the effect of the cooling of the brains during the scans which also had an influence on $R1$ brain measured values. Therefore:

$$R1 = R1^{o} + \frac{R1^{T}}{T} + r1C_{Fe_3O_4} \tag{2.1}$$

where $R1^{o}$ corresponds to the $R1$ value at the body temperature of the rat (T_0) and before administration of MLNPs, $R1^{T}$ is the rate change of $R1$ with temperature (temperature coefficient of $T1$ = 7.6 10^{-3} s/°C (Birkl et al. 2014)), T the temperature of the brain after MLNP injection and $r1$ is the effective relaxation rate of $R1$ as a function of magnetite concentration (magnetite coefficient of $R1$ = 5.7 s^{-1}/mM (Table 7)(Martinez Vera et al. 2014)). $C_{Fe_3O_4}$ is the concentration of magnetite in mM to be determined.

The temperature (T) of the rat brains after MLNP injection was calculated through phase mapping using proton resonance frequency (PRF) shift (Ishihara et al. 1995):

$$\Delta T = \frac{\varphi(T) - \varphi(T_o)}{\gamma \times \alpha \times B_o \times TE} \tag{2.2}$$

where $\varphi(T)$ is the phase image after MLNP injection, $\varphi(T_o)$ is the baseline phase image at the body temperature of the rat, γ is the gyromagnetic ratio, α is the PRF change (-0.01 ppm/°C), B_o is the external magnetic field strength and TE is the echo time. Phase difference was calculated using the four-quadrant arctangent function ($ATAN2$) (Equation (2.3)). This function took two input arguments, the numerator and the denominator of the arctangent function:

$$\varphi = \varphi(T) - \varphi(T_o) = \arctan\left(\frac{Im(Z1Z2^*)}{Re(Z1Z2^*)}\right) = ATAN2\left[Im(Z1Z2^*), Re(Z1Z2^*)\right] \quad (2.3)$$

Where $Z1 = \rho_1 e^{i\varphi(T)}$ and $Z2 = \rho_2 e^{i\varphi(T_0)}$ are two independent complex images.

$R1^o$ was determined using the rats treated only with saline solution. For each rat, the relaxation times before and after the injection and the temperature at these acquisitions were fitted with a linear regression model. The mean of the coefficients of these first degree polynomial fits was used to generate a general model to calculate $R1^o$. T_o was the mean of the measured rectal temperatures at the beginning of the experiments using the rats treated with saline solution. The brain temperature T was calculated using phase mapping (Equation (2.2) and Equation (2.3)).

MLNP MRI protocol

Two rats served to explore the accumulation of MLNPs in the body following intravenous injection of 400 µL (800 µg) MLNPs through the femoral vein. The measurements were performed before NP administration and (9, 18, 27, 36) minutes and 1 week after the injection.

The detection of MLNPs in the brain was performed using 38 rats and the concentration of magnetite in the brain was determined using 10 rats out of the 38. Following $T1$ baseline mapping, MLNPs were injected intravenously into the femoral vein without removing the rat from the coil through a catheter that had been previously prepared. A solution containing MLNPs (4.8 mg) suspended in physiological buffer (1 mL) was administered at 3.2 µL per gram body weight. Saline solution at equal volume served as control in 10 out of the 38 rats. After injection, $T1$ mapping was subsequently repeated two times. In the group of 28 rats with MLNP administration, 11 rats received PEG coated MLNPs and in 2 rats, 400 µL (800 µg) MLNPs were administered by intraventricular injection to achieve a higher MLNP concentration in the brain. At the end of this thesis, smaller size MLNPs were synthesized (diameter of MLNP = 110 nm) and these were used in a group of 10 rats for MLNP SWI analysis and for determination of MLNP concentration in the brain, 5 rats out of the 10 received PEG coated MLNPS.

$T1$ histograms of the brains were represented with the three components WM, GM and CSF. The peak positions of these three Gaussians curves were used as the global $T1$ value for these structures which facilitated robust analysis of MLNP induced relaxivity changes. This methodological description was also published in a similar fashion in an original article (Martinez Vera et al. 2014). SWI analysis was performed by comparing the positions of the histogram mode from the baseline brain histogram and the brain histograms of the two follow-up scans. Based on $T1$ mapping results, the magnetite concentration in the brain was calculated using only the $T1$ values of the GM for the baseline, first and second follow-up scans. Rather than an accumulation in specific structures, the rationale behind this approach was a diffusion model where a global and diffuse distribution of MLNPs in the brain was expected.

2.4. MRI validation method

Histological studies using fluorescence imaging (the protocol as well as the techniques used are detailed in the Appendix B) served to validate the MR studies when tracking the MLNPs in vivo using rats. The mean fluorescence signal in the investigated brain sections of the corpus callosum (CC) and hippocampus (HC) in the green and red channels were linearly correlated with the $T1$ changes in the GM, WM and CSF, with the susceptibility changes in the entire brain and with the magnetite concentration in GM, all for the first and second follow-up scans. This methodological description was also published in an original article (Martinez Vera et al. 2014).

2.5. Statistical analysis

Linear correlation analyses (Pearson's r) were performed to study the relationship between the MR examinations (MLNP induced $T1$ changes, susceptibility changes, magnetite concentration measurements) and the histological analyses (relative levels of fluorescence). A paired t-test was used for comparison of ex vivo signal as well as to determine significant $T1$ and susceptibility changes following MLNP injection, i.e. to verify whether minimal uptake of MLNPs can be probed by quantitative MRI. A p-value of < 0.05 was considered as statistically significant. Before the t-test analysis, a test for normality was performed using the Shapiro-Wilk test for normality. The test rejects the hypothesis of normality when the p-

value is less than or equal to 0.05. This methodological description was also published in a similar fashion in an original article (Martinez Vera et al. 2014).

3| Results

3.1. Nanoparticle preparation

See results in Appendix A. These findings were published in an original article (Martinez Vera et al. 2014).

3.2. MLNP relaxivity assessment

3.2.1. Relaxivity analysis

Different relaxivity responses were obtained for each model at each concentration. Six magnetite concentrations were found to be most suitable for sample preparation when a high effect of magnetite was present: (0.02, 0.03, 0.06, 0.12, 0.25 and 0.49) mM. Relaxivity results from phantom measurements with different MLNPs are summarized in Figure 7 and Figure 8. In line with theoretical considerations, the longitudinal relaxation rate constant $R1\ (=1/T1)$ and the effective transversal relaxation rate constant $R2^*(=1/T2^*)$ were found to correlate linearly with magnetite concentration. The size of the MLNPs showed some effect on the relaxivity; however, the slope of the regression line was mainly determined by the size of the magnetite.

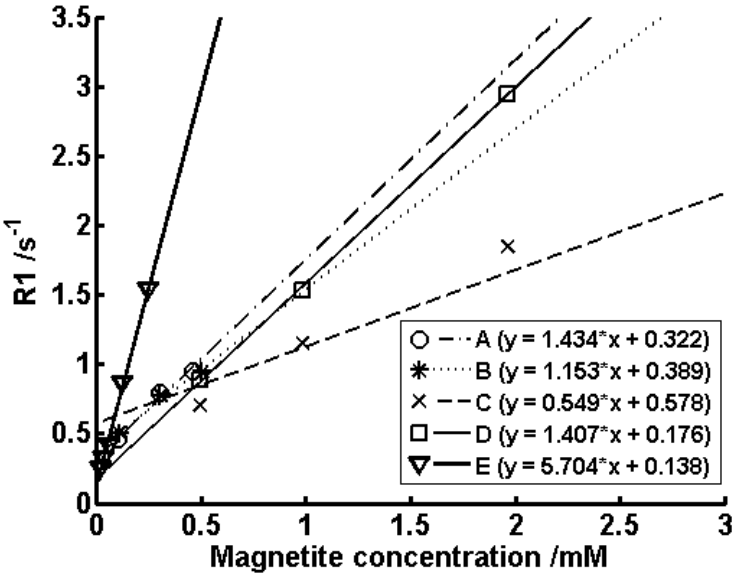

Figure 7. Linear regressions between the longitudinal relaxation rate constant $R1\ (=1/T1)$ and magnetite concentration of the different MLNPs defined in Table 7. Reproduced from (Martinez Vera et al. 2014), copyright (2014) under the terms of the Creative Commons Attribution License (CC BY 4.0), https://creativecommons.org/licenses/by/4.0/.

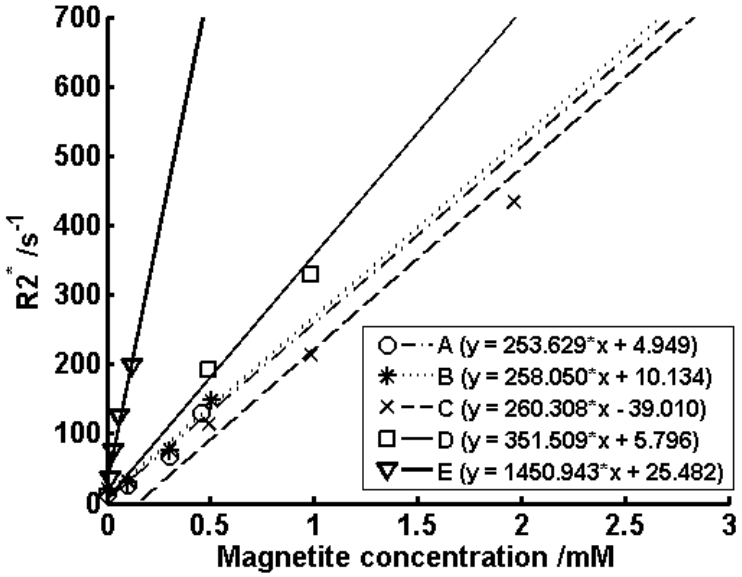

Figure 8. Linear regressions between the effective transversal relaxation rate constant $R2^*(=1/T2^*)$ and magnetite concentration of the different MLNPs defined in Table 7.

The strongest $\mathrm{R1}$ and $R2$* effect was found for the MLNPs with a mean diameter of approx. 200 nm and an 8 nm magnetite loading of 90.90 µg per mg of MLNP. This kind of MLNPs, with a higher relaxivity effect, was selected for the in vivo measurements. $R2$* mapping was not chosen for in vivo studies due to the limited readout bandwidth for the high MLNP relaxivity response (Table 7). These findings were also published in a similar fashion in an original article (Martinez Vera et al. 2014).

Table 7. Relaxivity of the different magnetically labeled nanoparticle (MLNP) formulations. Reproduced from (Martinez Vera et al. 2014), copyright (2014) under the terms of the Creative Commons Attribution License (CC BY 4.0), https://creativecommons.org/licenses/by/4.0/.

Letter Series	Diameter of MLNP /nm	Diameter of magnetite NP /nm	µg magnetite per mg MLNP	Polydispersity index (PDI)	$r1 \pm$ standard deviation /mM^{-1}s^{-1}
A	462.8	20	47.62	0.17	1.43 ± 0.11
B	551.7	20	47.62	0.03	1.15 ± 0.08
C	201.6	20	90.9	0.04	0.54 ± 0.06
D	318.1	20	90.9	0.12	1.40 ± 0.33
E	200.8	8	90.9	0.09	5.70 ± 0.23

3.2.2. DESPOT1 measurements

The choice of flip angles in spoiled GRE-sequences as DESPOT1-sequence was critical for determining both SI as well as image contrast. When analyzing nanoparticle series A, SI clearly depended on magnetite concentration and on the flip angle used (Figure 9). Using the same scan parameters, the SI decreased with higher magnetite concentration. Furthermore, within each concentration, MR signal was maximized at the Ernst angle (Deoni et al. 2004) (Figure 9 red marks). The maximum MR signal was reached at 20 ° in samples containing higher magnetite concentration (0.30 mM and 0.46 mM), and at 15 ° in samples with less concentration (0 mM and 0.10 mM).

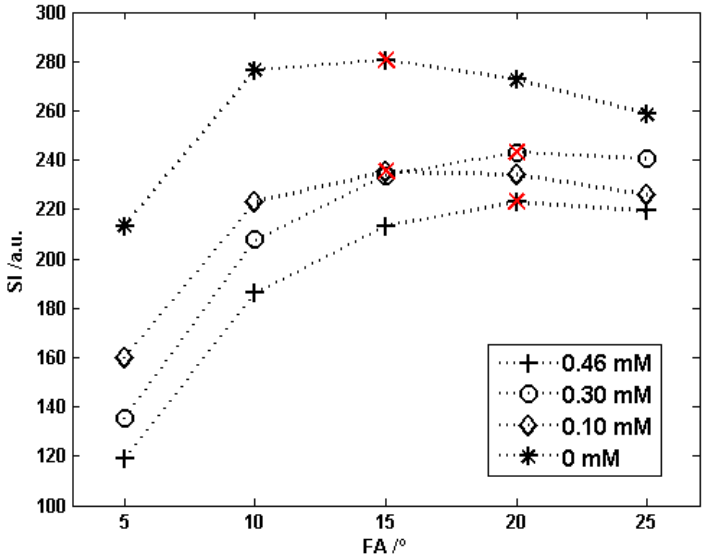

Figure 9. Flip angle (FA) influence on signal intensity (SI) depending on the sample magnetite concentration (0 mM, 0.10 mM, 0.30 mM and 0.46 mM) of nanoparticle series A using 2D DESPOT1-sequence. There was a shift from 15 ° to 20 ° (red marks) in the Ernst angle when concentration of magnetite in the samples increased.

$T1$-weighted maps were calculated for each series of MLNPs. $T1$ values decreased with magnetite concentration (Figure 10). The DESPOT1-sequence was found to systematically underestimate the $T1$ values (Figure 10B) compared to those obtained using IR-sequence (Figure 10A).

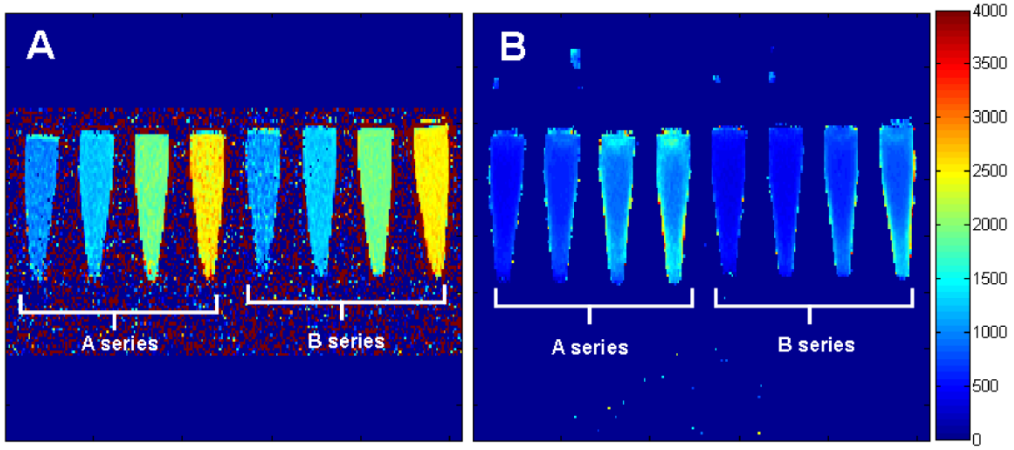

Figure 10. $T1$ mapping using 2D IR-sequence (A) and 2D DESPOT1 (B) with 5 FAs from magnetite-loaded nanoparticle series A and B (from right to left: 0 mM, 0.10 mM, 0.30 mM and 0.46 mM). $T1$ values obtained with 2D DESPOT1 were lower than the reference values obtained with IR. Colorbar represents $T1$values.

DESPOT1 optimization

- Correction of B_1 inhomogeneities from the transmitter coil

$T1$ values were uniformly distributed throughout the phantom as seen in Figure 11 when B_1 inhomogeneities were corrected using DAM (Figure 11B) and BS shift (Figure 11C) sequences. However, reference $T1$ values obtained with 2D IR-sequence (Figure 11D) were still higher than those obtained with 2D DESPOT1.

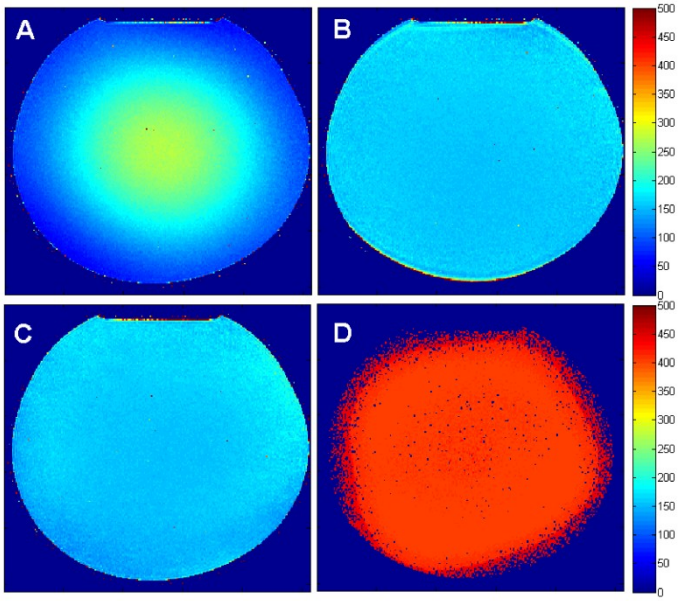

Figure 11. $T1$ maps obtained with 2D DESPOT1-sequence without B_1 correction (A) and with B_1 correction DAM (B) and Bloch-Siegert shift (C) methods. $T1$ values were uniform through the phantom when B_1 inhomogeneities were corrected. $T1$ values were lower as the ones obtained with 2D IR (D). Colorbar indicates the $T1$ values coming from the phantom.

BS shift was selected as the B_1 correction method in MLNP sample measurements due to its total reduced acquisition time (2.75 min) in comparison with DAM acquisition time (5.52 min). However, phase correction factor (k_{BS}) maps showed that the signal coming from high magnetite concentration samples (Figure 12) and also from nanoparticle series E, all of which had a high relaxivity response, was null.

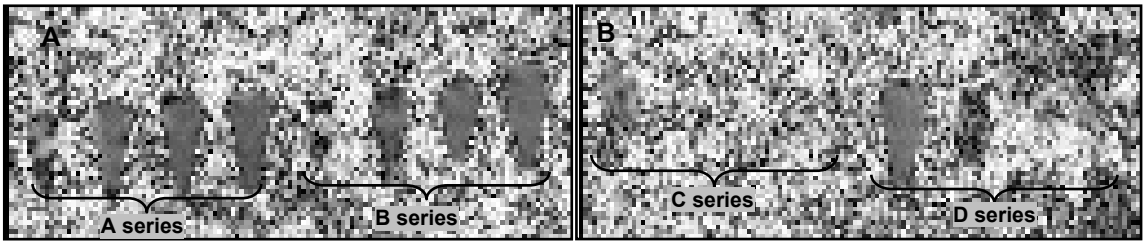

Figure 12. Phase correction factor (k_{BS}) maps using Bloch-Siegert shift sequence from nanoparticle series A, B (A), C, D (B) using different magnetite concentrations (nanoparticle series A and B from right to left: (0, 0.10, 0.30 and 0.46) mM; nanoparticle series C and D from left to right 0.49 mM, 0.98 mM, 1.96 mM and 3.93 mM). With a high concentration of magnetite, the signal coming from k_{BS} mapping was null.

Analysis of the influence of the different FAs used on $T1$ mapping showed that the slope from the different linear fittings was similar (values were between 0.87 and 0.88) when plotting $S_{SPGR}/\sin(\alpha_T)$ versus $S_{SPGR}/\tan(\alpha_T)$ (Table 8). However, $T1$ values calculated from these slope values were very different (Figure 13B). This was due to the localization of these slopes which were inside the range where the natural logarithm changes the most (Figure 13A).

Table 8. Linear fitting parameters when plotting $S_{SPGR}/\sin(\alpha_T)$ vs. $S_{SPGR}/\tan(\alpha_T)$ are presented using five or two transmitted angles (α_T) in 2D DESPOT1-sequence.

Flip angles α_T /degrees	$f(x) = slope \times x + intercept$; coefficients with 95 % confidence bounds	
	slope	intercept
5,10,15,20,25	0.8797 (0.8758, 0.8835)	504.1 (492.4, 515.9)
5,10	0.8754	521.2
5,15	0.8808	499.5
5,20	0.8808	499.3
5,25	0.8786	508.0

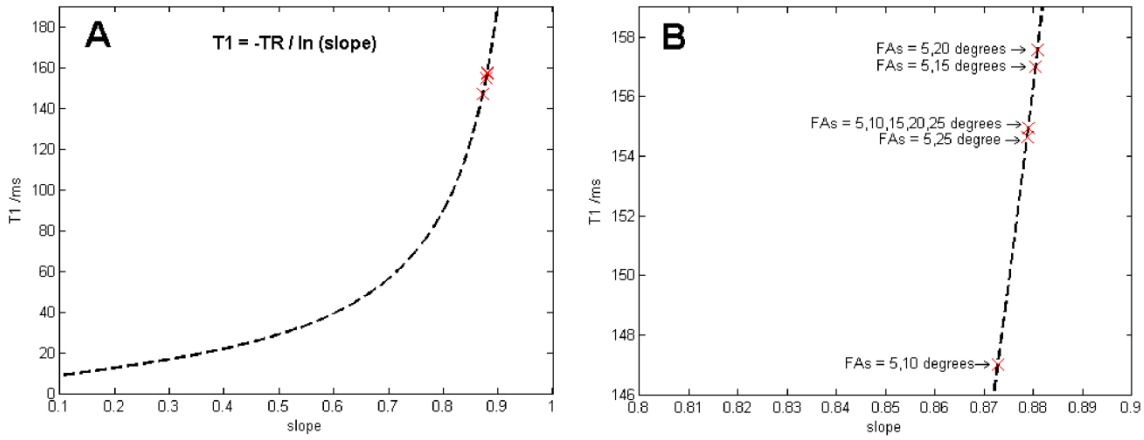

Figure 13. $T1$ values (red crosses) obtained from different calculations using the signal obtained from five or two flip angles in 2D DESPOT1-sequences. (A) $T1$ values are located where natural logarithm changes the most. (B) Zoom where the measurements are located. Although slope values were similar, $T1$ values were quite different.

Based on these results, the FAs selected to be used in the DESPOT1 acquisitions were 3 and 19 degrees.

Finally, 3D DESPOT1 using 2 FAs reduced the scan time and reached $T1$ reference values obtained with 2D IR-sequence (Figure 14).

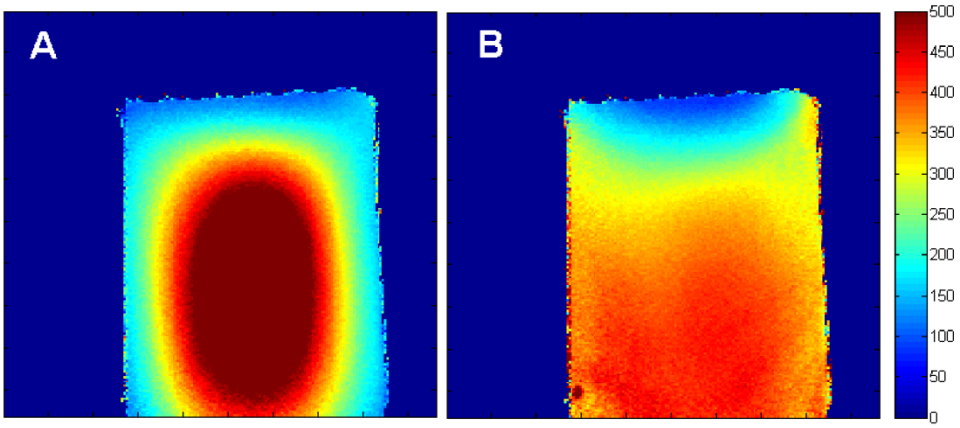

Figure 14. $T1$ maps (sagittal view) obtained with 3D DESPOT1 without (A) and with (B) BS shift method using a series of 2 FAs (3 º and 19 º). Homogeneity improvement was reached when corrected angles were used. The resulting DESPOT1 3D values were in agreement with IR reference $T1$ values (Figure 10C). Colorbar indicates $T1$ values coming from the phantom.

Final protocol (sequences and their optimized parameters) for MLNP relaxometry assessment is summarized Table 9. These findings were also published in a similar fashion in an original article (Martinez Vera et al. 2014).

Table 9. Final MRI protocol used in phantoms to evaluate the relaxometry effect of different magnetite MLNP concentrations.

Relaxometry	Sequence	TR /ms	TI /ms	TE /ms	FA /º	Voxel size /mm	Total TA /min
	Localizer	8.6	-	4	20	0.9×0.8×5	-
$T1$	2D IR	5000	50,100,200, 400,800, 1600,3200	9.2	180	0.47×0.47×2	14.31
$T1$	3D DESPOT1	10	-	4.22	3,19	0.63×0.63×1	4.51
$T2^*$	2D Multi-echo GRE	300	-	4.92, 24.6	30	0.47×0.47×3	4.71
TR = Repetition time; TI = Inversion time; TE = Echo time; FA = Flip angle; TA = Acquisition time							

3.3. In vivo MR MLNP tracking

3.3.1. Results in mouse studies

RF coils and animal setup

The CPC coil provided high SNR and high homogeneity throughout the image of the body with a large FOV (Figure 15). However, the head microcoil exhibited a strong signal dependency with distance r from the coil center ($\propto 1/r^2$). This signal dependency caused signal variation across the image as shown in Figure 16A, where the top of the head, closer to the coil, had higher signal than the bottom part of the brain. This is the reason why it was important to place the coils as close as possible to mouse head and body. The animal setup implemented in this study allowed the combination of the two coils, thus brain and body imaging from the same animal was possible within the same experiment. The temperature of the animal was kept constant and the mouse was under anesthesia for the entire scan time.

MRI sequences

An aspect to be considered at the beginning of the measurements was the initial shimming to maintain B_0 homogenous inside of the mouse's FOV. For that, it was important that the initial selected volume FOV was placed only in the mouse's FOV. The bottles had to be outside of this FOV due to their high signal contribution in the initial shimming. A prior manual shim adjustment was also necessary to

compensate for strong B_0 inhomogeneity caused by the mouse's anatomy. All coils were activated when the localizer sequence was used.

- Abdominal imaging

Although high SNR was obtained using the 3D FLASH sequence, fat suppression and flow compensation were not enough to eliminate motion artifacts when scanning the body of the mouse (Figure 15A). PSIR TSE with a saturation slab on the lungs reduced motion artifacts, as can be seen in Figure 15D, in comparison with the PSIR TSE and any form of correction (Figure 15B) or with only fat suppression and flow compensation (Figure 15C). A saturation slab in the region of the lungs generated a very low signal and appeared as background signal in the MR images. Because of 2D imaging, physiological triggering and gating was no longer required. Among the TIs used to obtain the body images, TI = 100 ms was selected because it provided enhanced contrast between body structures and background air was rendered a mid-shade of gray.

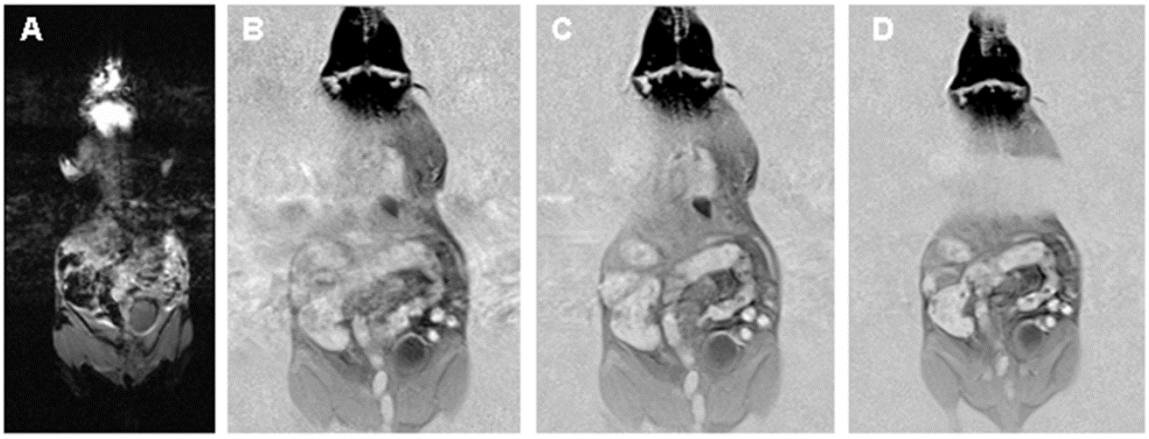

Figure 15. Optimization of body imaging in mice. (A) 3D FLASH-sequence was first implemented but it was changed to phase sensitive-IR fast spin echo sequence (B) due to motion artifacts in the images. Flow compensation, fat suppression (C) and also a saturation slab on the lungs (D) improved image quality and removed motion artifacts.

- Brain imaging

Using the 3D DESPOT1-sequence, high SNR in the brain was achieved (Figure 16). When using a FA of 19 degrees, it was possible to achieve time of flight effect. This phenomenon is known as flow-related enhancement (Axel 1984) where the inflow of spins results in increased signal. Due to this phenomenon blood produced bright signal and vessels could be detected (Figure 16B).

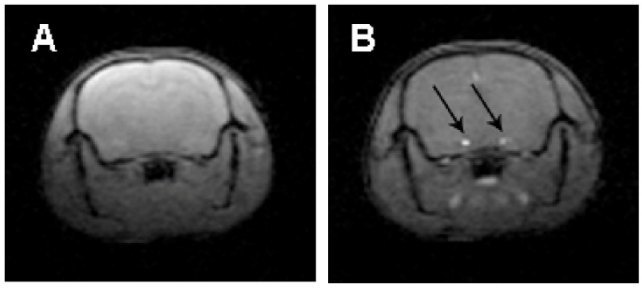

Figure 16. Same coronal brain slices obtained with 3D DESPOT1 using 3 º (A) and 19 º (B). Vessels (arrows) were detected when FA = 19 º.

A summary with the final sequences used in the mouse MRI protocol can be seen in Table 10.

Table 10. Final sequences in body and brain mouse imaging.

Sequence	TR /ms	TI / TE /ms / ms	ETL	FA /º	Voxel size /mm	Image matrix	Px BW /Hz/px	NEX	TA /min
Localizer	8.6	-/4	-	20	0.9×0.8×5	512×512			
Body 2D PSIR FSE	5000	100 / 9.2	5	180	0.39×0.39 ×2.25	180×256× 10	326	3	3.58
Brain 3D DESPOT1	14	-/5.9	1	3, 19	0.21×0.21 ×0.5	192×192× 60	221	4	7.14
TR = Repetition time; TI = Inversion time; TE = Echo time; ETL = Echo train length; FA = Flip angle; TA = Acquisition time; Px BW = Pixel bandwidth; NEX = Number of averages									

Brain $T1$-mapping

Brain $T1$ maps were calculated with and without B_1 correction (Figure 17). When B_1 correction using BS shift method was applied in $T1$ calculations, the quality of the images degenerated. Due to the inferior resolution and high susceptibility artifacts, the phase correction factor (k_{BS}) maps (Figure 17C) added its own noise when calculating $T1$ maps (Figure 17B). Because the detection of $T1$ changes in the brain due to the presence of magnetite does not need absolute values, the correction of B_1 inhomogeneities was not included in the animal protocol.

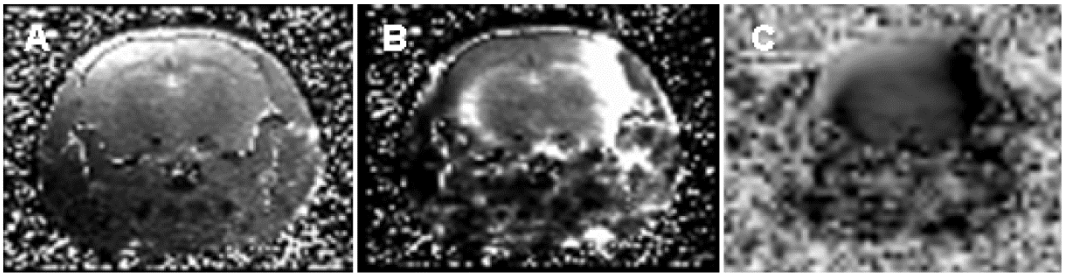

Figure 17. Same coronal brain $T1$-weighted slices obtained with 3D DESPOT1 without (A) and with (B) B_1 correction using Bloch-Siegert shift. (C) Due to the inferior resolution and high susceptibility artifacts, phase correction factor (k_{BS}) maps added its own noise when calculating $T1$ maps.

MLNP MRI protocol

The duration of the final protocol, excluding the time to inject the MLNPs, was 25 minutes. Nanoparticle injection in situ through the mouse's tail vein took more than ten minutes. The blue tail vein was difficult to find because the tail was no longer warm and the vein was not any longer dilated. Furthermore, this task was also difficult due to the lack of sufficient lighting inside the scanner room. It was also very important that the mouse kept the same position during all the scans so it was not possible to make any changes to the mouse position to improve tail vein visibility. To facilitate this task, a heat pad was added under the tail of the mouse. However, the best solution was to inject the nanoparticles outside the scanner room. Nanoparticles were visualized neither in the abdomen (Figure 18) nor in the brain.

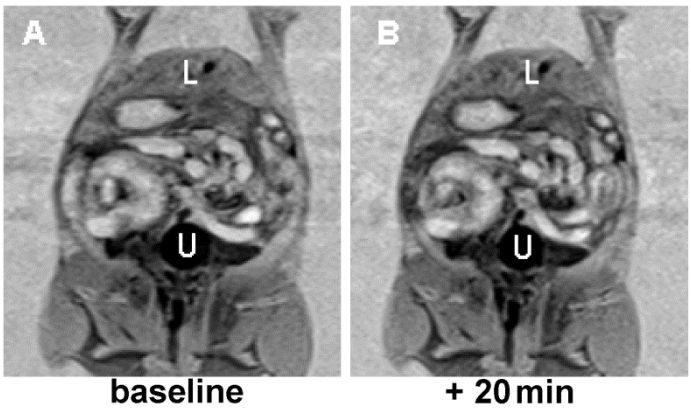

Figure 18. Transversal abdominal slices obtained with PSIR FSE-sequence before MLNP injection (A) and 20 minutes after the injection through the tail vein (B). Any magnetite induced change was observed neither in liver (L) nor in the urinary bladder (U).

3.3.2. Results in rat studies

Next, results obtained in abdominal and brain imaging in rats. The validation of the MR results using fluorescence imaging is also presented.

Abdominal imaging

The PSIR FSE-sequence provided sufficient resolution and contrast to assess MLNP induced signal intensity changes in the body of the rat. Most pronounced changes presented as an increase in signal intensity were observed in the liver and spleen. These changes were apparent at the first imaging time point 9 minutes after MLNP injection and thereafter almost no further changes over the observational period of 36 minutes were observed (Figure 19). These findings were also published in a similar fashion in an original article (Martinez Vera et al. 2014). One week after injection, signal intensity decreased however it did not reach baseline values, indicating the ongoing presence of MLNPs in these organs (Figure 20). Subsequent to MRI, these regions also presented marked changes in the fluorescence signal (Figure B-1). These findings were also published in a similar fashion in an original article (Martinez Vera et al. 2014).

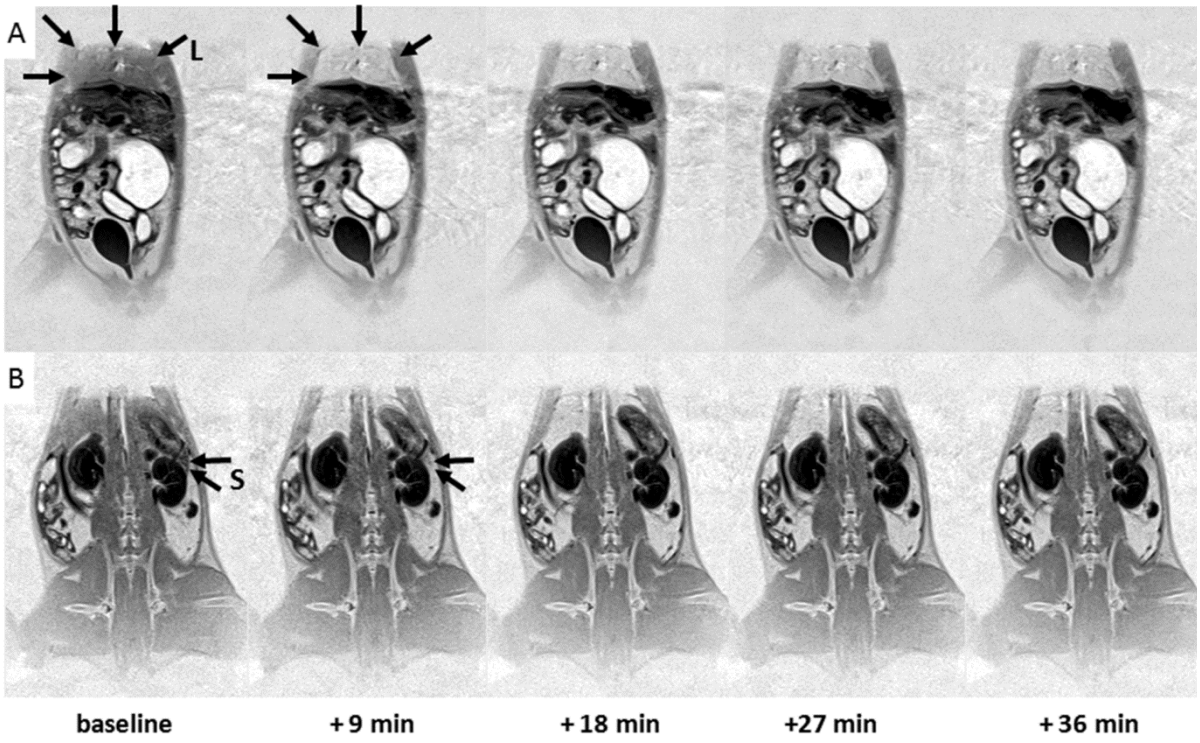

Figure 19. Signal increase (arrows) due to the uptake of MNLPs in the rat body was observed in the coronal MRI slices of the liver L (row A) and the spleen S (row B). Reproduced from (Martinez Vera et al. 2014), copyright (2014) under the terms of the Creative Commons Attribution License (CC BY 4.0), https://creativecommons.org/licenses/by/4.0/.

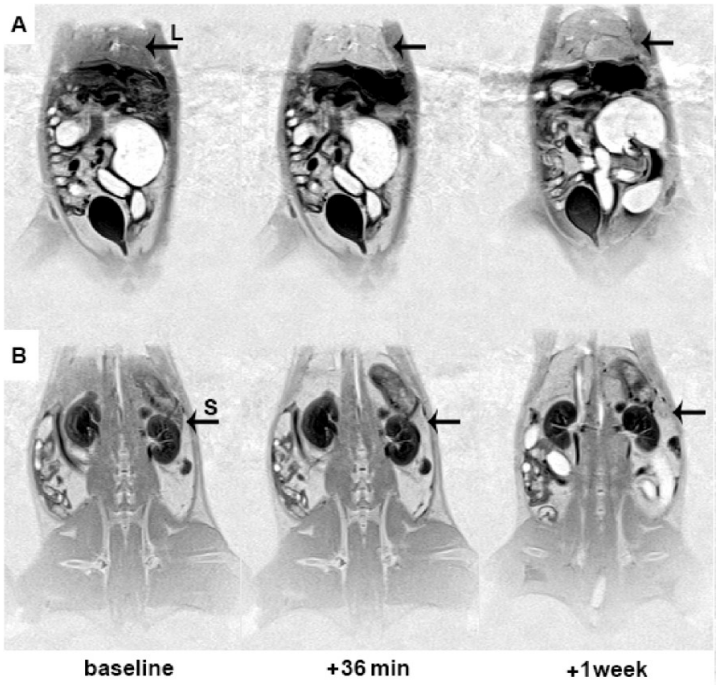

Figure 20. One week after injection, signal decrease (arrows) was observed in the coronal MRI slices of liver L (row A) and the spleen S (row B), however these signal intensities were still higher than the signals before injection (baseline). Angulation of the right row is not identical due to repositioning.

Brain imaging

- Animal setup

SNR was influenced by the animal bed which consisted of a thin piece of cardboard. The thinner the board, shorter the distance between the brain and the coil leading to be able to obtain higher SNR in brain imaging (Figure 21A, cardboard thickness = 4 mm; Figure 21B, cardboard thickness = 2 mm).

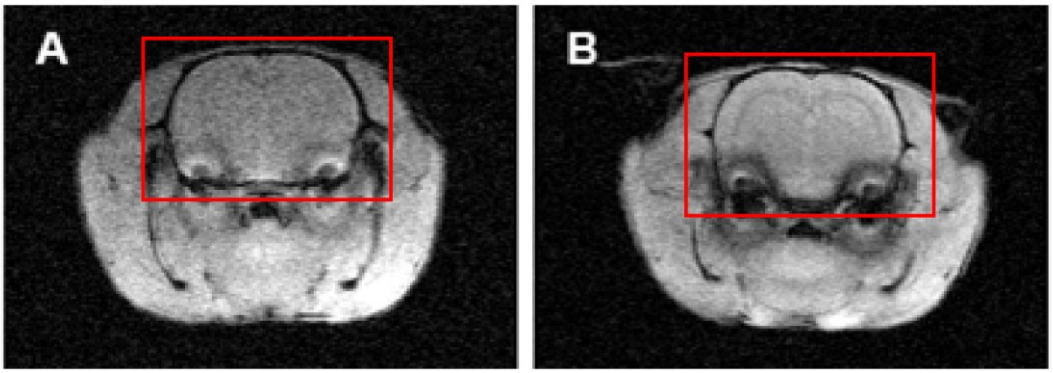

Figure 21. Effect of the animal bed in brain imaging. Coronal MRI slices of two rat brains (in squares) using the same 3D DESPOT1-sequence parameters. Higher SNR was obtained when the animal holder (A, thickness = 4 mm) was replaced by a thinner one (B, thickness = 2 mm). Angulation of the slices is not identical due to repositioning.

Animal setup optimization

Figure 22 illustrates the results obtained when CPC surface coil (A, C) and the wrist coil (B, D) were compared in rat brain imaging using the optimized 3D DESPOT1-sequence with FA = 6 ° (left histograms) and 30 ° (right histograms). The histograms show the SI coming from the brains of 10 rats, 5 rats using the surface coil (dashed line) and 5 rats using the wrist coil (line). Transversal brain images in the figure correspond to two different rats, each one imaged with a different coil. Slice positions are identical.

Both coils provided images with a large field of view. The two CPC modules, one module above and the other below the rat head, delivered SNR which decreased roughly in the direction of the dorsoventral (Figure 22A, C). For each coil, brain SI histogram curves obtained with FA = 30 ° were more dispersed than the curves obtained using FA = 6 º. The mode (signal intensity of the highest frequency) and

the full-width at half-maximum (FWHM) of each histogram were calculated and the mean of these parameters was analyzed (Table 11).

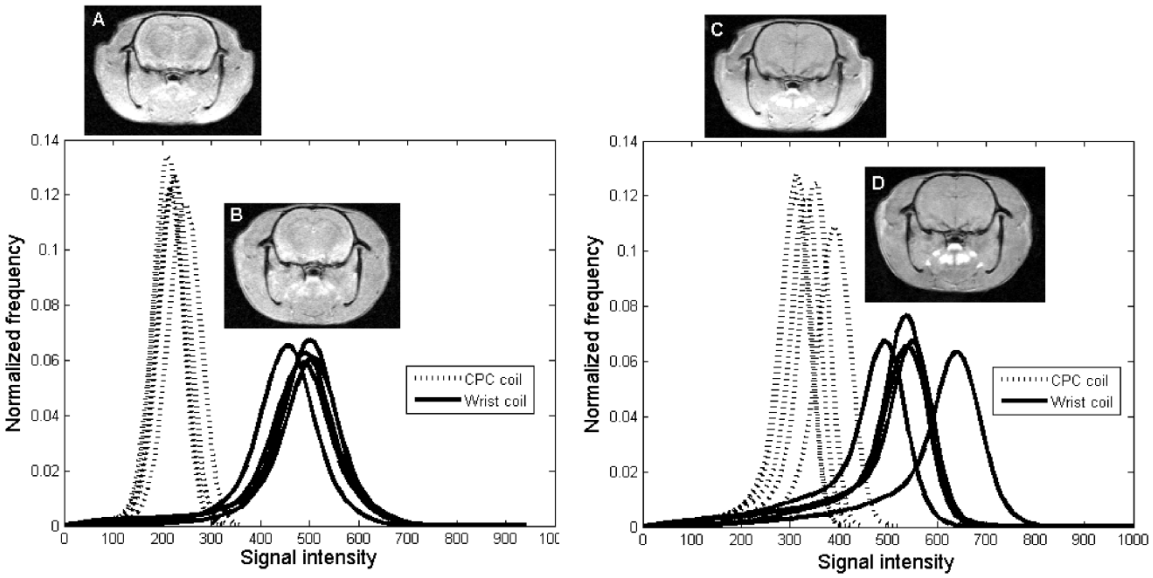

Figure 22. SNR comparison between a CPC (A, C) and a wrist coil (B, D) using the same 3D DESPOT1-sequence. From each coil, two rat brains (coronal view images) are shown with FA = 6 º (left brain histograms) and FA = 30 º (right brain histograms). Angulation of A and C slices is not identical to B and D slices due to repositioning.

Table 11. SNR analysis using a CPC and a wrist coil. Mode and FWHM mean values of rat brain SI histograms using 3D DESPOT1-sequence.

Coil	Mean mode SI / SEM		Mean FWHM / SEM	
	FA = 6 º	FA = 30 º	FA = 6 º	FA = 30 º
CPC	226 / 7	341.6 / 14.3	73.73 / 1.78	70.80 / 2.01
Wrist	490 / 7	552.4 / 24.9	128.13 / 1.54	107.65 / 2.89
SEM = Standard error of the mean; FA = Flip angle; FWHM = Full width half maximum				

SNR coming from the brain using the CPC coil was almost half (46 %) of the SNR obtained with the wrist coil. This difference was larger (62 %) when the FA used was 30 º. Inhomogeneity was measured by the mean of the FWHM. For the wrist coil, inhomogeneities were higher than those from the surface coil for 6 º (57 %) and 30 º (66 %). Furthermore, when the wrist coil was used, the combination of water and gel bottles was not needed. Since an improvement in the initial shimming was achieved as well as an optimized animal set up.

- Brain $T1$ maps

Mask images of the brain were used to extract $T1$ brain values. Using a whole brain histogram technique, a frequency distribution of $T1$ values was obtained. From each TE, brain $T1$ maps were calculated and the histogram of the mean values of these $T1$ maps was analyzed (red curve in Figure 23 left).

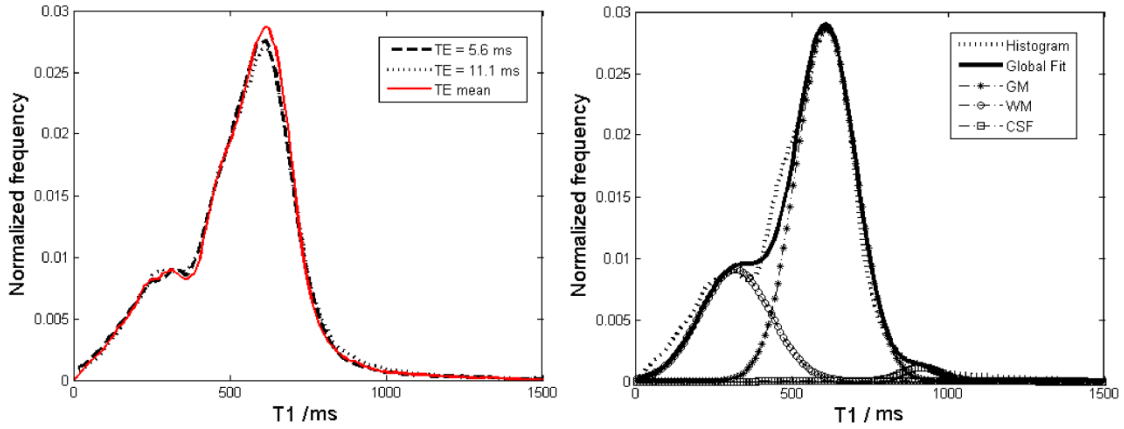

Figure 23. $T1$ histograms of a rat brain. Three histograms (left) were obtained with two echo times ($TE1$ = 5.6 ms (dashed line); $TE2$ = 11.4 ms (pointed line)) and the average of these two TEs (red line). Triple Gaussian fitting (right) allowed for separation of white matter (circles), gray matter (diamonds) and cerebrospinal fluid (squares).

$T1$ histograms were first fitted using a double Gaussian fitting in order to segment WM and GM regions of the brain. However, there were high $T1$ values (> 1000 ms) that were not included in this model. Partial volume voxels became important, since a large proportion of the grey matter lies in voxels that contain CSF, so whole-brain histograms had a small contribution of CSF and this component had to be included in the Gaussian model. The Triple Gaussian fit (Figure 23 right) allowed the representation of the whole brain into WM, GM and CSF Gaussian curves. On the other hand, histograms also presented low $T1$ values (< 100 ms) which were not physiological and could not be explained by the triple Gaussian model. This indicated that the brain imaging sequence which had been applied led to some errors. To resolve them, new phantom experiments were performed.

Brain imaging optimization

The results obtained in water phantom experiments were used to evaluate the 3D brain imaging sequence and to correct $T1$ for non-physiological values. The effect of B_1 corrections was also examined.

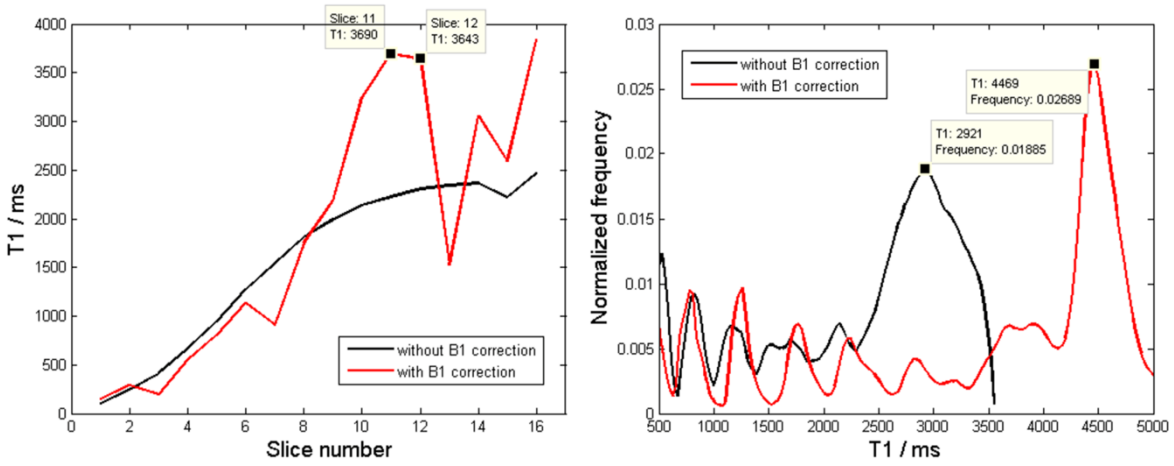

Figure 24. $T1$ values of a water phantom with (red line) and without (black lines) B_1 correction using 2D ROIs per slice (left) and using a 3D ROI (right). Low $T1$ values corresponded to slice profile artifacts due to the 3D acquisition mode with RF selective slice excitation.

$T1$ values of the 3D volume water phantom were calculated with (Figure 24 red line) and without (Figure 24 black line) B_1 correction. $T1$ histograms of each slice of the volume were calculated from ROIs using 2D masks (Figure 24 left). Non-corrected $T1$ values were not constant throughout the slices and always lower than water $T1$ values (~ 3600 ms at 3 T). On the other hand, corrected values were also not constant throughout all slices, however they reached the correct water $T1$ values at central slices (slice numbers = 11 and 12). A 3D mask was also used to select a ROI of the whole volume (Figure 24 right). The highest peaks observed in the corrected and non-corrected histograms were lower (Figure 24 black line) and higher (Figure 24 red line) than the correct $T1$ values of water. Furthermore, additional low $T1$ values were also present in the histograms. The slice-selection pulse of selective 3D imaging produced slice profile artifacts, as observed by the alteration of water relaxation times compared to adjacent slices. Non-selective 3D imaging uses excitation pulses without slice profiles and they are used when no spatial selection is required. This non-selective 3D acquisition was then tested in these water phantom experiments (Figure 25). As before, the mode of the $T1$ value histograms of the 2D ROIs of each slice was evaluated (Figure 25

left) and the $T1$ histograms of the whole volume were analyzed using a 3D ROI (Figure 25 right). Here, the effect of B_1 inhomogeneities was not examined. These new sequence parameters permitted obtainment of images with higher SNR and a reduced acquisition time. Furthermore, as seen in Figure 25 left, the $T1$ mode values were constant throughout all slices (3631 ms $\pm$ 32 ms). This value also roughly corresponded the histogram mode (3685 ms) when the whole volume was analyzed. Furthermore, the low $T1$ values previously observed were no longer present. The excitation pulse length in non-selective 3D imaging can be very short, so shorter TEs (TEs = 4.82 ms, 9.96 ms) could be achieved and subsequently $T1$-weighting increased. Also, higher FAs (6 º, 30 º) were used which further maximized the $T1$ contribution. Thus, correct water $T1$ values were obtained and slice profile artifacts were corrected using these new sequence parameters.

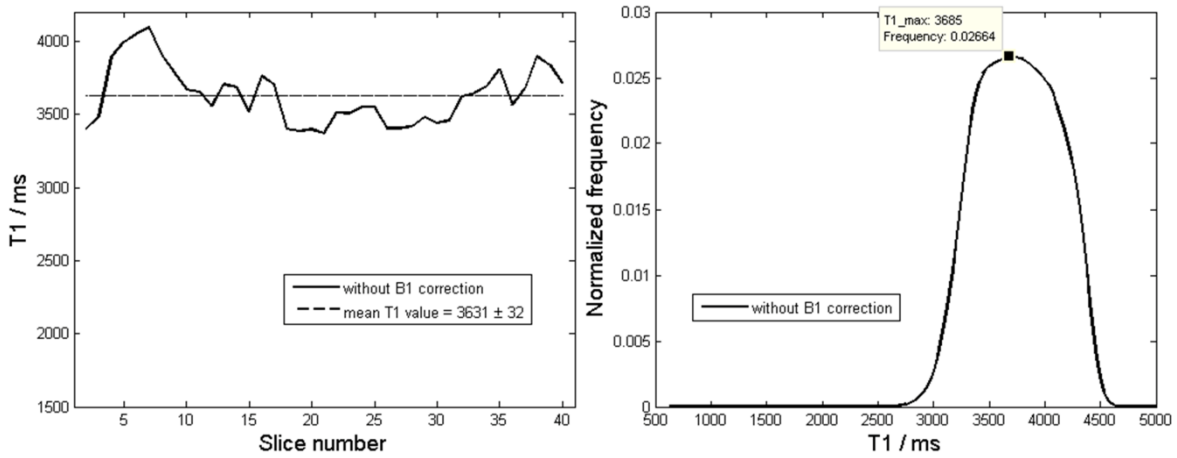

Figure 25. $T1$ values of a water phantom without B_1 correction using 2D ROIs per slice (left) and 3D ROIs (right). Aliasing artifacts were corrected when a 3D acquisition mode with a non-selective excitation pulse was used.

This optimized sequence was then used in in vivo brain imaging. Accordingly, slice profile artifacts were eliminated and a saturation band positioned on the rat lungs prevented the backfolding effect. Non-physiological $T1$ values were then removed from $T1$ histograms of the rat brain (Figure 26). Now, the model containing three Gaussian fits described all the $T1$ values coming from WM, GM and CSF structures in the brain. These findings were also published in a similar fashion in an original article (Martinez Vera et al. 2014).

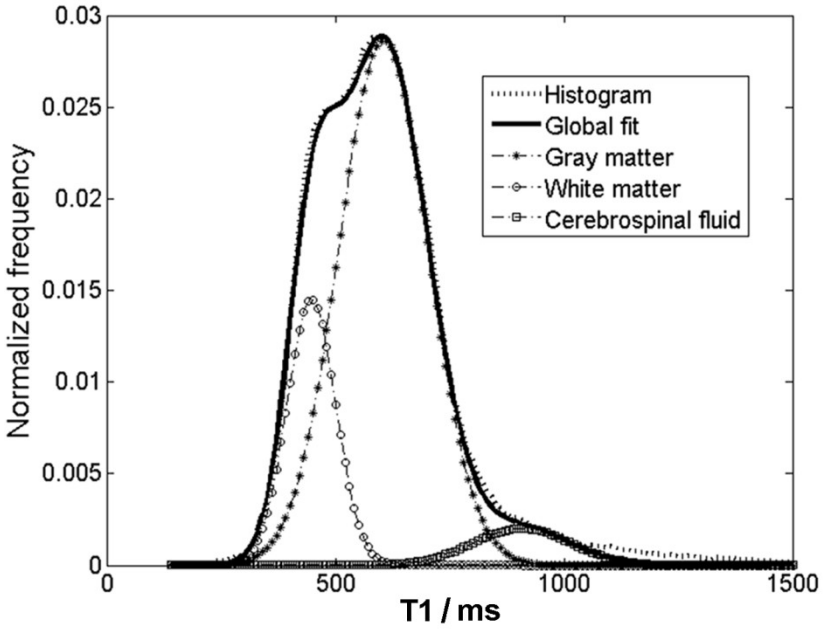

Figure 26. $T1$ values from the whole rat brain (dotted line) were modeled by fitting a triple Gaussian function. Each brain component (white matter (circles), gray matter (diamonds) and cerebrospinal fluid (squares)) was represented by a separate Gaussian peak. Slice profile artifacts were eliminated using a 3D acquisition mode with non-selective slice excitation. Backfolding effect was cancelled by using a saturation band located on the rat lungs. Reproduced from (Martinez Vera et al. 2014), copyright (2014) under the terms of the Creative Commons Attribution License (CC BY 4.0), https://creativecommons.org/licenses/by/4.0/.

MRI protocol

Total experiment time per rat was 65 minutes. Baseline $T1$ mapping (before MLNP injection) lasted 26 minutes and following injection, the second $T1$ mapping lasted 26 minutes and the third 13 minutes. The third measurement only was acquired with FA = 30 º. FA = 6 º was not included here because at low angles, proton-weighting is maximized in these images, i.e. without MLNP effect. Therefore the total experiment time was reduced. The third $T1$ map was calculated using the images acquired with FA = 30 º and the ones acquired from the second measurement with FA = 6 º. These findings were also published in a similar fashion in an original article (Martinez Vera et al. 2014). Some problems encountered during the scans were movement artifacts in the images because the rat was awake and new measurements needed to be repeated. It was important to provide the appropriate and gentle restraint, a sufficient amount of analgesia to render the animal unconscious without loss of vital functions. Despite the care taken, four rats out of the 44 died during experiments because of the anesthesia. An optimal dose was found to be 1.66 µL per gram body weight.

MLNP effect in brain imaging

When nanoparticle density was higher, a higher concentration of contrast agents was obtained, and thus it was possible to detect the MLNPs in an indirect way measuring the loss of MR signal (magnitude image) or gain of MR signal (phase image) using the same voxels but at different time points, before and after the contrast agent administration. This hypointensity and hyperintensity in the brain was clearly seen when the MLNPs were intraventricular injected. Due to the high dose accumulated in the brain, susceptibility artifacts were also present in the MR images (Figure 27).

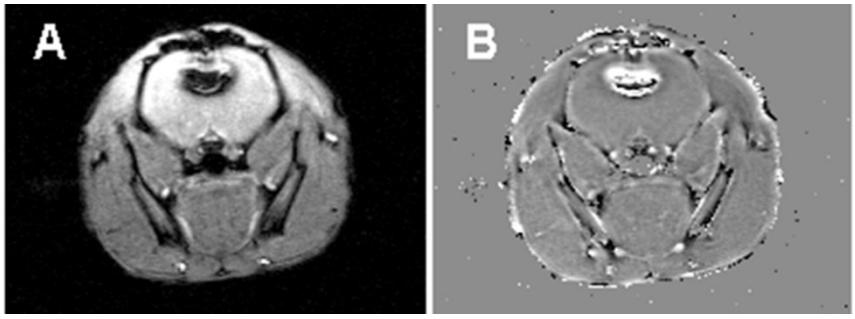

Figure 27. Transversal MR slices of a rat brain. Loss of signal in the magnitude image (A) and hyperintensity in the phase image (B) of the brain can be observed due to the accumulation of magnetite after intraventricular injection of MLNPs.

The histogram technique evaluated the whole brain when NP could be visually assessed neither in MR images nor in the $T1$ maps nor in the susceptibility maps. This technique was particularly appropriate for this kind of nanoparticles where the biological effects were diffuse and widespread. A shift in peak location occurred under the presence of MLNPs. These findings were also published in a similar fashion in an original article (Martinez Vera et al. 2014).

- $T1$ histogram analysis

The Gaussian peak locations of the corresponding brain tissues (WM, GM and CSF) were used to detect the presence of MLNPs in the brain. In the brain, $T1$ histogram analysis revealed a significant MLNP induced shift of the GM and WM peaks towards shorter $T1$ values (Figure 28, and Figure 29A, B). In parallel, the mean fluorescence signal related to MLNPs increased significantly in the

investigated rat brain sections of the CC and HC in the green and red channels (Figure 29C). For all variables, Shapiro-Wilk test for normal distribution accepted normality ($p > 0.05$).

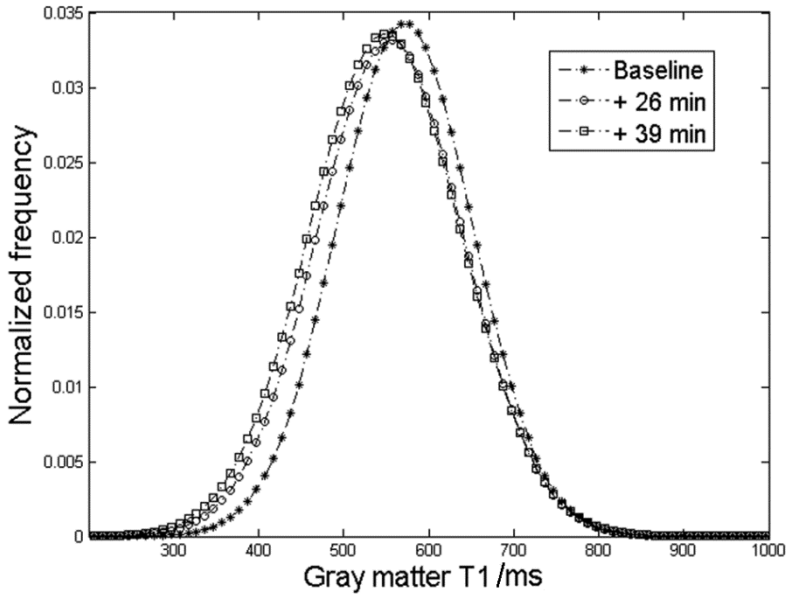

Figure 28. Gray matter $T1$ values (Gaussian peaks) became significantly shorter after 26 and 39 minutes following MLNP injection. Reproduced from (Martinez Vera et al. 2014), copyright (2014) under the terms of the Creative Commons Attribution License (CC BY 4.0), https://creativecommons.org/licenses/by/4.0/.

The relationship between $T1$ changes and results from fluorescence imaging are summarized in Table 12. $T1$ shortening induced by MLNP in GM (Figure 30) and WM correlated with the relative fluorescence signal with the red channel showing the highest sensitivity. Overall, the correlations were higher for the first $T1$ measurement following MLNP injection than at the end of the experiment. Temperature measurement using the rectal probe showed that the mean temperature in rat body decreased by 2.7 °C between the start and end of the brain MRI examination. These findings were also published in an original article (Martinez Vera et al. 2014).

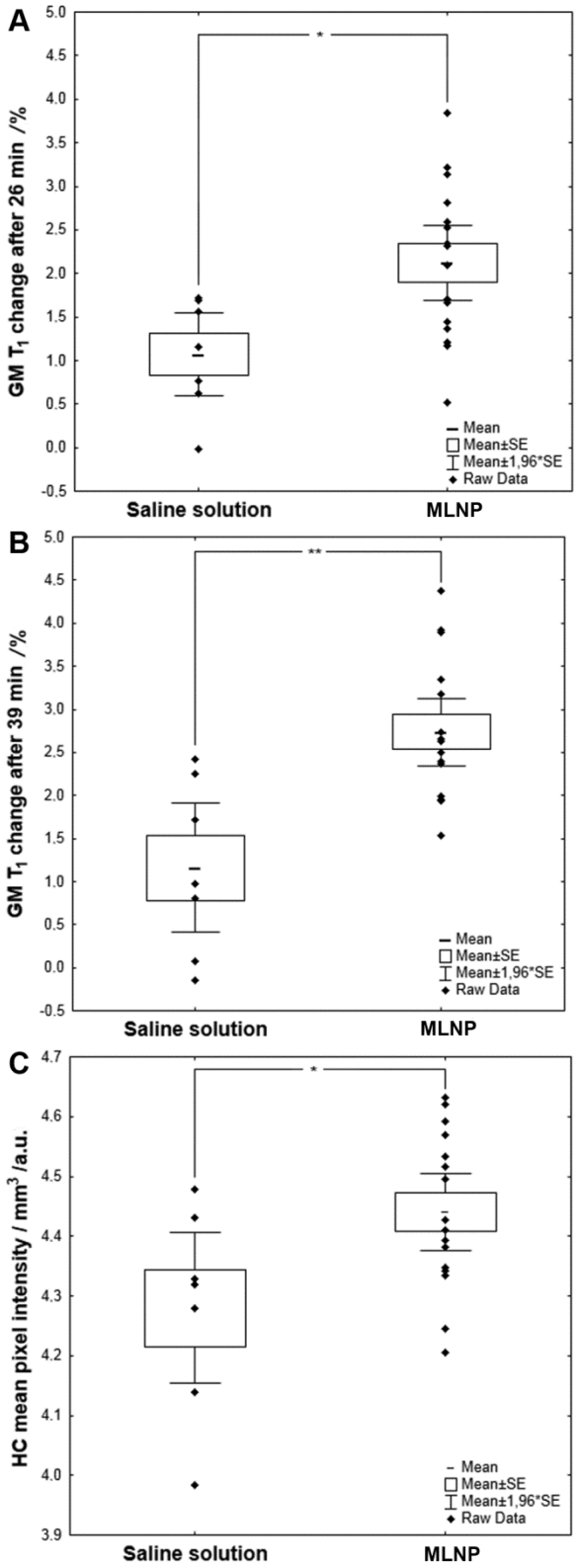

Figure 29. A significant gray matter (GM) $T1$ shortening after 26 minutes (A) and after 39 minutes (B) together with a significantly increase in hippocampus (HC) fluorescence signal intensity in the red channel (C) corresponded to MLNP uptake. * $p < 0.05$; ** $p < 0.01$. Shapiro–Wilk test for T1 changes in control group after 26 minutes $p = 0.40$ and after 39 minutes $p = 0.59$, Shapiro–Wilk test for T1 changes in group treated with MLNP after 26 minutes $p = 0.98$ and after 39 minutes $p = 0.28$. Shapiro–Wilk test for fluorescence signal intensity in saline group $p = 0.55$ and in group treated with MLNP $p = 0.58$. Reproduced from (Martinez Vera et al. 2014), copyright (2014) under the terms of the Creative Commons Attribution License (CC BY 4.0), https://creativecommons.org/ licenses/by/4.0/.

Table 12. $T1$ changes in white matter (WM) and gray matter (GM) linearly correlated with the fluorescence signal intensity of the red channel after MLNP administration. Reproduced from (Martinez Vera et al. 2014), copyright (2014) under the terms of the Creative Commons Attribution License (CC BY 4.0), https://creativecommons.org/licenses/by/4.0/.

Fluorescence in	$T1$-WM1	$T1$-WM2	$T1$-GM1	$T1$-GM2
corpus callosum (CC)	0.675**	0.490*	0.640**	0.625**
hippocampus (HC)	0.612*	0.495*	0.683**	0.610*
CC + HC	0.649**	0.495*	0.664**	0.622*
The Pearson correlation coefficient is shown (* $p < 0.05$; ** $p < 0.01$). The subscripts 1 and 2 correspond to the post injection delay of 26 and 39 min, respectively. These findings have been published in an original article (Martinez Vera et al. 2014).				

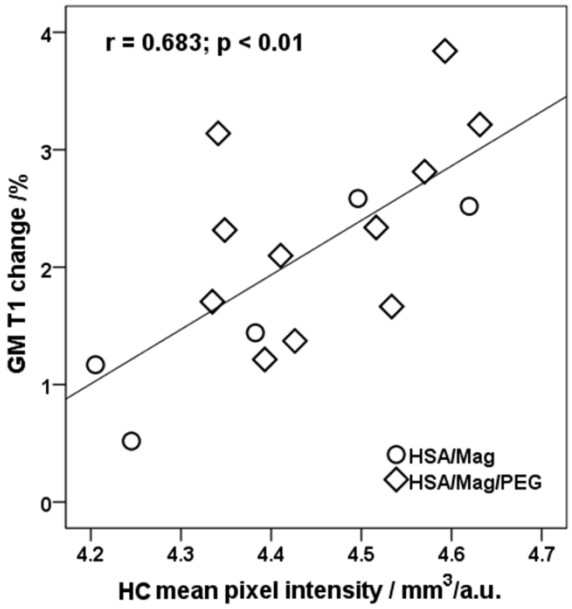

Figure 30. $T1$ shortening in gray matter (GM) of the 16 rats treated with MLNPs linearly correlated with the fluorescence signal intensity in the hippocampus (HC) of the red channel. Reproduced from (Martinez Vera et al. 2014), copyright (2014) under the terms of the Creative Commons Attribution License (CC BY 4.0), https://creativecommons.org/licenses/by/4.0/.

- Susceptibility histogram analysis

Unwrapping and filtering removed global B_0 inhomogeneities (Figure 31B) from the phase images (Figure 31A) and susceptibility weighted maps were obtained with the combination of magnitude and corrected phase images (Figure 31C).

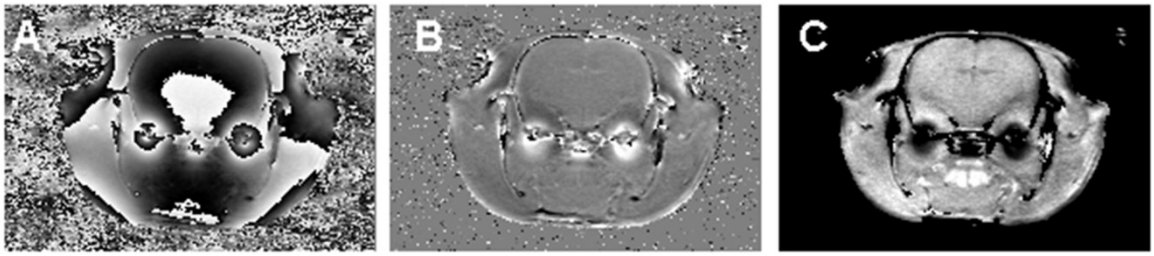

Figure 31. Transversal MR slices of a rat brain. Phase images (A) were first unwrapped and then high pass filtered (B). This corrected phase image was used as mask to multiply magnitude images to obtain susceptibility weighted images (C).

In the brain, susceptibility weighted histogram analysis revealed a significant MLNP contrast enhanced induced shift of the susceptibility SI peak towards larger susceptibility SI (Figure 33) and these values scaled with the HC and CC relative fluorescence signal with the red channel (Figure 32) for the second follow-up scan (Table 13). For all variables, Shapiro-Wilk test for normal distribution accepted normality ($p > 0.05$).

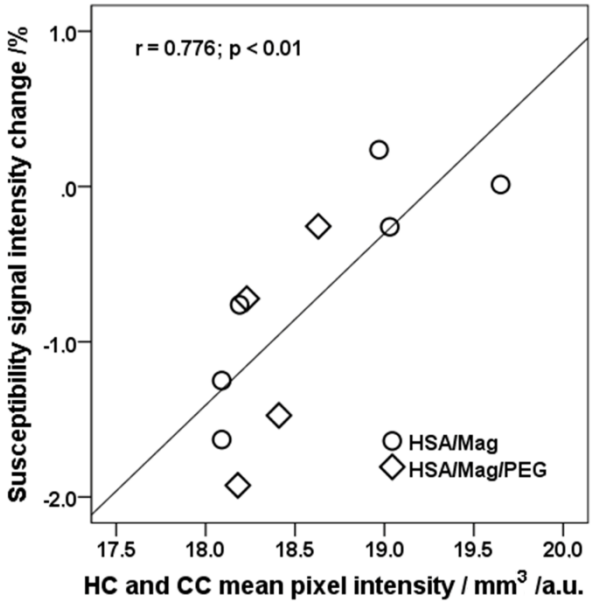

Figure 32. Relationship between susceptibility SI changes in the brain of the 10 rats treated with MLNPs and fluorescence signal in the hippocampus (HC) and corpus callosum (CC) of the red channel.

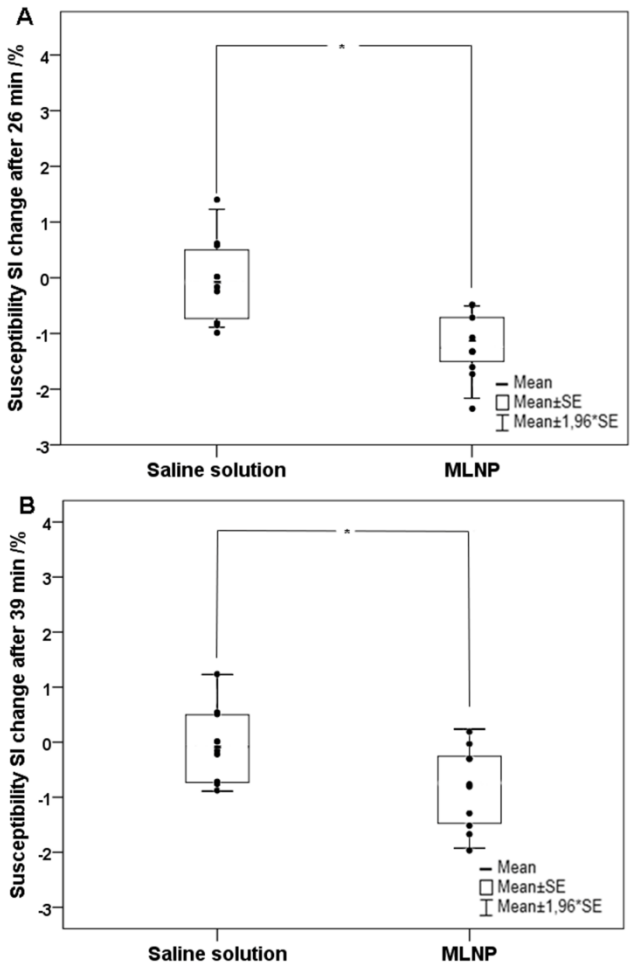

Figure 33. Susceptibility SI values in rats treated with MLNPs were significantly increased in comparison with control group after 26 minutes (A) and after 39 minutes (B). Shapiro–Wilk test for susceptibility change in control group after 26 minutes p = 0.55 and after 39 minutes p = 0.55, Shapiro–Wilk test for susceptibility change in group treated with MLNP after 26 minutes p = 0.61 and after 39 minutes p = 0.65.

Table 13. Relationship between magnetite loaded nanoparticles induced susceptibility changes in the brain and fluorescence signal in the red channel.

	Susceptibility SI1	**Susceptibility SI2**
Fluorescence in CC + HC	0.420	0.776**
The Pearson correlation coefficient is shown (**p < 0.01). SI = Signal intensity. The subscripts 1 and 2 correspond to the post injection delay of 26 and 39 min, respectively.		

Magnetite concentration in the brain

The mean brain temperature using phase mapping decreased from the baseline scan until the first follow-up by 0.10 ºC and by 0.15 ºC until the second one. Magnetite concentration in GM of the brain scaled with the relative fluorescence signal in the HC of the red channel. Here, the correlation was slightly better at the end of the experiment (Figure 34 right) than for the first magnetite concentration measurement following MLNP injection (Figure 34 left).

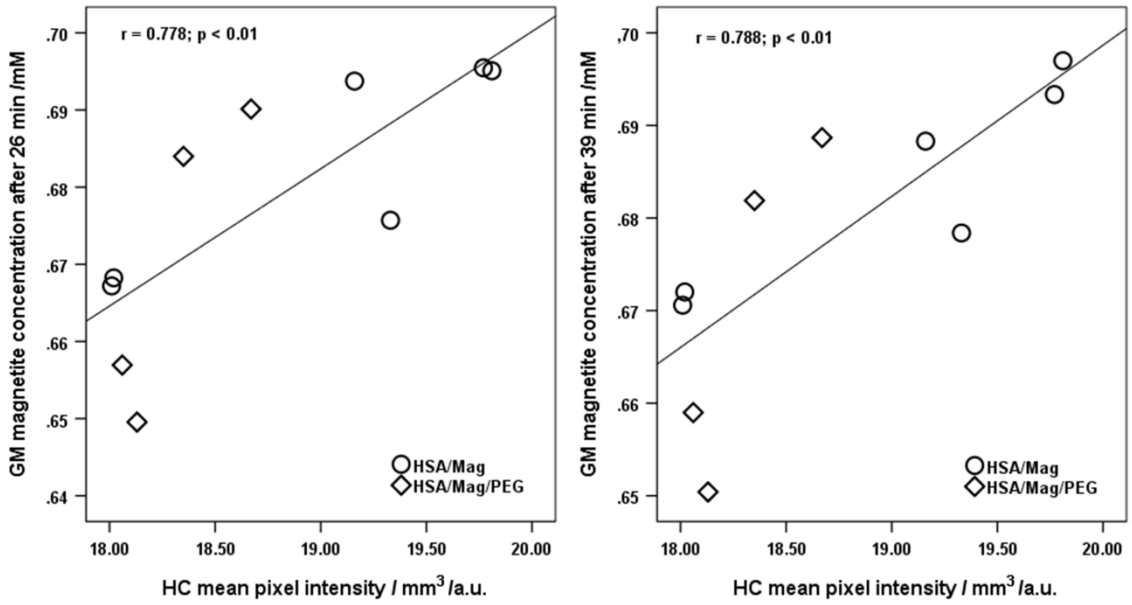

Figure 34. Magnetite concentration in the gray matter (GM) of 10 MLNP treated rats versus fluorescence signal in the hippocampus (HC) of the red channel after 26 minutes (left) and after 39 minutes (right).

3.4. Fluorescence imaging

See results in Appendix B. These findings were also published in an original article (Martinez Vera et al. 2014).

4| Discussion

Some parts of the discussion are reused from (Martinez Vera et al. 2014)

This thesis demonstrates that magnetite labeling enables in vivo tracing of the delivery of NPs to different organs in a rat model using MRI. The first part of this study concentrates on the characterization of different MLNP formulations, which is performed using samples with different magnetite concentrations and different MRI sequences. In the IR-sequence, NP induced signal intensity changes are directly influenced by the magnetite concentration and by sequence parameters such as the inversion time. In the DESPOT1-sequence, the $T1$ contrast is driven by TR and the FA. The dominant source of error in the accuracy of $T1$ using DESPOT1 is the imprecise knowledge of the FA used. Errors in the FA arises from two main sources: transmitter B_1 inhomogeneities and slice profile errors (Deoni et al. 2003). Variation in B_1 may occur due to either RF coil nonuniformities or RF attenuation, meaning B_1 inhomogenities lead to spatial variation of SI in the MR images (Figure 11A). B_1 inhomogeneities were corrected in this work using the methods DAM (Figure 11B) and BS shift (Figure 11C). The BS shift was eventually selected for the final protocol to correct for B_1 inhomogeneities due to its reduced acquisition time. However, in samples containing MLNPs, B_1 inhomogeneities arise because the RF power is absorbed differently across the object so when a high concentration of magnetite is present (high susceptibility effect), the BS shift method fails (Figure 12B) and flip angles across the samples cannot be accurately corrected. The DESPOT1 studies demonstrated the influence of the flip angle on the precision of $T1$ estimation. The importance of FA choice depending on $TR/T1$ was analyzed in Deoni et al. 2003. In the present work, samples with higher magnetite concentration (i.e. shorter $T1$ values) reach the Ernst angle when MR signal is maximized, with higher flip angles (Figure 9). DESPOT1 is also optimized here using only two flip angles (Figure 13) and the use of a 3D DESPOT1-sequence reduces scan time and also improves $T1$ mapping by minimizing slice profile errors and improving SNR (Figure 14). Embedding different concentrations of MLNPs in samples allows $T1$ relaxivity assessment as well as susceptibility effect assessment by $T2^*$. Results from phantom studies suggest that the relaxivity of the MLNPs is high enough to allow detection of even low concentrations in vivo. In agreement with relaxation theory, it could be shown that $R1$ linearly increases with MLNP concentration but also that the relaxivity is mostly determined by the

size of the magnetite. A smaller size of paramagnetic particles increases $R1$ relaxivity while $R2$* relaxivity increases with particle size (Roohi et al. 2012). Given the limited SNR and readout bandwidth provided by a clinical scanner, this was also the reason why this work focused on $R1$ effects rather than on $R2$* effects in the current investigations. Quantitative assessment of $R2$* would require a gradient echo sequence with at least two echoes, but the minimum echo times resulting from a limited readout gradient at a small field of view may not be optimal for assessing regions with a high MLNP concentration. Moreover, this thesis did not look for focal and macroscopically visible effects of MLNP accumulation but rather for global effects.

This work dealt with the adaptation of a clinical scanner for small animal imaging, such as in mice or rats. Image quality and protocol efficiency were assessed by evaluating these two small animal types and for this purpose, different protocols and MRI sequences were investigated depending on the animal used. High resolution structural small animal MRI is fundamentally limited by SNR. To attain optimum signal at clinical field strengths, specially tailored coils have to be used and sequences need to be optimized. The microcoil used in mouse imaging and the CPC coil used in rat imaging exhibits a signal dependency with distance r from the coil centre that causes signal variations across images (Figure 16 and Figure 22A, C). This variation can be improved by placing the animal closer to the coils, for the CPC coil, and this entails the use of thin animal holders (Figure 21). On the other hand, the wrist coil provides higher SNR originating from the brain than the CPC coil, although with less homogeneity (Figure 22, Table 11). Subsequently, as the dimensions of the bore of the wrist coil (400 mm × 400 mm × 300 mm, (L × W × H)) is larger than the brain size of the rat, it is important to carefully place the brain of the rat at the isocenter of the wrist coil where the uniformity of the B_1-field is maximum. The wrist coil also improves the animal set up as the additional gel bottles are no longer required. The PSIR FSE-sequence provided the best image quality in abdominal imaging (voxel size = 0.47×0.47×1.44 mm^3) with enhanced contrast between body structures and without motion artifacts. The traditional magnitude reconstruction of the IR-sequence automatically restricts the range of the $T1$-weighted factor from 0 to $(1 - exp\left[-\frac{TR}{T1}\right])$. Under magnitude reconstruction, air and any tissue which magnetization are zero at time TI, appears black. The

advantage of the PS reconstructed IR is that it doubles the range of the contrast. Artifacts caused by motion due to breathing occur only because the artifact area contributes to the overall signal. This undesired signal is reduced using a spatial saturation slab in the lung region (Figure 15). Presaturation RF pulses destroys the magnetization in this region and its small signal component did not lead to interferences in the other abdominal regions. The sequence parameters selected in body imaging also allow the detection of the MLNPs which produce a brighter signal in the abdominal rat images (Figure 19 and Figure 20). In parallel with body imaging a high resolution sequence to probe effects of nanoparticles in the brain was developed and optimized. A fast non-selective 3D DESPOT1-sequence for $T1$ mapping achieves short scan times (26 min) and also provides susceptibility weighted contrast images by combining magnitude and phase images. The 3D DESPOT1-sequence also delivers high resolution images (voxel size = 0.21×0.21×1 mm^3) in rat brain imaging which is essential when registering follow-up scans with baseline scans using the provided structural anatomical information. Animal sedation was improved through placement of the catheter in the right leg vein (Figure 5C) which allows maintenance of an opened via to inject anesthesia and nanoparticles without needing to remove the animal from the scanner (Figure 5B). Using this method, the cable-based supply of anesthesia (Figure 3D) and the problematic injection of MLNPs through the mouse tail vein, which was unable to guarantee the introduction of MLNPs in the circulatory system, were eliminated. While the accumulation of MLNPs was clearly visible in some organs (Figure 19 and Figure 20), visual inspection failed to discern MLNP uptake in the brain. This was not unexpected because the blood-brain barrier usually blocks compounds of the size administered in current work. Zensi et al. 2009 and Wagner et al. 2012 suggested that PEGylated HSA nanoparticles are unselectively retained within the endothelial cells by showing that after injection of these nanoparticles only a small number of them were visible in the endothelial cells of the blood-brain barrier. However, a slight but global $T1$ change in the white and gray matter brain tissue compartments was demonstrated in this work by using the proposed histogram technique. The three major tissue compartments could be defined using a triple Gaussian model (Figure 26). Contributions from the basal ganglia and cortex structures were represented by the dominant gray matter peak, while a smaller peak represented contributions from white matter. The cerebrospinal fluid was also

represented by an additional peak. The kinetics of the HSA based MLNPs is not fully clear but it seems that accumulation in the brain, spleen and liver occurs at a higher rate (Figure 19) and that the time constant for clearing is more than one week (Figure 20).

$T1$ changes correlated linearly with the fluorescence signal intensity (Figure 29, Table 12) where fluorescence imaging attests to the high sensitivity of this analysis and imaging approach. It is not yet clear if the fluorescence signal from magnetically labeled nanoparticles stems from the magnetite, or additionally from the serum albumin. However, validation with Prussian blue staining and control rats, where iron is bound within the complex alters the excitability of the magnetite molecules, suggesting that the magnetite is responsible for the high fluorescence signal (Figure B-2 and Figure B-3). Although significant correlations were found for all regions, the higher blood volume in gray matter, thus allowing for more pronounced MLNP effects, may explain why the best linear relationship was found between the $T1$ change in gray matter and the fluorescence signal in the hippocampus (Figure 30). Magnetite nanoparticles is a contrast medium which, after intravenous administration, can cause a greater inhomogeneity effect on local magnetic field, resulting in higher susceptibility differences between the MR acquisitions. MLNP-enhanced SWI statistically increased susceptibility SI in comparison with the control group in both follow-up scans (Figure 33). These susceptibility changes in the brain highly scaled with the relative fluorescence signal originating from both HC and CC of the red channel, however only for the second follow-up scan (Table 13, Figure 32). MLNP-enhanced SWI offers support of the hypothesis that magnetite is present in the GM and WM, however these susceptibility histograms, unlike their $T1$ counterparts, cannot distinguish between brain structures. Green fluorescent background signal was found to be generally higher in all compartments at equal exposure time. This is partially due to natural emission (Zipfel et al. 2003), but also due to PFA fixation which enhances green fluorescence. This may explain why a higher correlation was found for the red channel. Interestingly, the correlation coefficients between MRI and fluorescence signal were generally lower for the second $T1$ measurement, i.e. the one that was performed before sacrificing the animals and therefore should be more closely related to the ex vivo data. A possible explanation for this observation is that the

effect of cooling of the brains was not considered. As $T1$ depends on brain temperature (Rieke & Butts Pauly 2008; Birkl et al. 2014), the anesthesia induced a temperature drop that has an effect in the same direction as the uptake of MLNPs and therefore may have affected the correlation analysis. Another point is that the permeability of the BBB decreases at lower temperatures (Kiyatkin & Sharma 2009) which could counteract the temperature induced shortening of T1. It was not able to correct for the temperature effect, because no significant relationship between brain $T1$ and temperature in the rectum was found. Relative temperature change can be measured by comparing the data from the follow-up scans to the data from the baseline scan (measured mean baseline rectal temperature was (36.05 $\pm$ 0.03) °C), when all acquisitions are performed under identical experimental conditions. Phase mapping using the PRF shift permits the calculation of MRI-derived temperature maps by measuring the phase change resulting from the temperature-dependent change in resonance frequency (Rieke & Butts Pauly 2008). Using phase mapping the mean brain temperature decreased by (0.15 $\pm$ 0.23) °C in comparison with the mean rectal temperature which decreased by (2.7 $\pm$ 0.4) °C. The determination of magnetite concentration in the brain considered $T1$ changes due to the magnetite susceptibility and the effect of brain cooling. In this part of the study, the MLNPs were chosen to have the smallest diameter (110 nm) to ensure the minimal macrophage response (S. S. Yu et al. 2012) and higher interaction with the BBB. A mean concentration of (0.68 $\pm$ 0.02) mM was found to reach the gray matter in the brain. These results strongly correlated with the signal intensity derived by fluorescence imaging from HC red channel (Figure 34), corroborating the fact that MLNP are present in structures with higher blood volume.

Limitations of the study and future research lines

Due to anesthesia, the body temperature of the rats dropped approximately 10 % over the span of the MRI experiments. Therefore, in new experiments the effect of brain cooling is to be taken into account by an appropriate brain temperature measurement, or by using a heating pad to keep the rat body at a constant temperature.

Given the results in the brain studies, it can be concluded that only a very low percentage has entered the brain. However, the experiments cannot exclude the possibility that magnetically labeled nanoparticles might have been degraded because MRI only probes the presence of magnetite in brain tissue. On the other hand, it is not possible from the data to separate between nanoparticles that really crossed blood-brain barrier and NPs that become stuck in the vascular endothelia. To achieve higher rates of brain MLNP uptake, further research is needed. An aspect to improve is the size of the MLNPs. The NP size is a characteristic that strongly influences the iteration between nanoparticles and immune components which are activated in a size-dependent manner (NP < 1000 nm) (Harashima et al. 1994; Devine et al. 1994; Song et al. 2014). Smaller size NPs (< 100 nm) have been shown to be preferable due to slower removal from the blood (Kaushik et al. 2014; Kaushik et al. 2017). The MLNPs used in this work are > 100 nm and are coated with PEG which protects the NPs from immune recognition. It would be of great interest to explore the possibilities of making and characterizing these MLNPs of smaller dimensions in order to make NPs less easily recognized and taken up by monocytes and macrophages. Another aspect is to achieve higher rates of brain MLNP uptake. Even though in vitro studies have delivered proof that transport across the BBB for drug delivery to the CNS is optimal with NPs that are 100-150 nm, further research is needed to determine ways to modify MLNPs which promote MLNP transport over the BBB. Respective investigations are under way, for example one of the research groups involved in this thesis has already commenced experiments on MLNP modification with apolipoprotein E (Zensi et al. 2009; Wagner et al. 2010; Wagner et al. 2012).

5| Conclusions

In conclusion, it was demonstrated that NPs can be magnetically labeled such that they are traceable using MR $T1$ relaxometry and SWI. Despite the use of a clinical MRI scanner with limited sensitivity, it was possible to visually detect MLNPs in the liver and spleen of the rat. Furthermore, the detection of a diffuse and global accumulation of MLNPs in the rat brain was also feasible by the implementation of a new histogram based analysis technique and even to determine the concentration of magnetite that reaches the blood-brain-barrier. The specificity of this method which could detect in vivo MLNPs without visible accumulation of this contrast agent in the brain is of great of interest for investigating drug loaded MLNP for AD and other brain diseases.

6 References

Abbott, N.J., Rönnbäck, L. & Hansson, E., 2006. Astrocyte-endothelial interactions at the blood-brain barrier. *Nat Rev Neurosci.*, 7(1), pp.41–53.

Alam, M.I. et al., 2010. Strategy for effective brain drug delivery. *Eur J Pharm Sci.*, 40(5), pp.385–403.

Alqudami, A. & Annapoorni, S., 2007. Fluorescence From Metallic Silver and Iron Nanoparticles Prepared by Exploding Wire Technique. *Plasmonics*, 2(1), pp.5–13.

Alzheimer, A. et al., 1995. An English translation of Alzheimer's 1907 paper, "uber eine eigenartige erkankung der hirnrinde." *Clin Anat.*, 8(6), pp.429–31.

Alzheimer, A., 1907. Uber eine eigenartige Erkrankung der Hirnrinde. *Allg Zeits Psychiatry Psychisch Y Gerichtlich Med*, 64, pp.146–8.

Axel, L., 1984. Blood Flow Effects in Magnetic Resonance Imaging. *AJR Am J Roentgenol.*, 143(6), pp.1157–66.

Banks, W.A., 2012. Drug delivery to the brain in Alzheimer's disease: consideration of the blood-brain barrier. *Adv Drug Deliv Rev.*, 64(7), pp.629–39.

Beduneau, A. et al., 2009. Facilitated monocyte-macrophage uptake and tissue distribution of superparmagnetic iron-oxide nanoparticles. *PLoS One*, 4(2), p.e4343.

Begley, D.J., 2003. Understanding and circumventing the blood-brain barrier. *Acta Paediatr Suppl.*, 92(443), pp.83–91.

Birkl, C. et al., 2014. Temperature-induced changes of magnetic resonance relaxation times in the human brain: A postmortem study. *Magn Reson Med.*, 71(4), pp.1575–80.

Bloch, F. & Siegert, A., 1940. Magnetic Resonance for Nonrotating Fields. *Phys. Rev.*, 57(6), pp.522–527.

Boros, E. et al., 2012. Gd(DOTAla): a single amino acid Gd-complex as a modular tool for high relaxivity MR contrast agent development. *J Am Chem Soc.*, 134(48), pp.19858–68.

Brisset, J. et al., 2011. Quantification of Iron-Labeled Cells with Positive Contrast in Mouse Brains. *Mol Imaging Biol.*, 13(4), pp.672–8.

Brockmann, M.A., Kemmling, A. & Groden, C., 2007. Current issues and perspectives in small rodent magnetic resonance imaging using clinical MRI scanners. *Methods*, 43(1), pp.79–87.

Butt, A.M., Jones, H.C. & Abbott, N.J., 1990. Electrical resistance across the blood-brain barrier in anaesthetized rats: a developmental study. *J Physiol.*, 429, pp.47–62.

Castelli, D.D. et al., 2013. Nanoparticle-based chemical exchange saturation transfer (CEST) agents. *NMR Biomed.*, 26(7), pp.839–49.

Cheng, Z. et al., 2013. Multifunctional Nanoparticles: Cost versus benefit of adding targeting and imaging capabilities. *Science.*, 338(6109), pp.903–910.

Christensen K.A. et al., 1974. Optimal determination of relaxation times of Fourier transform nuclear magnetic resonance. Determination of spin-lattice relaxation times in chemically polarized species. *J. Phys. Chem.*, 78(19), pp.1971–1977.

Crone, C. & Olesen, S.P., 1982. Electrical resistance of brain microvascular endothelium. *Brain Res.*, 241(1), pp.49–55.

Deoni, S.C., 2007. High-resolution T1 mapping of the brain at 3T with driven equilibrium single pulse observation of T1 with high-speed incorporation of RF field inhomogeneities (DESPOT1-HIFI). *J Magn Reson Imaging.*, 26(4),

pp.1106–11.
Deoni, S.C., Peters, T.M. & Rutt, B.K., 2004. Determination of Optimal Angles for Variable Nutation Proton Magnetic Spin-Lattice, T1, and Spin-Spin, T2, Relaxation Times Measurement. *Magn Reson Med.*, 51(1), pp.194–9.
Deoni, S.C.L., Rutt, B.K. & Peters, T.M., 2003. Rapid combined T1 and T2 mapping using gradient recalled acquisition in the steady state. *Magn Reson Med.*, 49(3), pp.515–26.
Devine, D. et al., 1994. Liposome-complement interactions in rat serum: implications for liposome survival studies. *Biochim Biophys Acta.*, 1191(1), pp.43–51.
Dubois, B. et al., 2007. Research criteria for the diagnosis of Alzheimer's disease: revising the NINCDS-ADRDA criteria. *Lancet Neurol.*, 6(8), pp.734–46.
Dyrna, F. et al., 2013. The blood-brain barrier. *J Neuroimmune Pharmacol.*, 8(4), pp.763–73.
Ehrlich, P., 1885. *Das Sauerstoff-Bedürfniss des Organismus : eine farbenanalytische Studi*, Berlin : Hirschwald.
Eibofner, F. et al., 2010. Positive Contrast Imaging of Iron Oxide Nanoparticles With Susceptibility-Weighted Imaging. *Magn Reson Med.*, 64(4), pp.1027–38.
El-Ghundi, M., O'Dowd, B.F. & George, S.R., 2007. Insights into the role of dopamine receptor systems in learning and memory. *Rev Neurosci.*, 18(1), pp.37–66.
Geerts, H., 2007. Drug evaluation: (R)-flurbiprofen--an enantiomer of flurbiprofen for the treatment of Alzheimer's disease. *IDrugs.*, 10(2), pp.121–33.
Geraldes, C.F.G.C. & Laurent, S., 2009. Classification and basic properties of contrast agents for magnetic resonance imaging. *Contrast Media Mol Imaging.*, 4(1), pp.1–23.
Gossuin, Y. et al., 2009. Magnetic resonance relaxation properties of superparamagnetic particles. *Wiley Interdiscip Rev Nanomed Nanobiotechnol.*, 1(3), pp.299–310.
Graves, M.J., 2007. Pulse sequences for contrast-enhanced magnetic resonance imaging. *Radiography*, 13(Supplement 1), pp.e20–e30.
Haacke, E.M. & Reichenbach, J.R., 2011. *Susceptibility Weighted Imaging in MRI: Basic Concepts and Clinical Applications*, Wiley-Blackwell.
Hahn, E.L., 1950. Spin Echoes. *Phys. Rev.*, 80(4), pp.580–594.
Hao, R. et al., 2013. Developing Fe3O4 nanoparticles into an efficient multimodality imaging and therapeutic probe. *Nanoscale*, 5(23), pp.11954–63.
Harashima, H. et al., 1994. Enhanced hepatic uptake of liposomes through complement activation depending on the size of liposomes. *Pharm Res.*, 11(3), pp.402–6.
Hardy, J., 2006. A Hundred Years of Alzheimer's Disease Research. *Neuron.*, 52(1), pp.3–13.
Herrmann, K.H. et al., 2012. Possibilities and limitations for high resolution small animal MRI on a clinical whole-body 3T scanner. *Magma*, 25(3), pp.233–44.
Hornak, J.P., Szumowski, J. & Bryant, R.G., 1988. Magnetic field mapping. *Magn Reson Med.*, 6(2), pp.158–63.
Hu, F. & Zhao, Y.S., 2012. Inorganic nanoparticle-based T1 and T1/T2 magnetic resonance contrast probes. *Nanoscale*, 4(20), pp.6235–43.
Huang, J. et al., 2012. Improving the magnetic resonance imaging contrast and detection methods with engineered magnetic nanoparticles. *Theranostics*, 2(1), pp.86–102.

Insko, E.K. & Bolinger, L., 1993. Mapping of the Radiofrequency Field. *J Magn Reson.*, Series A(1), pp.82–85.

Ishihara, Y. et al., 1995. A precise and fast temperature mapping using water proton chemical shift. *Magn Reson Med.*, 34(6), pp.814–23.

Jack, C.R.J. et al., 2010. Hypothetical model of dynamic biomarkers of the Alzheimer's pathological cascade. *Lancet Neurol.*, 9(1), pp.119–28.

Jokerst, J. V et al., 2011. Nanoparticle PEGylation for imaging and therapy. *Nanomedicine (Lond)*, 6(4), pp.715–28.

De Jong, W.H. & Borm, P.J. a, 2008. Drug delivery and nanoparticles:applications and hazards. *Int J Nanomedicine.*, 3(2), pp.133–49.

Kaushik, A. et al., 2017. Personalized nanomedicine for CNS diseases. *Drug Discov Today*, 0(0).

Kaushik, A. et al., 2014. The potential of magneto-electric nanocarriers for drug delivery. *Expert Opin Drug Deliv.*, 11(10), pp.1635–46.

Kim, B.H. et al., 2011. Large-scale synthesis of uniform and extremely small-sized iron oxide nanoparticles for high-resolution T1 magnetic resonance imaging contrast agents. *J Am Chem Soc.*, 133(32), pp.12624–31.

Kim, J. & Mook-Jung, I., 2015. Special issue on neurodegenerative diseases and their therapeutic approaches. *Exp Mol Med.*, 47, p.e146.

Kim, T. et al., 2011. Mesoporous silica-coated hollow manganese oxide nanoparticles as positive T1 contrast agents for labeling and MRI tracking of adipose-derived mesenchymal stem cells. *J Am Chem Soc.*, 133(9), pp.2955–61.

Kiyatkin, E. & Sharma, H., 2009. Permeability of the blood-brain barrier depends on brain temperature. *Neuroscience*, 161(3), pp.926–39.

Kreuter, J. et al., 2002. Apolipoprotein-mediated transport of nanoparticle-bound drugs across the blood-brain barrier. *J Drug Target.*, 10(4), pp.317–25.

Kreuter, J. et al., 2007. Covalent attachment of apolipoprotein A-I and apolipoprotein B-100 to albumin nanoparticles enables drug transport into the brain. *J Control Release*, 118(1), pp.54–8.

Kreuter, J. et al., 1995. Passage of peptides through the blood-brain barrier with colloidal polymer particles (nanoparticles). *Brain Res.*, 674(1), pp.171–4.

Langer, K. et al., 2003. Optimization of the preparation process for human serum albumin (HSA) nanoparticles. *Int J Pharm.*, 257(1–2), pp.169–80.

Lardenoije, R. et al., 2015. The epigenetics of aging and neurodegeneration. *Prog Neurobiol.*, 131, pp.21–64.

Lee, N. et al., 2012. Water-dispersible ferrimagnetic iron oxide nanocubes with extremely high r2 relaxivity for highly sensitive in vivo MRI of tumors. *Nano Lett.*, 12(6), pp.3127–31.

Löw, K. et al., 2011. Targeted human serum albumin nanoparticles for specific uptake in EGFR-Expressing colon carcinoma cells. *Nanomedicine*, 7(4), pp.454–63.

M. Jenkinson et al., 2002. Improved optimisation for the robust and accurate linear registration and motion correction of brain images. *Neuroimage*, 17(2), pp.825–41.

M. Jenkinson & Smith, S.M., 2001. A global optimisation method for robust affine registration of brain images. *Med Image Anal.*, 5(2), pp.143–56.

Martinez Vera, N.P. et al., 2014. Tracking of Magnetite Labeled Nanoparticles in the Rat Brain Using MRI. *PLoS One*, 9(3), p.e92068.

Marzola, P., Osculati, F. & Sbarbati, A., 2003. High field MRI in preclinical research. *Eur J Radiol.*, 48(2), pp.165–70.

McMahon, M.T. et al., 2006. Quantifying exchange rates in chemical exchange saturation transfer agents using the saturation time and saturation power dependencies of the magnetization transfer effect on the magnetic resonance imaging signal (QUEST and QUESP): Ph calibration for poly. *Magn Reson Med.*, 55(4), pp.836–47.

Meister, S. et al., 2013. Nanoparticulate flurbiprofen reduces amyloid-β42 generation in an in vitro blood-brain barrier model. *Alzheimers Res Ther.*, 5(6), p.51.

Musiek, E.S., Xiong, D.D. & Holtzman, D.M., 2015. Sleep, circadian rhythms, and the pathogenesis of Alzheimer disease. *Exp Mol Med.*, 47, p.e148.

Na, H. Bin et al., 2007. Development of a T1 contrast agent for magnetic resonance imaging using MnO nanoparticles. *Angew Chem Int Ed Engl.*, 46(28), pp.5397–401.

Naahidi, S. et al., 2013. Biocompatibility of engineered nanoparticles for drug delivery. *J Control Release.*, 166(2), pp.182–94.

Nasrallah, I.M. & Wolk, D.A., 2014. Multimodality Imaging of Alzheimer Disease and Other Neurodegenerative Dementias. *J Nucl Med.*, 55(12), pp.2003–11.

Pelaz, B. et al., 2013. Interfacing engineered nanoparticles with biological systems: anticipating adverse nano-bio interactions. *Small*, 9(9–10), pp.1573–84.

Pillai, D.R. et al., 2011. Comprehensive small animal imaging strategies on a clinical 3 T dedicated head MR-scanner; adapted methods and sequence protocols in CNS pathologies. *PLoS One*, 6(2), p.e16091.

Prince, M. et al., 2015. World Alzheimer Report 2015: The Global Impact of Dementia - An analysis of prevalence, incidence, cost and trends. *Alzheimer's Disease International*, p.84.

Rempe, R. et al., 2014. Strategies to overcome the barrier: use of nanoparticles as carriers and modulators of barrier properties. *Cell Tissue Res.*, 355(3), pp.717–26.

Rieke, V. & Butts Pauly, K., 2008. MR thermometry. *J Magn Reson Imaging*, 27(2), pp.376–90.

Ritchie, K. & Lovestone, S., 2002. The Dementias. *Lancet*, 360(9347), pp.1759–66.

Roohi, F. et al., 2012. Studying the effect of particle size and coating type on the blood kinetics of superparamagnetic iron oxide nanoparticles. *Int J Nanomedicine*, 7, pp.4447–58.

Rümenapp, C., Gleich, B. & Haase, A., 2012. Magnetic nanoparticles in magnetic resonance imaging and diagnostics. *Pharm Res.*, 29(5), pp.1165–79.

Sacolick, L.I. et al., 2010. B1 mapping by Bloch-Siegert shift. *Magn Reson Med.*, 63(5), pp.1315–22.

Sariñana, J. & Tonegawa, S., 2016. Differentiation of forebrain and hippocampal dopamine 1-class receptors, D1R and D5R, in spatial learning and memory. *Hippocampus*, 26(1), pp.76–86.

Schenck, J.F., 1996. The role of magnetic susceptibility in magnetic resonance imaging: MRI magnetic compatibility of the first and second kinds. *Med Phys.*, 23(6), pp.815–50.

Schröder, L. et al., 2006. Molecular imaging using a targeted magnetic resonance hyperpolarized biosensor. *Science*, 314(5798), pp.446–9.

Silva, G. a, 2010. Nanotechnology applications and approaches for neuroregeneration and drug delivery to the central nervous system. *Ann N Y Acad Sci.*, 1199, pp.221–30.

Siwach, O.P. & Sen, P., 2008. Fluorescence properties of Fe nanoparticles prepared by electro-explosion of wires. *Mater Sci Eng B Solid State Mater Adv Technol*, 149(1), pp.99–104.

Soesbe, T.C., Wu, Y. & Dean Sherry, A., 2013. Advantages of paramagnetic chemical exchange saturation transfer (CEST) complexes having slow to intermediate water exchange properties as responsive MRI agents. *NMR Biomed.*, 26(7), pp.829–38.

Song, G. et al., 2014. Nanoparticles and the Mononuclear Phagocyte System : Pharmacokinetics and Applications for Inflammatory Diseases. *Curr Rheumatol Rev.*, 10(1), pp.22–34.

Sperling, R. a, Mormino, E. & Johnson, K., 2014. The evolution of preclinical Alzheimer's disease: Implications for prevention trials. *Neuron*, 84(3), pp.608–22.

Stephen, Z.R., Kievit, F.M. & Zhang, M., 2011. Magnetite Nanoparticles for Medical MR Imaging. *Mater Today (Kidlington)*, 14(7–8), pp.330–38.

Stollberger, R. & Wach, P., 1996. Imaging of the Active B1 Field In Vivo. *Magn Reson Med.*, 35(2), pp.246–51.

Storp, B. Von et al., 2012. Albumin nanoparticles with predictable size by desolvation procedure. *J Microencapsul.*, 29(2), pp.138–46.

Tromsdorf, U.I. et al., 2009. A highly effective, nontoxic T1 MR contrast agent based on ultrasmall PEGylated iron oxide nanoparticles. *Nano Lett.*, 9(12), pp.4434–40.

Tu, C. & Louie, A.Y., 2012. Nanoformulations for molecular MRI. *Wiley Interdiscip Rev Nanomed Nanobiotechnol.*, 4(4), pp.448–57.

Viatonou, S. et al., 2009. Predictors of rapid cognitive decline among demented subjects aged 75 or more: ('Sujet Age Fragile--Evaluation et Suivi' Cohort-SAFES). *Int J Geriatr Psychiatry*, 24(7), pp.709–15.

Wagner, S. et al., 2010. Nanoparticulate transport of oximes over an in vitro blood-brain barrier model. *PLoS One*, 5(12), p.e14213.

Wagner, S. et al., 2012. Uptake mechanism of ApoE-modified nanoparticles on brain capillary endothelial cells as a blood-brain barrier model. *PLoS One*, 7(3), p.e32568.

Wahajuddin & Arora, S., 2012. Superparamagnetic iron oxide nanoparticles: magnetic nanoplatforms as drug carriers. *Int J Nanomedicine*, 7, pp.3445–71.

Wang, Q. et al., 2008. Chronic treatment with simvastatin upregulates muscarinic M1/4 receptor binding in the rat brain. *Neuroscience*, 154(3), pp.1100–6.

Wang, Y. et al., 2000. Artery and vein separation using susceptibility-dependent phase in contrast-enhanced MRA. *J Magn Reson Imaging*, 12(5), pp.661–70.

Ward, K.M., Aletras, a H. & Balaban, R.S., 2000. A new class of contrast agents for MRI based on proton chemical exchange dependent saturation transfer (CEST). *J Magn Reson.*, 143(1), pp.79–87.

Weber, C., Coester, C., et al., 2000. Desolvation process and surface characterisation of protein nanoparticles. *Int J Pharm.*, 194(1), pp.91–102.

Weber, C., Kreuter, J. & Langer, K., 2000. Desolvation process and surface characteristics of HSA-nanoparticles. *Int J Pharm.*, 196(2), pp.197–200.

Weber, C., Reiss, S. & Langer, K., 2000. Preparation of surface modified protein nanoparticles by introduction of sulfhydryl groups. *Int J Pharm.*, 211(1–2), pp.67–78.

Wyss-Coray, T. & Mucke, L., 2002. Inflammation in neurodegenerative disease - A double-edged sword. *Neuron*, 35(3), pp.419–32.

Wyss-Coray, T. & Rogers, J., 2012. Inflammation in Alzheimer disease-a brief review of the basic science and clinical literature. *Cold Spring Harb Perspect Med.*, 2(1), p.a006346.

Xing, R. et al., 2013. Hollow iron oxide nanoparticles as multidrug resistant drug delivery and imaging vehicles. *Nano Res.*, 6(1).

Xu, S. et al., 2013. Targeting receptor-mediated endocytotic pathways with nanoparticles: rationale and advances. *Adv Drug Deliv Rev.*, 65(1), pp.121–38.

Xu, W. et al., 2015. Cognitive Reserve and Alzheimer's Disease. *Mol Neurobiol.*, 51(1), pp.187–208.

Xu, Y. et al., 2012. Neurotransmitter receptors and cognitive dysfunction in Alzheimer's disease and Parkinson's disease. *Prog Neurobiol.*, 97(1), pp.1–13.

Yokel, R., Grulke, E. & MacPhail, R., 2013. Metal-based nanoparticle interactions with the nervous system: the challenge of brain entry and the risk of retention in the organism. *Wiley Interdiscip Rev Nanomed Nanobiotechnol.*, 5(4), pp.346–73.

Yu, J. et al., 2012. Hollow manganese phosphate nanoparticles as smart multifunctional probes for cancer cell targeted magnetic resonance imaging and drug delivery. *Nano Res.*, 5(10), pp.679–694.

Yu, S.S. et al., 2012. Size- and charge-dependent non-specific uptake of PEGylated nanoparticles by macrophages. *Int J Nanomedicine*, 7, pp.799–813.

Zensi, A. et al., 2009. Albumin nanoparticles targeted with Apo E enter the CNS by transcytosis and are delivered to neurones. *J Control Release.*, 137(1), pp.78–86.

Zensi, A. et al., 2010. Human serum albumin nanoparticles modified with apolipoprotein A-I cross the blood-brain barrier and enter the rodent brain. *J Drug Target*, 18(10), pp.842–8.

Zhang, L. et al., 2011. T1-weighted ultrashort echo time method for positive contrast imaging of magnetic nanoparticles and cancer cells bound with the targeted nanoparticles. *J Magn Reson Imaging*, 33(1), pp.194–202.

Zhao, Z. et al., 2013. Octapod iron oxide nanoparticles as high-performance T_2 contrast agents for magnetic resonance imaging. *Nat commun.*, 4, p.2266.

Zhou, Z. et al., 2013. Peptide targeted tripod macrocyclic Gd(III) chelates for cancer molecular MRI. *Biomaterials*, 34(31), pp.7683–93.

Zhu, D. et al., 2013. Nanoparticle-based systems for T1-weighted magnetic resonance imaging contrast agents. *Int J Mol Sci.*, 14(5), pp.10591–607.

Zipfel, W.R. et al., 2003. Live tissue intrinsic emission microscopy using multiphoton-excited native fluorescence and second harmonic generation. *Proc Natl Acad Sci U S A*, 100(12), pp.7075–80.

Appendix

Appendix A: Nanoparticle preparation

Prof. Dr. Claus Pietrzik (University Medical Center of the Johannes Gutenberg-University Mainz, Mainz) and Prof. Klaus Langer (Institute of Pharmaceutical Technology and Biopharmaceutics, Münster) were in charge of the preparation of the MLNPs. These methodological descriptions and results were published in an original article (Martinez Vera et al. 2014).

Synthesis of magnetite labeled HSA nanoparticles

Human serum albumin (20 mg) was dissolved in 2 mL purified water and the pH was adjusted to 8.0. The solution was filtered through a 0.22 µm cellulose acetate membrane filter. An aliquot (1 mL) of this solution was mixed with 33.3 µL (1 mg) magnetite dispersion with an average particle size of 8 nm (PlasmaChem, Germany) and 10 µL 1M NaCl solution. The mixture was incubated for 1 h at 20 °C under constant stirring (600 rpm). To initiate nanoparticle formation, 4 mL ethanol were added using a tubing pump. Particles were stabilized by crosslinking using 5.8 µL glutaraldehyde solution (8 %). The crosslinking was performed for at least 12 h under constant stirring at room temperature. A similar procedure was repeated with the different particle sizes of magnetite (diameter of 20 nm and 8 nm) and magnetite loading (47.62 µg/mg MLNP and 90.9 µg/mg MLNP). After preparation the particles were purified by three centrifugation steps (10,000 g, 5 min) and redispersion of the pellets to the original volume in purified water.

Preparation of PEGylated nanoparticles

For PEGylation magnetite labeled HSA nanoparticles were prepared as described above and modified as follows: 1 ml of HSA NP (20 mg/ml) was incubated with 300 µl methoxy PEG succinimidyl active ester (mPEG-SSA, Rapp Polymere, Germany) solution (85 mg/ml in phosphate buffer pH 8.0) for 1 h at 20 °C under constant shaking (600 rpm, Eppendorf thermomixer). The nanoparticles were purified by centrifugation and redispersion as described above.

Nanoparticle characterization

Nanoparticles were analyzed with regard to particle diameter and polydispersity by photon correlation spectroscopy (PCS) using a Malvern Zetasizer Nano ZS (Malvern Instruments Ltd., Malvern, UK). Prior to measurement the samples were diluted with purified water.

The concentration of the purified nanoparticles was determined by microgravimetry. An aliquot (20.0 µl) of the respective nanoparticle sample was put in a micro weighing dish (VWR, Germany). After a drying time of 2 h at 80 °C the dish was weighted with a microbalance (Sartorius, Germany). The content of the nanoparticles was calculated from the difference of the empty and nanoparticle filled dish.

The amount of incorporated magnetite was investigated by total reflection X-ray fluorescence (TXRF) in the Group of Prof. Karst (University of Muenster, Institute of Inorganic and Analytical Chemistry).

Scanning electron microscopy (SEM) images of the magnetite labeled nanoparticles were performed by Elektronen-Optik-Service GmbH, Germany.

Results

In this study we prepared magnetite labeled HSA nanoparticles with a particle diameter between 200 nm and 550 nm. The samples showed monodisperse (PDI < 0.1) or slightly polydisperse (PDI < 0.2) size distribution (Table 7). The amount of incorporated magnetite was calculated by TXRF and indicated almost quantitative magnetite entrapment during the preparation of the nanoparticles (data not shown). SEM images of MLNPs confirmed the results of the PCS and TXRF experiments with regard to particle size and incorporation of magnetite (Figure A-1). Furthermore, in earlier cell culture experiments we could show that nanoparticles based on HSA were non-toxic in concentrations up to 1000 µg/ml (Löw et al. 2011; Storp et al. 2012; Weber, Reiss, et al. 2000).

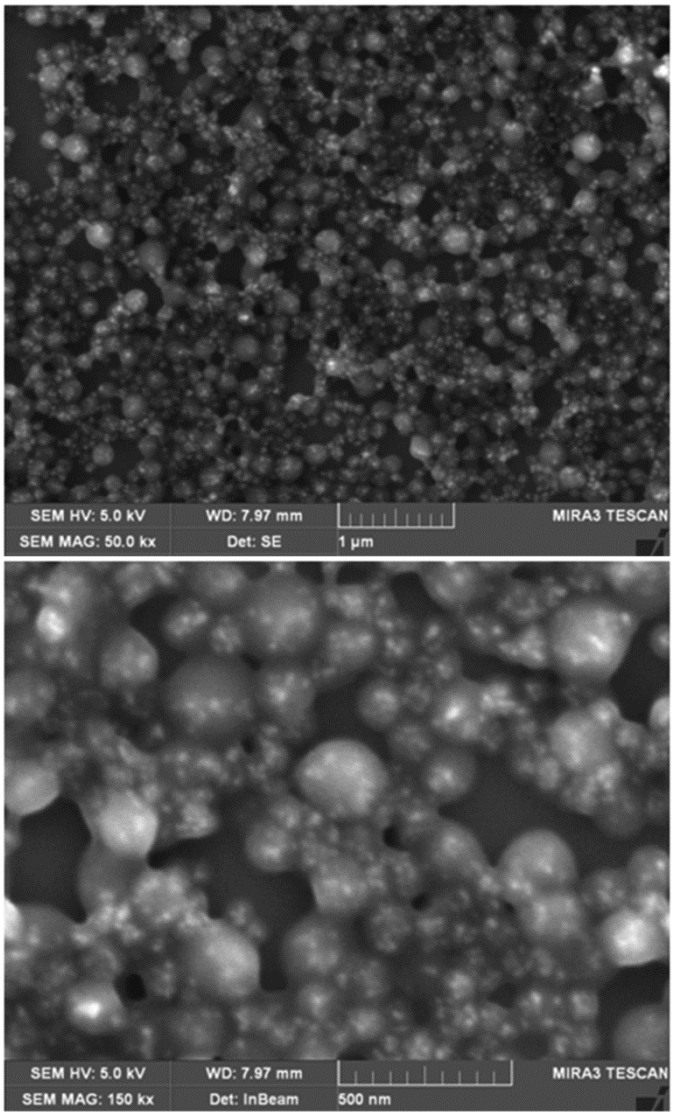

Figure A-1. Magnetite (diameter of 8 nm) from MLNPs is detected (light spots) using scanning electron microscopy (Tescan MIRA XMU with YAG BSE-detector and SE-detector). Upper and lower image: 20,000-fold magnification with 5.78 µm FOV and 60,000-fold magnification with 1.93 µm FOV respectively. Reproduced from (Martinez Vera et al. 2014), copyright (2014) under the terms of the Creative Commons Attribution License (CC BY 4.0), https://creativecommons.org/licenses/by/4.0/.

Appendix B: Fluorescence imaging

Daniel Havas from the JSW Life Sciences GmbH, Austria was in charge of the histological analysis using fluorescence imaging. These methodological descriptions and results were published in an original article (Martinez Vera et al. 2014).

An Axio Imager Z1 microscope (Carl Zeiss AG, Germany) served to image MLNP fluorescence using a 10x Plan Apochromat lens (NA 0.45) and an Axio mRM high sensitive camera with 1x opto-coupler. The camera was set to the linear default in AxioVision (v4.8) software control. The filter sets used were Fs38HE and Fs43 (https://www.micro-shop.zeiss.com/us/us_en/spektral.php).

Histological protocol

Immediately after MRI the rats were sacrificed. Rats were transcardially flushed with 0.9 % saline to remove eventual NPs within vessels together with red blood cells, both of which would bias signal measurements. Rat brains were dissected as follows: heads were cut off and the skins on top of the heads were removed. With an electric cutter, the bone of the skulls were cut and open at several spots to make the next step easier. With small pliers, pieces of the bones were broken away from the skulls so the brains lied open. Then with a spatula, the brains were lifted and connected nerves (e.g. the optic nerve) were cut and the brains were finally removed from the skulls The brains were then fixed in a 4 % neutral buffered paraformaldehyde (PFA) solution for two hours to stabilize proteins and the albumin of the NPs. After cryo-protection in 15 % sucrose until sunk, hemibrains were frozen in dry ice cooled liquid isopentane and systematically cut sagittally at 16 µm thickness on a Leica CM3050 S cryotome. Short PFA exposure guarantees a low green autofluorescent background in the slices but sufficiently fixes the tissue. Air dried and embedded in Mowiol, mosaic images from the CC and the HC were recorded using equal exposure times for each channel and highly constant LED excitation (“Colibri” on a Zeiss Z1 AxioImager with sensitive mRM B&W camera and 10x Plan Apochromate lens). Histogram measurements were performed with ImageProPlus software (v6.2) after manual delineation of the ROI. Histogram measurements of three different medio-sagittal brain levels (approximately 0.2 mm, 1 mm and 2 mm lateral) were averaged per region to one

individual mean per animal. Mean pixel intensities of the CC and HC were assessed for the red and green channel. To evaluate MLNP uptake in the rest of the body, liver and spleen were sampled, cut and investigated for direct MLNP fluorescence of microscopically visible accumulations.

An additional experiment in a single rat was performed to detect and validate the MLNP related fluorescence (Alqudami & Annapoorni 2007; Siwach & Sen 2008) by comparing fluorescence imaging and Prussian blue labeling to Fe^{3+} (Hematognost Fe®, Merck). Dispersed and diffused MLNP are below the microscopic resolution. To achieve a significant accumulation of MLNP deposits and to prove their direct detectability with the used setup, MLNPs were administered into the lateral ventricle and imaged in consecutive sections, one for direct fluorescence, the second stained for Prussian Blue in brightfield.

Results

In the body of the rat, in parallel to MRI, the liver and the spleen presented marked changes in the fluorescence signal (Figure B-1).

The mean fluorescence signal related to MLNPs increased significantly in the investigated rat brain sections of the CC and HC in the green and red channels (Figure 29C). Only very high concentrations of MLNPs can be microscopically seen on fluorescence imaging such as those achieved after intraventricular injection. Figure B-2 shows the accumulations of agglomerated MLNPs following direct intraventricular injection in a single rat close to the intracerebroventricular injection site. The localization in the corresponding Prussian Blue iron stain indicates that the fluorescence of the MLNPs is induced by the magnetite. A direct co-imaging is not possible, since the excitability of the magnetite disappears when the iron is in the Prussian blue complex. In contrast, control rats showed lower fluorescence levels (Figure B-3A) and iron staining of corresponding slices did not reveal any accumulation of iron (Figure B-3B).

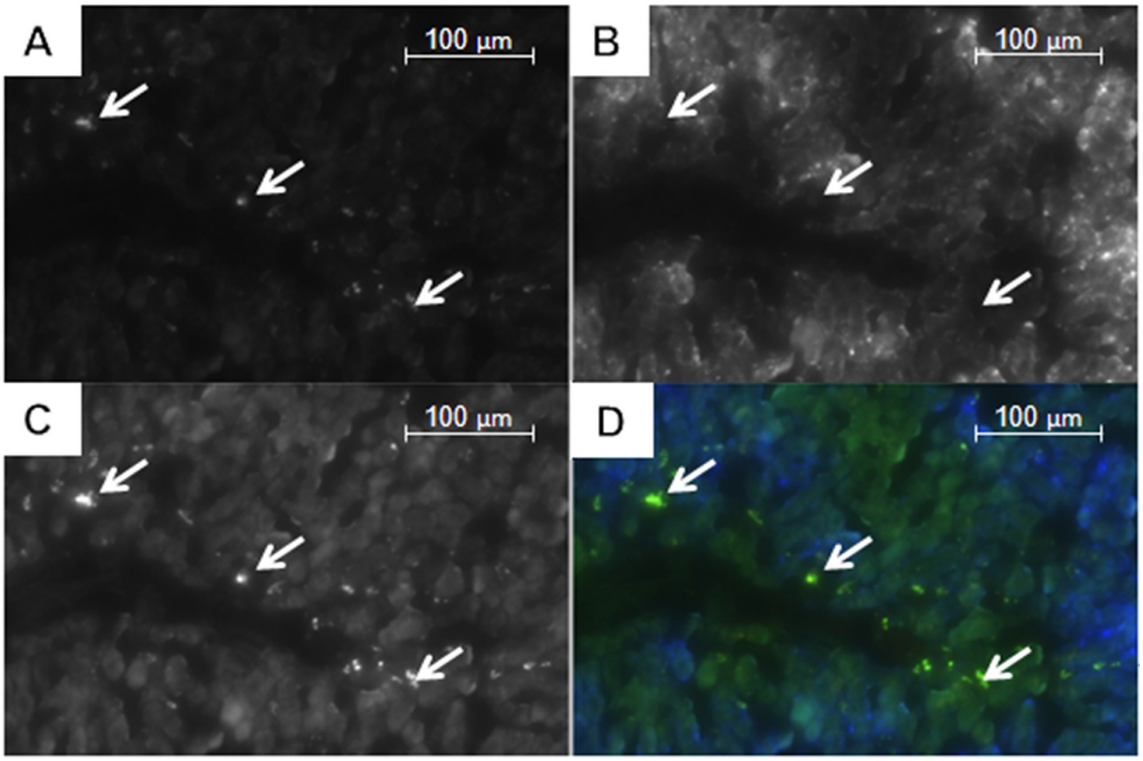

Figure B-1. Red (A) with the lowest background fluorescence, blue (B), green (C), and the sum of these three channels (D) of fluorescence images from a piece of the left liver lobe (bile duct). Agglomerations of magnetite loaded nanoparticles (arrows) are best detected in the green and red channel. Reproduced from (Martinez Vera et al. 2014), copyright (2014) under the terms of the Creative Commons Attribution License (CC BY 4.0), https://creativecommons.org/licenses/by/4.0/.

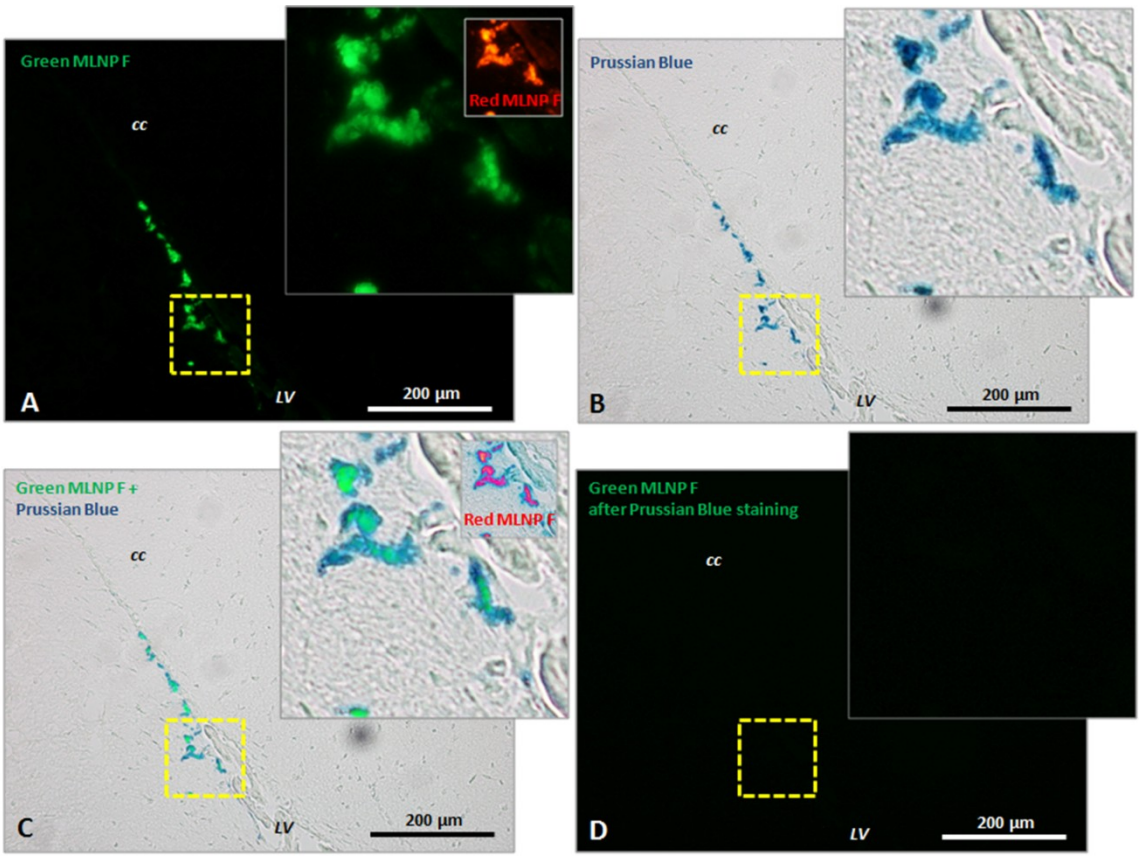

Figure B-2. Prussian Blue staining of fluorescencing (F) magnetite loaded nanoparticles accumulations close to the intracerebroventricular injection site. (A) The magnetite shows emission in the green and red (insert) spectrum with blue and green excitation. It was imaged before doing the Prussian Blue staining from an untreated cryo-slice from PFA fixed brain. (B) shows the Prussian Blue staining, whereas blue color derives from the hexacyanoferrat complex. (C) is a maximum difference projection of (A) and (B), showing the overlap of MLNP fluorescence and Prussian Blue staining. (D) The fluorescence totally vanishes after Prussian Blue staining, indicating that binding the iron in the complex alters the excitability of the magnetite molecules. LV = lateral ventricle; CC = corpus callosum; 20-fold magnification. Reproduced from (Martinez Vera et al. 2014), copyright (2014) under the terms of the Creative Commons Attribution License (CC BY 4.0), https://creativecommons.org/licenses/by/4.0/

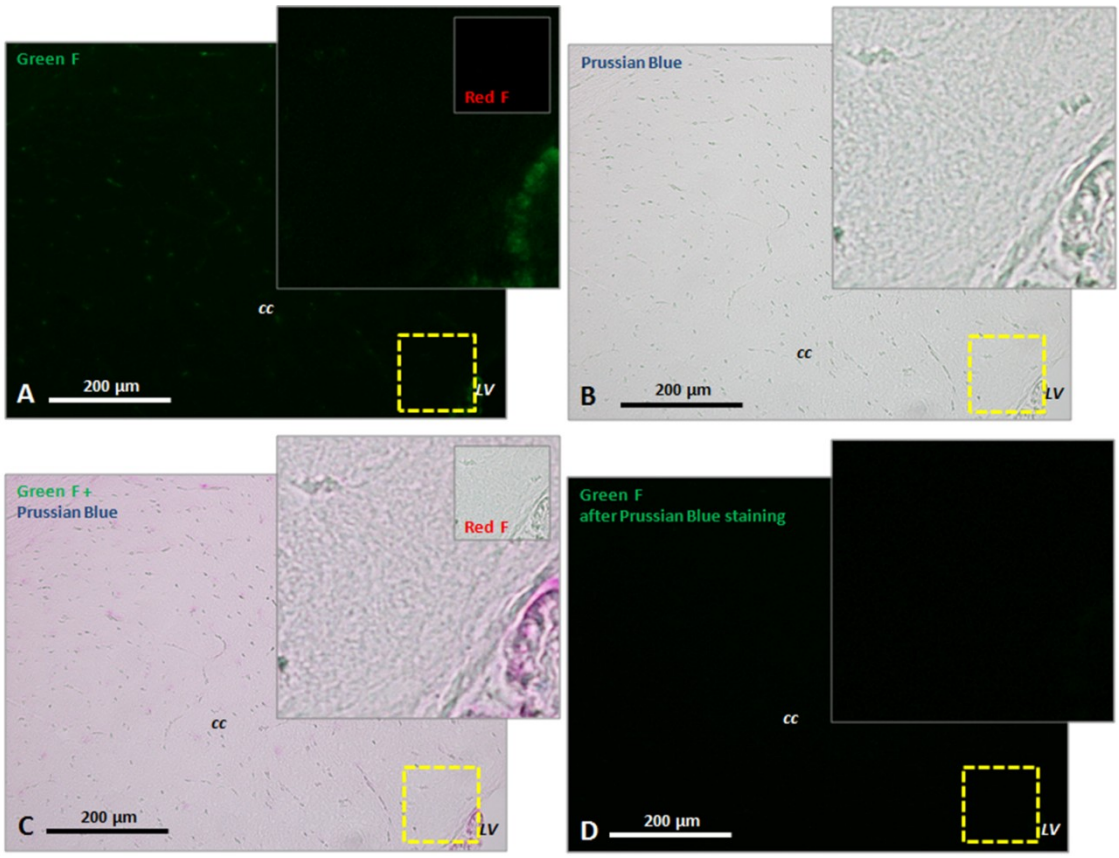

Figure B-3. Prussian Blue staining close to the injection site of the rat shown in Figure B-2 in a vehicle control rat. (A) Slice fluorescence levels are generally low in the cryo slices and in most cases restricted to vasculature as shown here for some ependymal cells of the chorioid plexus. (B) shows the Prussian Blue staining, whereas in healthy rats iron accumulations (from micro bleedings) in the brain are typically absent (C) is a maximum difference projection of (A) and (B). (D) The slice fluorescence vanishes during Prussian Blue staining and brightfield imaging. Abbreviations: F = fluorescence; LV = lateral ventricle; CC = corpus callosum. Magnification = 20x. Reproduced from (Martinez Vera et al. 2014), copyright (2014) under the terms of the Creative Commons Attribution License (CC BY 4.0), https://creativecommons.org /licenses/by/4.0/.